Impact of friction stir processing on mechanical, microstructural, tribological and electrochemical properties of aluminum alloys

BY

Ibrahim Hassan ZainElabdeen

A Thesis Presented to the

DEANSHIP OF GRADUATE STUDIES

KING FAHD UNIVERSITY OF PETROLEUM & MINERALS

DHAHRAN, SAUDI ARABIA

In Partial Fulfillment of the
Requirements for the Degree of

MASTER OF SCIENCE

In

MECHANICAL ENGINEERING

APRIL-2020

KING FAHD UNIVERSITY OF PETROLEUM & MINERALS

DHAHRAN- 31261, SAUDI ARABIA

DEANSHIP OF GRADUATE STUDIES

This thesis, written by **Ibrahim Hassan ZainElabdeen** under the direction of his thesis advisor and approved by his thesis committee, has been presented and accepted by the Dean of Graduate Studies, in partial fulfillment of the requirements for the degree of **MASTER OF SCIENCE IN MECHANICAL ENGINEERING**.

Zuhair Gasem

Dr. Zuhair Gasem
Department Chairman

Dr. Fadi Al-Badour
(Advisor)

Dr. Suliman Al-Homidan
Dean of Graduate Studies

Dr. Neçar Merah
(Member)

Date

Dr. Rami Sulieman
(Member)

This work is dedicated to my family

ACKNOWLEDGMENTS

All praise and thanks are to Allah, to him alone for giving me the power, patience, peace of mind, good health and strength to successfully complete this work. I am highly indebted to King Fahd University of Petroleum and Minerals (KFUPM) for giving me this opportunity to pursue my graduate studies in mechanical engineering.

I would like to express my gratefulness to my family for their continuous unconditional support, encouragement and prayers.

My sincere gratitude goes to my thesis advisor Dr. Fadi Al-Badour for his guidance, precious advices, enthusiasm, encouragement and the imparting of his knowledge and expertise.

I would like to express my appreciation to my committee members Prof. Neçar Merah and Dr. Rami Suleiman for their valuable assistance, guidance and constructive advice which really help me to successfully complete my thesis.

I am very grateful for Dr. Akeem Adesina for his efforts and support provided toward the success of this work. Besides him, I would like to thank Mr. Ahmed Al-Ghanim and Mr. Abdullah Al-Mohammedali for their unmatched support.

I would like to extend my appreciation to the department's chairman Dr. Zuhair Gasem and all faculty members in the Mechanical Engineering Department for their help and support during my master study.

This acknowledgment will not be complete without appreciating the financial Support provided by the Deanship of Scientific Research at KFUPM under the grant IN161049.

TABLE OF CONTENTS

LIST OF TABLES

LIST OF FIGURES

ABSTRACT

Full Name : Ibrahim Hassan ZainElabdeen

Thesis Title : [Impact of friction stir processing on mechanical, microstructural, tribological and electrochemical properties of aluminum alloys]

Major Field : Mechanical Engineering

Date of Degree : April-2020

Friction stir processing (FSP) is a solid-state technique developed on the same principle of friction stir welding (FSW). However, rather than joining sheets or plates, FSP is employed to modify the surface/bulk microstructure and/or development of surface metal composite.

Herein, FSP was carried out on Al-Mg-Si and Al-Cu-Li Alloys to improve the surface microstructure without adding reinforcement particles. The impact of various process conditions; i.e. traveling speed (ranging from 50 mm/min to 250 mm/min) and rotational speed (ranging from 400 rpm to 1200 rpm), on the microstructure, mechanical properties, wear characteristics, and corrosion behavior were studied in detail.

Several characterization techniques such as scanning electron microscope (SEM), advanced optical microscope (OM) and X-Ray diffraction (XRD) were employed in the present study. Microstructural observation revealed a remarkable diminishing in grain size after employing FSP for both alloys. Moreover, higher tool traveling speed resulted in an

appreciable reduction in the grain size and that was ascribed to the reduction in heat input, while increasing the tool rotational speed caused noticeable grain coarsening for the same mentioned reason. Superior microhardness was obtained for all Al-Mg-Si alloys processed samples under different process conditions where the sample processed at the lowest traveling speed showed an improved microhardness by approximately 100%. Wear resistance was found to be reduced marginally for the most of processed samples with no remarkable change in wear mechanism despite the marked enhancement in microhardness.

Several electrochemical tests were carried out to evaluate the influence of surface processing on the corrosion behavior such as electrochemical impedance spectroscopy (EIS), linear polarization resistance (LPR) and potentioynamic polarization (PDP). In case of Al-Mg-Si alloy (6061 AA), all results obtained from various electrochemical techniques were found to be in a good agreement, where the base sample demonstrated the poorest corrosion resistance. Besides, increasing the tool traveling speeds resulted in a remarkable improvement in corrosion resistance where the sample processed at the highest traveling speed showed a reduction in the corrosion current density (I_{corr}) by approximately 600 times when compared with the base sample. On the other hand, increasing the tool rotational speed has improved the corrosion resistance markedly where the sample processed at the highest rotational speed revealed a decline in the corrosion current density by about 55 times. For Al-Cu-Li alloy (2099 T-83), the non-destructive electrochemical examinations i.e. EIS and LPR were not in full agreement with PDP results. Both EIS and LPR results revealed appreciable enhancement in corrosion resistance where all processed

samples showed a significant improvement in corrosion resistance by either increasing the tool traveling speed or the tool rotation speed.

ملخص الرسالة

الاسم الكامل:ابراهيم حسن زين العابدين محمد

عنوان الرسالة: تأثير عملية التحريك الاحتكاكي على خصائص التآكل والصدأ والتراكيب البنائية متناهية الصغر والخصائص الميكانيكية والكهروكيميائية لسبائك الالمونيوم

التخصص:الهندسة الميكانيكية

تاريخ الدرجة العلمية:أبريل 2020

تم في هذا البحث استخدام تقنية التحريك الاحتكاكي وهي عملية معالجة للأسطح تتم عند درجة حرارة أقل من حرارة الذوبان. هذه العملية مستنبطة من عملية اللحام التحريكي الاحتكاكي لكن عوضا عن لحام معدنين، فإن هذه العملية تحسن خواص الاسطح عن طريق اضافة مواد أكثر قوة أو تحسين المواد عن طريق تغيير البنية المجهرية.

تم إجراء هذه العملية على نوعين مختلفين من سبائك الالمونيوم، حيث كان النوع الاول هو سبيكة الالمونيوم غير المعالج حرارياً والناتج من اضافة عنصري المغنيزيوم والسيليكون كعناصر أساسية إلى الألمونيوم، اما السبيكة الثانية فهي سبيكة الألمونيوم المعالج حرارياً والناتج من اضافة عنصري النحاس والليثيوم كعناصر أساسية إلى الألمونيوم.
إن الهدف الرئيسي من هذه الدراسة هو تقييم تأثير العوامل المتغيرة أثناء عملية التحريك الاحتكاكية على البنية المجهرية لكلا السبيكتين والخصائص الإلكترو كيميائية. تمت أيضا دراسة أثر العوامل المتغيرة على الخواص الميكانيكية والتآكل لسبيكة الالمونيوم غير المعالجة حرارياً. تم استخدام عدد من التقنيات المتقدمة لتقييم أثر عملية التحريك الاحتكاكي على سبائك الالمونيوم مثل المجهر الضوئي المتقدم والماسح الالكتروني فائق الدقة والاشعة السينية.

أظهرت النتائج أن العوامل المتغيرة (السرعة الخطية والسرعة الدورانية) لها أثر إيجابي ضخم على كل الخصائص الميكانيكية والإلكترو كيميائية للمواد التي تمت دراستها. على سبيل المثال وبالنسبة لسبيكة الالمونيوم غير المعالجة حرارياً، اثبتت الدراسة أن الخصائص الميكانيكية بلغت أوجها عند أدني سرعة دورانية وعند تثبيت السرعة الخطية. أما عند تثبيت الدورانية الخطية، فإن أفضل خصائص ميكانيكية تم التوصل إليها كانت عند أدنى سرعة خطية. بالنسبة للخصائص الإلكترو كيميائية فقد كانت

على العكس تماماً مقارنة بالخواص الميكانيكية أي أن أفضل خواص مقاومة للصدأ كانت عند اقصى سرعتين دورانية وخطيه عند تثبيت السرعتين الخطية والدورانية. أظهرت النتائج عدم جدوى التقنية الاحتكاكية لتحسين خواص التآكل.

أما بالنسبة لسبيكة الالمونيوم المعالجة حراريا، أظهرت النتائج أن التحسن في الخصائص الإلكترو كيميائية كان على نفس نهج السبيكة غير المعالجة حرارياً.

CHAPTER 1

INTRODUCTION

1.1 Motivation

As a result of their outstanding characteristics, including high ductility, good corrosion resistance, and high strength to weight ratio, aluminum alloys attracted more attention to be employed in several industries, such as automotive, defense and aerospace [1]. Nevertheless, despite unique properties that were mentioned earlier, aluminum alloys demonstrate poor surface characteristics such as wear-resistance and microhardness which was considered the major problem that restricted their applications [2][3]. It should be pointed out that the life of many engineering applications primarily relies on surface characteristics such as wear, corrosion and erosion resistance [4]. Thus, to overcome either poor surface or bulk properties, various conventional techniques were employed to add some fillers; forming a composite surface to enhance its mechanical properties. These techniques include, but are not limited to: diffusion bonding, casting, electron beam techniques, powder metallurgy, and spray depositions methods [5][6][7] Although metal matrix composites characteristics are governed through fractions and size of reinforcement particles and interfaces between incorporated particles and matrix, embedded ceramic particles sacrifice both materials ductility and toughness owing to the non-conformable nature of ceramic which may restrict their applications [3][8]. Moreover, fabrication with these techniques is carried out at an elevated temperature; in the liquid phase, which may lead to intermetallic reactions as well as adverse phases between reinforcements and substrate [7]. Furthermore, some of these methods are associated with particle clustering and porosity which reduces tensile properties considerably as reported by Gangil et. al [9].

Thus, the fabrication of surface composite beneath the melting temperature of the base material would result in solving most of the problems mentioned above [4]. Recently, the voluminous body of research has been conducted in developing surface metal matrix using friction stir processing. Friction stir processing (FSP) was developed on the same basis of friction stir welding (FSW) which was invented by The Welding Institute (TWI) in 1991 [10]. Friction stir processing (FSP) resulted in a dramatic change in mechanical properties, wear behavior and corrosion resistance through a severe plastic deformation accompanied by heat generated during stirring action [11]. Thus, FSP affects the surface microstructure considerably and can result in ultra-fine equiaxed grains. Moreover, uniform dispersion of incorporated material as well as precipitates can also be obtained [11]. Several advantages were made FSP more favorable as compared to other conventional methods as it is considered a short rout technique to microstructure refinement. In addition, corrosion behavior, mechanical properties, microstructure and wear resistance can be controlled through changing process parameters of machine or tool design. Moreover, by changing the plunging depth, the depth of the processed zone can be controlled. Furthermore, FSP could be considered as a green technique wherein friction between tool and workpiece is main source of the heat input and no deleterious gas is used [12]. A huge volume of research was conducted to examine the change in microstructure, wear resistance, mechanical properties, corrosion behavior, particles dispersion during the fabrication of surface metal matrix using FSP. However, it is strongly believed that the enhancement in various

properties obtained through embedded hard phases can be gained with just varying process conditions.

1.2 Objectives

The main objectives of this research are:

- To modify 6061 and 2099 Aluminum alloys surfaces using friction stir processing.
- To explore the impact of varying process parameters i.e. rotation and traverse speeds on the microstructure and the corrosion behavior for both alloys.
- To study the tribological characteristics and mechanical properties of 6061 AA friction stir processed surfaces as compared to the base metal.

1.3 Research Methodology

In the present work, surfaces of 6061 and 2099 AA were modified using friction stir processing under different process parameters. A pin tool was utilized for 2099 AA, whereas a pinless tool was used for 6061 AA. Friction stir welder machine was operated under position control where welding speed was varied while rotational speed was kept constant and vice versa. As depicted in Figure 1-1, processing of samples was followed by sample preparation step where all samples were cut to suitable sample dimensions for microstructural evaluation, mechanical, tribological and corrosion testing. To investigate the change in microstructure, all samples were ground, polished and subsequently etched. However, to evaluate the microhardness and elastic modulus, diffident samples were

ground and polished before the test. For wear and corrosion tests, all samples were only ground to remove all FSP shoulder marks. After corrosion and wear tests, SEM technique was utilized to analyze the mechanisms associated with worn and corroded surfaces. The schematic diagram of Figure 1-1 describes the methodology followed during this work.

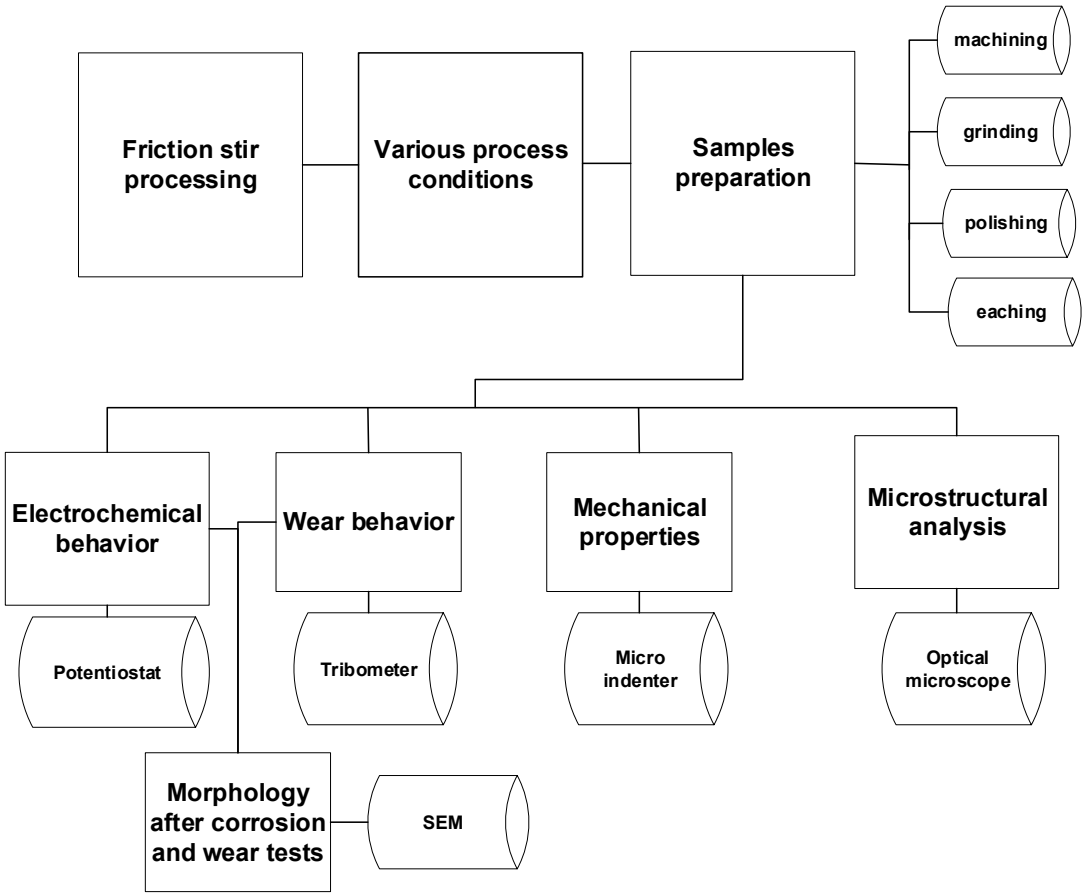

Figure 1- 1 Schematic diagram of research methodology

1.4 Organization

This thesis consists of five chapters organized as follows: chapter one is the introduction and contains the motivation and research objectives. The literature review is covered in the second chapter which includes the state-of-art research in the field of FSP and research gap. After that, detailed information about the experimental procedure is covered in the third chapter. The results and discussion of the 6061 AA is presented in chapter four, whereas the discussion of the obtained results of 2099 AA is presented in the fifth chapter. Finally, the conclusions and recommendations of this study is presented in the last chapter.

CHAPTER 2

LITERATURE REVIEW

2.1 Friction stir welding:

Friction stir welding (FSW) is a solid-state welding process invented by The Welding Institute (TWI) at the beginning of the last decade from the previous century. Although, FSW process was designed to weld metals that cannot be welded easily by conventional methods such as Aluminum and magnesium; however, the usage of friction stir welding process has been extended these days from polymers to steel. Huge investments had been directed in the development of this process by research institutes, universities, and different companies. During 16 years of progress, the welding institute gave around 200 licenses to use the process, close to 2000 patent application related to this process have been filled [13]. The basic principle of this process is simple. A rotating tool consists of two parts, shoulder with a larger diameter and pin with smaller one, are pressed against abutting or lapping edges of sheets or plates that need to be welded and move along the line of joint as depicted in Figure 2- 1[4][12][14].

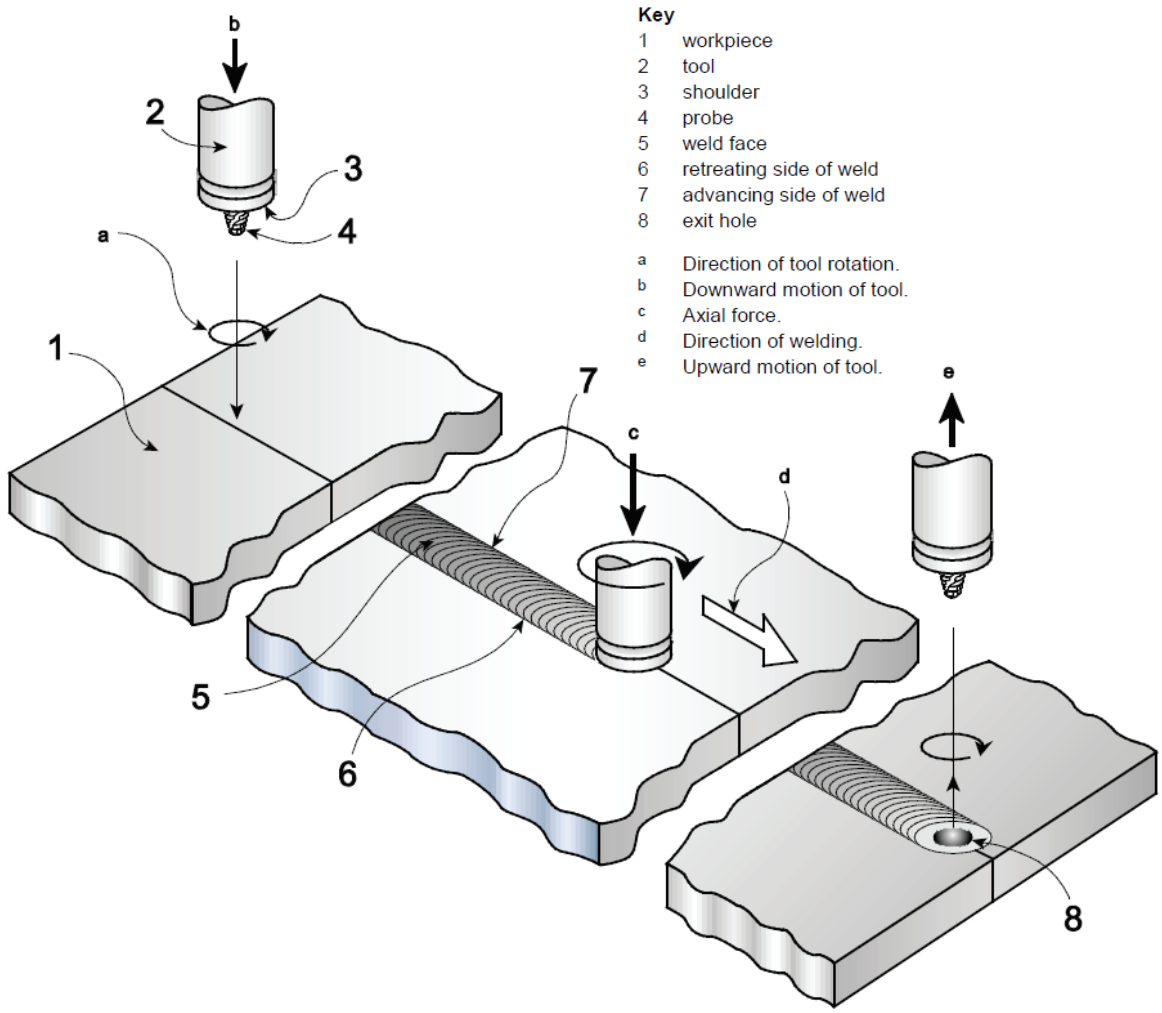

Figure 2- 1 basic configuration of FSW (Butt Joint) [15]

The retreating side is commonly known for the side of the weld where the rotating tool moves contrary to traveling direction. On the other hand, as presented in Figure 2- 1 on the advancing side of the weld both the direction of tool rotation and tool traveling are the same.

2.2 Friction stir processing:

It is one derivative of friction stir welding which is used widely for either surface modification for grain refinement or development of surface composites. FSP was developed by Mishra et al. in 2003 to fabricate al-SiC metal matrix composite [16].

Figure 2- 2 depicts a schematic representation of friction stir processing, where a rotating tool is pressed against the surface of bulk material and therefore provides the adequate heat to soften the area around the tool through the action of stirring. Obviously, FSP implicates a sever plastic deformation for the material around the tool at a temperature far low than the melting temperature. Thus, both elevated temperature and mechanical stirring result in a grain refinement and homogenization.

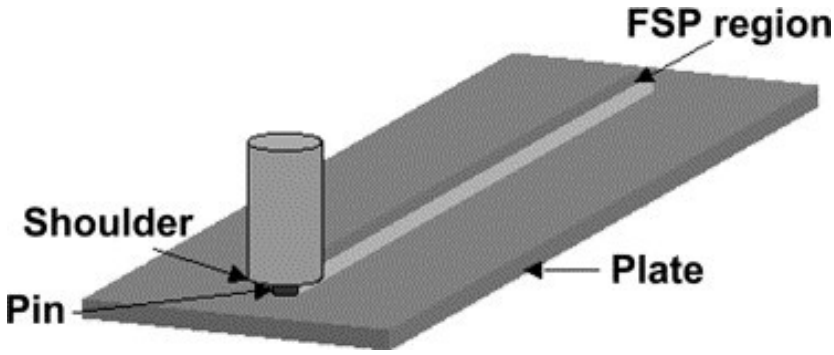

Figure 2- 2 Schematic of friction stir processing [16]

2.2.1 Friction stir processing as a surface modification approach:

Alidokh et al. [17] successfully modified A365 surface by using FSP. Rather than adding powder, they studied the effect of changing rotating speed on mechanical properties, microstructure, and wear resistance of modified surfaces. Their results showed that a higher

rotating speed caused a considerable modification in Si morphology as well as grain size. Furthermore, enhancement in hardness was also noticed which was the core reason for the improvement in wear resistance. Zahmatkesh et. [18] evaluated wear behavior, microstructure, and microhardness of friction stir processed Al2024. Fine equiaxed grains were detected at the nugget zone of the processed sample which contributed to hardness improvement. In addition, the friction coefficient of the processed sample was lower than that of the base metal which was attributed to a significant reduction in plastic deformation between contacted surfaces. Therefore, both lower friction coefficient and higher hardness were the main reasons for wear resistance improvement.

2.2.2 Friction stir processing to synthesize surface composite

Different mechanical characteristics, wear behavior, microstructural aspects and corrosion resistance were investigated whereby using single reinforce particles and dual reinforce particles.

A surface metal composite of Al5083-B_4C was fabricated using FSP by Yuvaraj et al. [19]. They addressed the influence of reinforcement size as well as the number of tool-passes on wear-resistance, microstructure, and mechanical properties of newly developed surfaces. Their findings demonstrated that the increment in the number of passes resulted in uniform dispersion of powder and thus a higher hardness. In addition, particles with smaller size had a great contribution in producing ultra-fine grains. Therefore, a higher number of passes with BC_4 nanoparticles was optimum parameter because it gave the highest wear resistance, hardness, and tensile strength.

Sivanesh el al. [20] have successfully synthesized AA6082-$CaCO_3$ using FSP and have inspected the influence of added particles on wear resistance, microstructure, and hardness. The results demonstrated that a slight enhancement in hardness for the sample processed without powder; however, the fabricated surface composite exhibited outstanding wear resistance which was owed to the initiation of a solid lubricant film and thereby reducing metal to metal contact.

Thangarasu et al. [21] have synthesized 6082-TiC surface composite at various volume fractions of reinforcement using friction stir processing and have evaluated mechanical properties, microstructure and wear behavior. The finding revealed that all mechanical properties as well as wear resistance were the best at the highest volume fraction of reinforced particles of 24 %.

Kumar et al. [22] have successfully embedded tungsten particles in the Al5083 matrix using friction stir processing and compared the fabricated metal composite surface with friction stir processed surface without powder and the base metal. The results indicated a homogenous distribution of reinforcement particles in the aluminum matrix. Moreover, the fabricated composite exhibited a considerable enhancement in hardness which led to improve the wear resistance of a composite surface.

Kurt et al. [23] have incorporated SiC particles to A1050 using friction stir processing and have compared the influence of rotation speed and traveling speed on mechanical properties and microstructure of friction stir processed samples as well as friction stir

processed samples with added ceramic phase. The results indicated a remarkable enhancement in hardness with traveling speed rises for samples processed without powder, whereas, with adding powder increasing traveling speed resulted in hardness deterioration. On the other hand, rising rotation speed for samples processed without powder resulted in hardness reduction, while, changing the rotational speed for composite samples exhibited a marginal impact on hardness. Additionally, better reinforcement dispersion was observed at a higher rotation speed.

Recently, Manochehrian et al. [24] have addressed the outcome of three different volume fractions of Ti_3AlC_2 added to A356 using FSP on microstructure, mechanical characteristics and wear resistance. The results have indicated homogenous dispersion of fine Si in the matrix and decrease in porosity was also obtained which was attributed to refinement in grains. In addition, the composite sample with a higher reinforcement content exhibited the best mechanical properties meanwhile, the minimum friction coefficient was also observed at this higher volume fraction which had a great contribution to the reduction of mass loss.

Bourkhani et al. [25] have fabricated AA1050-Al_2O_3 composite using FSP and studied mechanical properties, microstructural changes and tribological behavior at different samples depth and tool passes. The finding demonstrated nonuniform particle distribution and heterogeneous grain structure after one pass; however, after the second pass, uniform particle distribution and grain structure were clearly observed. In addition, by changing

sample depth, a slight change in mechanical properties was detected; nevertheless, the wear resistance illustrated a significant improvement at higher sample depth.

Rana et al. [26] have synthesized AA7075-B_4C composite using FSP and have made a comparative study to investigate the influence of powder size and changing the direction between the passes on reinforcement dispersion, microstructure and wear behavior. The finding indicated a uniform dispersion of powder for samples processed by changing the direction after each pass. In addition, a sample with finer powder particles exhibited both the highest microhardness and lowest mass loss.

S.A. Alidokh et al. [27] have fabricated A356- SiC-MoS2 hybrid metal matrix using friction stir processing and have compared the microstructure, wear resistance and mechanical properties of as-cast A356 with unitary A365-SiC and binary A365-SiC-MoS2 composites. They demonstrated a significant change in the microstructure of composites. The main features of microstructural modification were breakage of Si circular particles and aluminum dendrites, which result in a uniform distribution of both ceramic and solid lubricant particles in the metal matrix. Moreover, the ceramic particles and MoS2 resulted in a considerable enrichment in both wear resistance and hardness.

Yuvaraj et al. [28] have fabricated the Al5083-TiC-B_4C surface matrix using friction stir processing and have assessed the impact of mono composite and hybrid composite on mechanical properties and wear resistance. A uniform dispersion of incorporated ceramic particles in the aluminum matrix was achieved for various composites. The results

demonstrated that both the highest hardness and tensile strength were observed for Al5083-B_4C composite; nevertheless, the least ductility was observed for this mono composite. Moreover, Al5083-TiC-B_4C binary composite exhibited the maximum resistance to wear among all sample and that was attributed to the lubrication effect of TiC and higher load-bearing capacity of B_4C.

Eskandari et.al [29] have utilized FSP to produce AA 8026-TiB_2-Al_2O_3 composite. They have investigated the impact of the changing number of passes, powder size, traveling speed, rotational speed on wear resistance, microstructure, and mechanical properties. The results have revealed that the higher rotation speed, lower traveling speed or higher number of passes resulted in a uniform distribution of reinforced particles in the matrix. Additionally, a vital role of particle size was also detected. Moreover, an enhancement in hardness on the fabricated composite at a higher rotation speed, lower traveling speed and higher number of passes and thereby improving wear resistance.

Palanivel et.al [30] have synthesized AA6082-TiB_2-BN surface composite via FSP and have addressed the influence of using unitary and binary reinforced particles on microstructure and wear resistance. The results showed a uniform distribution of added particles in the matrix without any segregation. Also, binary composite exhibited a slight enhancement in wear resistance as compared to two other mono composites. However, a considerable enhancement in wear resistance was detected as compared to the unreinforced sample.

Amra et.al [31] have studied the microstructural and tribological aspects of AA5083 reinforced with SiC and CeO_2 using friction stir processing. Their finding concluded that unitary AA5083-SiC showed the highest hardness. However, hybrid AA5083-CeO_2-SiC exhibited the outstanding wear resistance and that was ascribed to lubricated layer made by CeO_2. Likewise, a comparative study by Soleymani el al. [32] aimed to investigate the impact of adding mono composite of SiC or hybrid composite of SiC- MoS_2 added to Al5083 using FSP. The results indicated the highest hardness of SiC mono composite; nevertheless, hybrid composite exhibited superior wear resistance which was attributed to the lubricant film made by MoS_2. Similarly, A413-SiC- MoS_2 hybrid composite surface was fabricated using FSP by Janbozorgi et al. [33]. They indicated that as compared to A413-SiC mono composite, A413-SiC- MoS_2 binary composite exhibited a better wear resistance which was ascribed to the lubricant film that led to diminishing friction coefficient and thereby enhancing wear resistance. The impact of relative ratios of graphite and alumina added to Al5083 using FSP on wear and mechanical properties was investigated by Mostafapour et.al [34]. They illustrated that the highest wear resistance was observed for the composite with a higher graphite content which was owed to the lubrication properties of graphite. Additionally, the better mechanical performance was detected for the composite with a higher alumina content which was ascribed to the decrease of alumina mean interparticle spacing.

Srinivasu et al. [35] have fabricated A356-B_4C-MoS_2 composite using friction stir processing and have investigated the effects of adding micro size solid lubricant MoS_2 to

different sizes of boron carbide on microstructure and wear behavior. The finding showed a significant refinement in the microstructure. Moreover, a binary composite of MoS_2 and nano-sized B_4C exhibited the lowest coefficient of friction and thus the least mass loss.

Sudhakar et al. [36] have added B_4C-MoS_2 to AA7075- using FSP and have studied the influence of boron carbide particle size namely 160, 60, and 30 µm on wear resistance, mechanical properties and microstructure and thereafter have investigated the same properties when MoS_2 solid lubricant was added. The finding showed microstructural refinement and a homogenous distribution of carbides particles. In addition, 30 µm B_4C have shown the greatest hardness and wear resistance among all mono composites; nevertheless, after adding MoS_2 further improvement was obtained in both hardness and wear resistance which was ascribed to the formation of tribo-film.

Mahmoud et al. [37] have fabricated A 1050-SiC- Al_2O_3 hybrid composite surface using FSP and have studied the impact of relative fractions of reinforced particles on a hybrid composite surface wear resistance and hardness. The results demonstrated that wear rate showed a great dependency on the applied force and relative fractions of added particles. Further, at a normal force of 5 N, the binary composite with a ratio of 4:1 (SiC to Al_2O_3) illustrated an outstanding wear performance, whereas, at 10 N normal load, the mass loss for all processed samples under different ceramic ratios was almost equal to that of the unreinforced specimen.

Recently, Deore et al. [38] have incorporated three different kinds of fillers namely MWCNTs, SiC and Cu in AA7075 using friction stir processing and have investigated the effect of these fillers and age hardening on microstructure, mechanical properties and wear behavior. They revealed a significant grain refinement in all processed samples with or without additives; nevertheless, adding filler resulted in further refinement as a result of the pinning action of additives. In addition, age hardening that followed FSP has resulted in the existence of $MgZn_2$ for all mono composite samples. Although all friction stir pressed samples demonstrated an improvement in mechanical properties and wear behavior, post heat treatment has resulted in further enhancement in these properties for all samples.

2.2.3 Effect of varying number of passes and changing the direction during FSP

Hashemi et al. [39] have investigated impact of varying the number of passes and tool geometry during fabricating of Al7075-TiN composite using FSP on microstructure, hardness and wear behavior. Three kinds of pin geometries were utilized including, threaded, triangular and square pins. The results indicated the threaded pin with four passed exhibited the lowest friction coefficient, the highest microhardness and the least mass loss which was ascribed to the formation of Al_2O_3 film that reduced metal to metal contact and thereby enhancing wear resistance.

Huang et al. [40] synthesized Al1060-W surface composite using FSP and studied the effect of the number of passes on microstructure, particle distribution, electrical conductivity, and mechanical properties. The finding revealed a uniform distribution and

more grain refinement were gained with an increase in the number of passes. In addition, tensile strength and microhardness of composites surface were exhibited the best performance at the highest number of passes; however, the least influence of process was found on electrical conductivity.

Ahmadifard et al. [41] have produced Al7075-Ti_3AlC_2 composite using FSP and have studied the influence of the number of passes on reinforcement dispersion, mechanical properties, microstructure and wear behavior. The results showed a uniform distribution in strengthening particles after four passes rather than one pass. In addition, both microhardness and strength have shown superior properties after four passes; nevertheless, this ceramic phase has resulted in a considerable reduction in the ductility. Furthermore, four passes have resulted in a coefficient of friction decrement and thus wear resistance improvement.

Gao et al. [42] compared Al7075 base metal with friction stir processed Al7075 and Al7075-Pl composites produced using FSP at different number of passes. They have investigated the effect of increment in the number of passes on the dispersion of the particles, mechanical properties and wear behavior. The finding showed a uniform dispersion of particles with a higher number of passes. In addition, the effect of Pl soft particles was reflected on microhardness which illustrated a slight reduction as compared to the process sample without powder. Moreover, the wear resistance was the highest for the sample that process with highest number of passes.

In situ composite of Al050-Fe_3O_4 was synthesized using multi pass FSP by Eftekhari et al. [43]. They have changed the direction after each pass to obtain a uniform microstructure and have investigated the contribution of passes number on strengthening, particulate distribution, grain size, wear behavior, tensile strength and corrosion susceptibility. They demonstrated that the higher number of passes led to gain refinement and better particles distribution and therefore, improvement in strength and hardness. In addition, the fractured surface after one pass illustrated a brittle fracture compared to a mixture of ductile and brittle fractures that was obtained at higher number of passes. Moreover, the sample processed with the highest number of passes displayed the least amount of material loss during sliding which was attributed to the lower friction coefficient. Furthermore, processed samples showed more noble potential than that of base metal and pitting resistance also improved; however, the corrosion rate for the processed samples increased as compared to as received specimen.

Shafiei et al. [44] have successfully fabricated Al6082-Al_2O_3 composite via FSP and have investigated the influence of varying number of passes on the grain size, reinforcement size and dispersion, microhardness and wear resistance. They indicated that a rise in the number of passes resulted in more grain refinement, reduction in the clustering of particles. In addition, the microhardness of the composite sample processed at a higher number of passes showed a considerable improvement which was interpreted by grain size refinement and better reinforcement particle distribution. Moreover, this improvement in microhardness led to outstanding wear performance of the composite.

Patel et al. [45] have utilized FSP in the synthetization of A4047-$ZrSiO_4$ unitary composite and have assessed the impact of an increase in the number of passes on microstructure, mechanical properties and wear resistance. They demonstrated more uniform distribution of added particles with increasing in process passes. In addition, uniform dispersion of particles has reflected in wear resistance as well as mechanical properties enhancement.

The effects of a varying number of tool pass during fabrication of AA5053-ZrO_2 nanocomposite using FSP on microstructure, mechanical properties and wear behavior were studied by Mirjavadi et al. [46]. The finding demonstrated an obvious refinement in grain structure and further improvement in particle distribution with an increasing number of passes. In addition, at higher passes number, the composite exhibited superior mechanical properties. Moreover, the least mass loss was observed for the sample fabricated with the highest number of passes which was interpreted by hardness enhancement and load-bearing capacity of zirconia.

2.2.4 Impact of tool design during FSP

Chen et al. [47] have conducted an experiment aimed to study the effect of pin eccentricity during friction stir processing of Al5052 on mechanical properties and microstructure. They used three different tools including a concentric tool, 0.4 mm and 0.8 mm eccentric tools. The results showed enlargement in the onion ring area after using eccentric pins as compared to a concentric pin. In addition, an optimized eccentric pin can result in improvement in mechanical properties; nevertheless, over-eccentric pin produces much

than desired heat which leads to grain coarsening and therefore mechanical properties declines.

Hussain et al. [48] have studied the effect of tool pin shape during fabrication of Al7075-TiN composite using multi-pass FSP on mechanical properties, microstructure and wear behavior. Different tool geometries were used including, threaded, square and triangular. It was observed that the tool geometry has a great impact on strengthening particulates distribution and therefore composite surface properties. Additionally, the highest tensile strength was captured for the square tool compared to the least mass loss which was observed for the threaded tool; however, all process samples demonstrated a poor ductility as compared to the base metal and this is attributed to a hard phase of embedded ceramic.

2.2.5 Influence of varying speed during FSP

Recently, Zhang et al. [49] utilized FSP to synthesize Al1060 -CNTs nanocomposite, wherein the tool rotation speed was varied from 600 to 950 rpm while traverse speed was increased from 15 to 90 mm/min. They have used an equation to estimate the energy level of each process parameters and thereafter correlated this energy level with resultant microstructure and mechanical properties. The results indicated a marginal coarsening in the grain of aluminum matrix associated with a higher energy level. In addition, better dispersion of CNTs in the matrix was observed at higher energy level which resulted in better mechanical properties. Cao et al. [50] have reinforced AA5052 with carbon fiber using FSP in which tool travel speed was increased from 50 to 100 mm/min while

maintained tool rotation speed at 1000 rpm. Obtained results showed superior properties for the composite manufactured at 75 mm/min and 1000 rpm.

2.3 Friction stir processing of 6061 AA

Graphene nanoplatelets have been added successfully to 6061 AA via friction stir processing using novel multiple micro channel reinforcing approach and subsequently its impact on microstructure and mechanical properties have been outlined by Sharma et. al [51] . The results have shown that as compared to the conventional single channel technique, both tensile and microhardness have been improved by approximately 28 and 84 % respectively while the yield strength slightly declines. Sharma et al. [52] have investigated the influence of adding different fillers such as SiC, CNTs and GNPs to 6061 AA either in a binary or in a unitary phase on microstructure, microhardness and tribological behavior. The results have shown a homogenous distribution of GNPs in the aluminum matrix. In addition, an appreciable improvement by approximately 36 % in microhardness was observed in Al-SiC- GNPs composite. Moreover, the later composite has demonstrated an enhancement in wear resistance by about 56% compared with the base sample. Sharma et al. [53] have compared the tribological performance of G, Gr and CNTs added to 6061 AA using FSP. The results have illustrated a significant improvement in wear resistant for Al-G-SiC composite by approximately 50%, whereas Al-SiC-CNTs composite have displayed a considerable deterioration. Sharma et al. [54] compared mono and hybrid SiC and Gr added to 6061 AA via FSP and concluded a better mechanical properties for hybrid composite when compared with mono composite and the base sample.

Maurya et al. [55] have successfully reinforced 6061AA by different carbonaceous particles such as CNTs, Gr and G using FSP and have investigated the mechanical and tribological behavior of synthesized composites. The results outlined an enhancement in hardness by approximately 116%, 100% and 84% for Al-G, Al-CNTs, Al-Gr composites respectively. Moreover, a similar trend in microhardness improvement was also reported for wear resistance where the Al-G composite exhibited the highest wear resistance. Riaz et al. [56] have reinforced 6061 AA with CNTs using FSP and have studied the resultant microstructure and mechanical properties. The results have demonstrated an enhancement in microhardness and tensile strength for the developed nanocomposite with approximately 47.4 and 32.4% respectively as compared to the sample processed without powder. Balakrishnan et al. [57] have compared the microstructure and mechanical properties of zirconium particles added to 6061 AA with and without FSP. The results approved that FSP resulted in uniform dispersion of added particles. Besides, casting defects were considerably eliminated. Moreover, as compared to casted composite, FSP significantly enhanced the tensile strength which was ascribes favorable modification in microstructure. Dinaharan et al. [58] have investigated the impact of employing FSP on the modification 6061- Al_3Ti and 6061-Al_3Zr prepared via casting. The results have revealed a significant improvement in the dispersion of reinforced particles. Moreover, substantial enhancement in both microhardness and wear resistance for friction stir processed samples over the casted 6061, casted 6061- Al_3Ti and casted 6061-Al_3Zr. Similarly, Balakrishnan et al. [59] have successfully utilized FSP to modify AA6061-Al_3Fe composite fabricated via casting.

The results have shown a homogenous dispersion of added particles after FSP as well as elimination of cast defects. Moreover, severe plastic deformation caused by FSP and pinning effect of added particles resulted in considerable reduction in grain size and subsequently enhanced tensile strength.

Dinaharan et al. [60] have fabricated AA6061-rice hush ash composite using FSP and have studied the microstructure and tensile strength of the synthesized composite. The results have revealed homogenous grain structure for the composite and uniform dispersion of added particles which resulted in substantial enhancement in tensile strength compared with that for aluminum matrix. Likewise, Dinaharan et al. [61] have used FSP to alter AA6061- Al_2Cu composite fabricated via casting and have investigated microstructure and tensile strength. The results have illustrated a homogenous microstructure and uniform dispersion of reinforcement particles after deploying friction stir processing. Additionally, the tensile strength of the composite considerably improved after FSP. Barati et al. [62] have evaluated the effect of the combination of vibration and FSP of AA6061-SiO_2 composite on microstructure, tensile strength and corrosion resistance compared to the base sample and conventional FSP. The results have shown a decline in grain size for the sample processed with a new approach by approximately 38% compared to conventional friction stir processed sample. Additionally, the FSP sample have exhibited the highest corrosion rate followed by the base sample, while combining vibration to FSP results in reducing the corrosion rate by about 87%. Moreover, tensile strength and wear resistance was the highest for the sample processed with a new novel technique. Zhang et al. [63] have

modified casted AA6061-ZrB_2 using several passes of FSP and have investigated the new microstructure and mechanical properties. The results have revealed a considerable enhancement in microstructure homogeneity after FSP. Besides both microhardness and tensile strength increases regularly with rising number of passes.

Aruri et.al [64] have compared AA6061- SiC-GR and AA6061 SiC- Al_2O_3 hybrid composites synthesized via FSP at different rotational speeds. Their results have demonstrated that the highest microhardness was for AA6061-SiC-Al_2O_3 at the lowest rotational speed and that was attributed to the pinning effect of Al_2O_3 and SiC. On the other hand, the highest wear resistance was for AA6061-SiC-Gr composite which was interpreted by the load-bearing capacity of SiC and lubricant film of Gr. Moreover, presence of brittle reinforcement resulted in reduction in tensile strength compared to base metal

Devaraju et al. [65] employed Taguchi methodology to address the influence of rotation speed, reinforcement type and fractions therein on mechanical properties and wear resistance of friction stir processed AA6061-SiC-Gr. The finding revealed that the rotation speed was the major contributor in most properties. Furthermore, the pinning effect and lubrication film made by SiC and Gr caused a significant enhancement in hardness and wear resistance respectively.

Taguchi methodology was employed to optimize rotation speed and relative powder fractions of SiC and Al_2O_3 which added to AA6061 using FSP by Devaraju et.al [66]. The

results illustrated a uniform dispersion of reinforcement powder in aluminum metal matrix. In addition, a significant deterioration in strength was observed for all processed samples. However, considerable improvement was detected for hardness as well as wear resistance.

Devaraju et al. [67] compared the performance of AA6061-SiC- Al_2O_3 with AA6061-SiC-Gr composites fabricated using friction stir processing. The finding showed that the soft phase of Graphite was the main reason for microhardness reduction; nevertheless, this solid phase contributed toward coefficient of friction reduction and thereby enhancing the wear resistance.

In situ approach was employed to fabricate Al6061-Cr_2O_3 using plasma spray and consequently friction stir processing was applied on the surface [68]. The powder was distributed uniformly along the nugget zone and no defects were captured. Friction stir processed sample without powder demonstrated the poorest wear performance and that was attributed to the loss of precipitation hardening which was caused by the process. However, the highest wear resistance was observed at aluminum reinforced sample and that was interpreted by the presence of hard ceramic in the aluminum matrix.

Sharma et al. [69] synthesized AA6061- B_4C- MoS_2 composite using FSP and studied the performance of each mono composite as well as binary composite with different relative fractions on microstructure, microhardness and wear resistance. The results indicted uniform dispersion of reinforcement particles without agglomeration. In addition, mono composite AA6061-B_4C exhibited the highest microhardness; however, with modifying

the composite by introducing 25% - vol. of MoS_2, a considerable reduction in hardness was noticed meanwhile, the highest wear resistance was obtained due to the incorporation of this solid lubricant that reduced metal to metal contact. Moreover, a noticeable decrement in hardness and wear resistance in the friction stir processed sample without powder which owed to the dissolution of strengthening precipitates.

Kheirkhah et al. [2] have incorporated BN to 6061 AA via FSP and have studied the resultant structure and subsequent mechanical properties as well as corrosion behavior. The results have revealed a homogenous dispersion of reinforced particles over the aluminum matrix. Additionally, an enhancement in microhardness with approximately 62% and 23% for samples processed with and without adding BN particles respectively as compared with the base metal. Moreover, the corrosion resistance for the composite surface was substantially higher than that of the friction stir processed surface and base metal.

Kishan et al. [70] have investigated the impact of volume fraction of TiB_2 nanoparticles incorporated to AA6061 via friction stir processing and have assessed wear resistance microstructure, and mechanical properties of the resultant surface composite. It was observed that all processed samples exhibited a lower tensile strength as compared to the as-received specimen. Nevertheless, both microhardness and wear resistance for all processed samples were higher than that of as-received material. Particularly, TiB2-8% volume fraction showed the highest microhardness among all samples; whereas, the highest wear resistance was observed at TiB2-4% volume fraction.

Dinaharan et al. [71] have incorporated waste fly ash into the AA6061 matrix using FSP have inspected the impact of different volume fractions on mechanical properties, microstructure and wear resistance. The finding illustrated that a higher volume fraction yielded favorable properties. Besides the pinning effect of fly ash particles, an intense plastic deformation has contributed to a further reduction of grain size and hardness improvement and therefore wear resistance enhancement.

Rejil et al. [72] have addressed the impact of different fractions of TiC-B_4C added to AA6360 using Friction stir processing on both microstructure and wear resistance. They have found a uniform dispersion of ceramic reinforcements in the aluminum metal matrix. In addition, the film formation at an equal relative fraction of particles caused in a significant enhancement in wear resistance.

Mehta et.al [73] utilized friction stir processing to incorporate B_4C to Al-6061. Their study was aimed to assess the effect of change the stirring direction during multi-passes on microstructure, hardness and wear behavior. They indicated that reverse the traveling direction played an essential role in the improvement of particle distribution and refinement. As a result, the surface of the sample fabricated through reversing of the traveling direction showed the best hardness and wear performance

Rathee et al. [74] conducted an evaluation study to optimize tool over plunging depth during the fabrication of AA6061-SiC using FSP. Six tools over plunging depth were used, ranged from 0.1 mm to 0.35mm. The results specified 0.25 mm as an optimum plunging

depth, while a higher over plunging depth caused a sticking of tool to the workpiece and powder scattering. Moreover, a tool with lower over plunging depth resulted in low contact between the workpiece and tool and thus low heat generation which had a great contribution to poor material flow and therefore cavities formation.

2.4 FSW of Al-Li alloys

Among aluminum alloys, the third generation of aluminum lithium alloys (Al-Li-Cu-X) has been considered as a highly promising material for aerospace applications. This is mainly due to its superior properties as compared to other aluminum alloys such as outstanding properties at low temperatures, good corrosion resistance, low density, superplasticity, high fracture toughness and enhanced specific strength [75][76][77]. As compared to the previous two generations of Al-Li that exhibited unexpected failures due to either hot or cold expansion and short traverse fracture toughness which resulted in the complicated design thereby restricting applications, the new generation with the content of lithium less than 2% was able to solve the mentioned drawbacks [78][79].

Indeed, adding 1% of lithium to aluminum alloy results in increasing the elastic modulus for the alloy by approximately 6 % and this mainly attributed to the fact that lithium is one of the rare elements considered to have relatively high solubility in aluminum. Moreover, a reduction of 3% in a density of aluminum alloys is another consequence of adding 1 % of lithium. In addition, heat treatment is an influential candidate in determining precipitates which play a vital role in determining mechanical properties and corrosion resistance [76].

Wang et al. [76] have studied the effect of rising rotational speed during FSW of AA2198 from 400 rpm to 1000 rpm with an interval of 200 rpm; while the welding speed was kept unchanged of 42 mm/min, on microstructure and mechanical properties. The results have indicated that increasing rotation speed remarkably coarsening the grain in the stir zone and reducing the density of precipitates. Additionally, tensile strength has initially exhibited an improvement upon rising the rotational speed; nevertheless, a reduction in the strength was detected with further increasing of rotational speed. Bitondo et al. [80] have performed a statistical study aiming to investigate the contribution of various process parameters of traveling speed and rotation speed during friction stir welding of AA2191-T3 on yield and ultimate tensile strengths. The results have shown a great dependence of ultimate strength on tool rotational speed compared to yield strength that has exhibited a strong correlation with tool traveling speed. Ma et al. [81] investigated the influence of raising the ratio between rotation speed and traveling speed on microstructure, fatigue behavior and mechanical properties. The results showed finer equiaxed grain in the stir zone area that becomes wider upon increasing the ratio. In addition, with rising the ratio, the strength of the joint, as well as microhardness, revealed significant reduction. Moreover, similar crack growth rates were observed at different ratios.

Muthumanickam et al. [82] have studied the impact of both traveling speed and rotation speed on microstructure and mechanical properties during friction stir welding of AA2195. The obtained results have indicated that for both the highest and lowest rotational speed defect-free zone was not detected. In addition, more grain refinement was observed with

either rising traveling speed or reducing rotation speed. Moreover, the influence of tool traveling speed on tensile strength found more pronounced compared to rotation speed.

2.5 Research gap

It is evident from the previous literature that most of the conducted work was focused to enhance various mechanical, tribological and corrosion characteristics through adding ceramic particles to the aluminum metal matrix using FSP. Metal matrix fabrication using FSP has several advantages over other conventional approaches where the fabrication temperature is beneath the melting point. Nevertheless, it is believed that varying process parameters have a great contribution to the heat input which markedly alters microstructure and thereby changing different properties. It is to be noted that varying process condition i.e. plunging depth, tilt angle, shoulder features, pin shape, pass number, the direction of passes, processing speed and rotational speed was not getting the same attention for various aluminum alloys when compared with composite fabrication. Additionally, the investigation of electrochemical behavior after FSP is scarce as compared to the mechanical and tribological properties. It is worthy to mention that the processing of aluminum surfaces gathered a lot of attention because of high availability of aluminum metal and its relatively poor surface properties. Therefore, enhancing surface characteristics would widen the usage of these alloys. Hence, FSP was performed on two aluminum alloys i.e. Al-Cu-Li and Al-Mg-Si, and subsequently the change in different properties associated with the process was investigated.

CHAPTER 3

EXPERIMENTAL PROCEDURE

3.1 Workpiece material

In the current study, 6061 AA and 2099 AA with 6 mm in thickness and 120, 60 mm in length and width respectively was utilized. The chemical composition for the 6061 and 2099 aluminum alloys was obtained using a spark atomic emission spectrometer and presented in Table 3- 1 and Table 3-2 respectively.

Table 3- 1 Elemental composition of 6061 AA

Element	Mg	Si	Cu	Fe	Mn	Al
wt%	0.82	0.71	0.23	0.63	0.14	Bal.

Table 3- 2 Elemental composition of 2099 AA

Element	Cu	Li	Mg	Mn	Zn	Zr	Al
wt%	2.65	1.75	0.25	0.28	0.7	0.1	Bal.

3.2 Equipment

Research-based friction stir welder machine (RM-1-MTI, USA) is shown in Figure 3- 1 was used to carry out the surface modification. Further, this machine is equipped with a CNC operation system and built-in data acquisition system to record different forces and the torque generated during the process. To process 6061 AA surface, pinless tool with two circular grooves shoulder of 23 mm (see Figure 3-2) was used. The tool was made from tool steel 4041 and heat-treated to achieve a hardness level of 54 HRC. On the other hand, an 11.5 mm diameter H13 tool steel shoulder with 6 mm pin diameter and 5.3 mm pin length (see Figure 3- 3 (a)) was used to process the surface of 2099 AA.

Figure 3- 1 RM-1 FSW machine

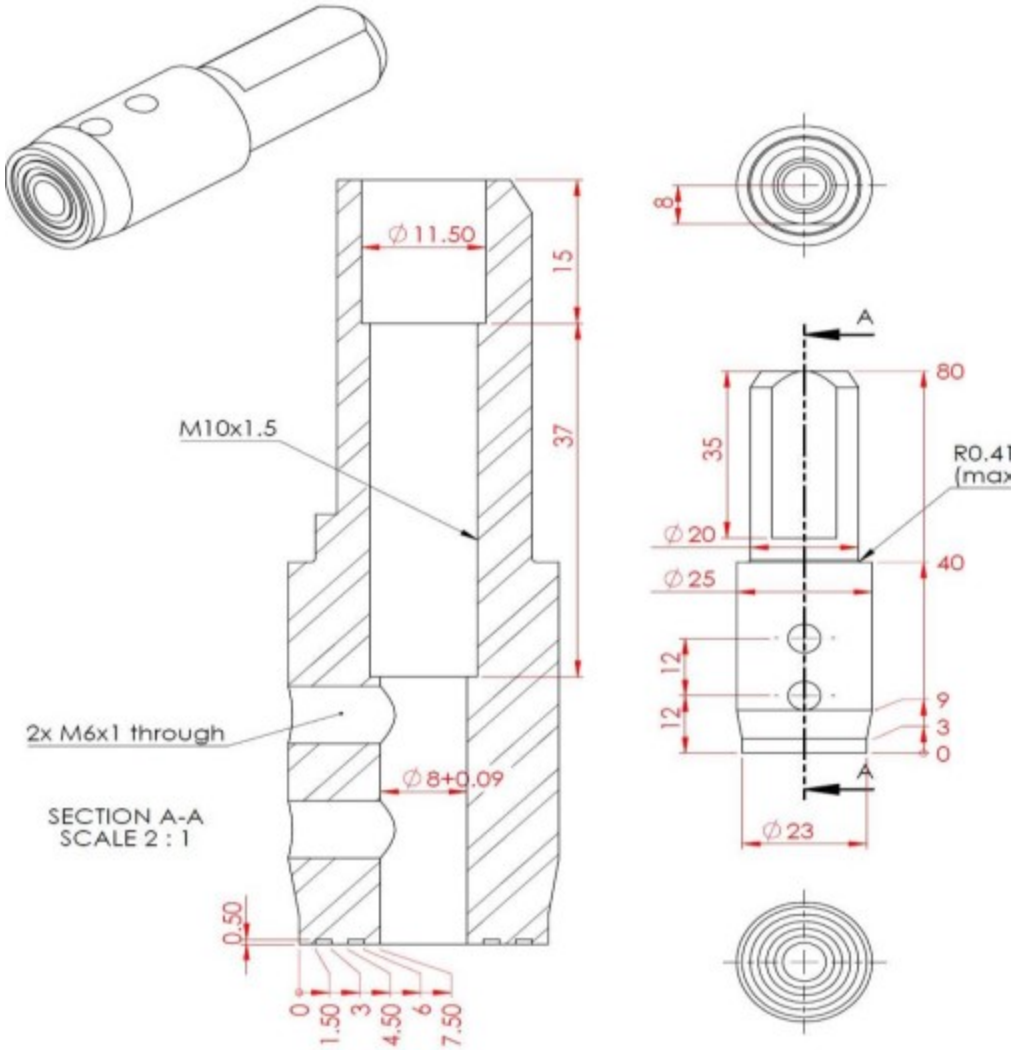

Figure 3- 2 FSP pin-less tool for 6061 AA

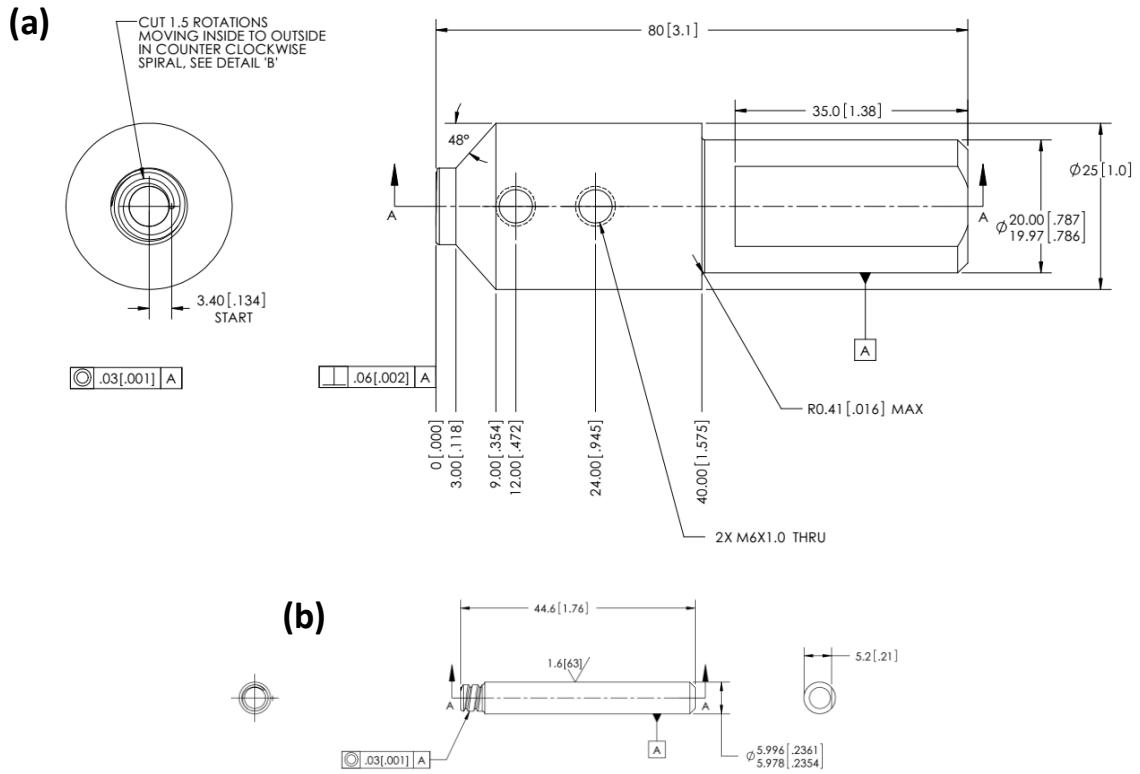

Figure 3- 3 (a) FSP tool for Al-Li alloys, (b) FSP Pin

3.3 Electrochemical analysis

All electrochemical measurements were performed on the base sample as well as processed samples using typical three-electrode cell: consisting of a sample as a working electrode, Graphite as a counter electrode and saturated calomel electrode (SCE) as a reference electrode; as seen in Figure 3- 4. Gamry instrument (Reference 3000) potentiostat; shown in Figure 3- 5 was utilized for the data collection and analysis while Echem Analyst 6.0 software was used to fit electrochemical data. All samples were cut into a suitable size and then ground using silicon carbide paper up to 400 grit to eliminate the surface roughness effect and thereafter samples were masked using Gamry masks and only 1 cm^2 of the

processed zone was exposed to 3.5 % NaCl solution at 23° C. Prior to performing the corrosion tests, all samples were cleaned using a distilled water. The polarization was carried out in an applied potential varying from -25 mV cathodically to 25mV anodically with respect to the open circuit potential (E_{OCP}) at scanning rate of 0.125 mV/s. Electrochemical impedance spectroscopy (EIS) tests was carried out using a frequency ranging from 10^{-2} to 10^{5} Hz with an AC voltage of 10 mV. Finally, the potentiodynamic polarization experiments were carried out between ±0.25 V at a scanning rate of 0.25 mV/s. Thereafter, corrosion potential and corrosion current density were determined using the Tafel extrapolation method.

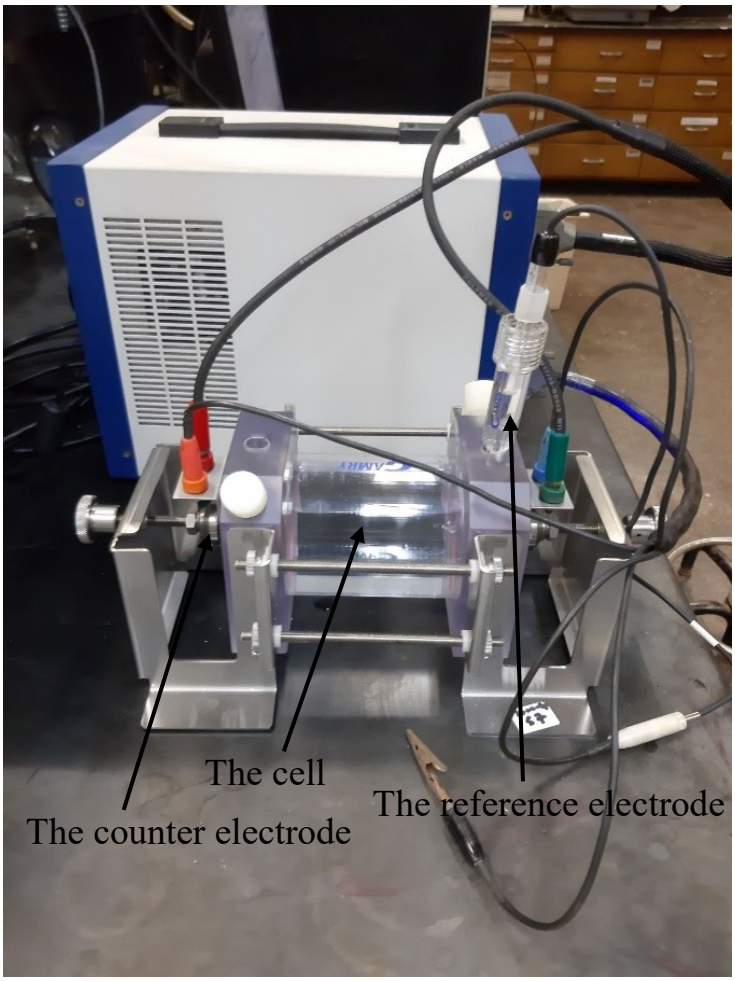

Figure 3- 4 Gamry Paracell for flat samples

Figure 3- 5 Gamry Potentiostat

3.4 Mechanical properties

In order to assess the mechanical properties of processed and base samples, micro indenter (MicroCombi Tester, CSM Instruments, Switzerland);presented in Figure 3- 6, was used.

A pyramidal diamond indenter was used with a normal load of 200 g (2 N) for 10 seconds dwelling time, at 4 N/min loading and unloading rate. A minimum of 6 (2 x 3 matrix) measurements at different locations on each sample were recorded for hardness (H) and modulus of elasticity (E).

Figure 3- 6 Micro indenter equipment

3.5 Tribological evaluation

A wear test was conducted using a linear reciprocation tribometer (Docum, India) which is presented in Figure 3- 7. The configuration of the test was ball on disc under dry and room temperature conditions. Stainless steel ball was used as a counter face with 6 mm in

diameter. Prior each test the counter face ball was cleaned using acetone and subsequently dried.

Figure 3- 7 Linear reciprocating tribometer

3.6 Characterization techniques

3.6.1 Microstructural analysis

Base metal and processed samples were cut into a suitable size, thereafter grinded using silicon carbide paper with grit size varied from 240 to 800. Consequently, grinded samples were polished using Diamond Lapping Paste with size ranged from 7 to 2 µm and finally Al_2O_3 with 50 nm size was used. To etch 6061 AA, NaOH solution (2g of NaOH dissolved in 100 ml of distilled water). On the other hand, killer regent was used to etch 2099 AA.

3.6.2 Present phases

X-ray diffractometer (Advance D8 XRD, Bruker, USA) was used to assess any structural changes between the base and the processed samples. The samples were scanned from 10 to 80° at a rate of 0.02 °/s using a CuKα radiation source (wavelength of 0.15406 nm) operating at 40 kV and 40 mA.

3.6.3 Grain size

In order to determine grain size and morphology, optical digital microscope (Olympus, DSX 510, Japan) was utilized. Olympus stream software equipped to the microscope was used to calculate average grain size according to ASTM 112-13 [83].

3.6.4 Morphology of worn and corroded surfaces

To study the morphology of samples after wear and corrosion tests field emission Scanning electron microscope (FESEM) (Quanta 250, Czech Republic) equipped with energy dispersive spectroscopy was used.

3.6.5 Wear measurement

To measure the amount of material loss after wear, weight balance (phoenix instrument, Germany) was used. A minimum of three measurements were taken before and after wear test and the average value was recorded.

Samples designation:

Table 3-3 Samples designationTable 3-3 shows samples designations used in the thesis for 2099 AA and 6061 AA.

Table 3-3 Samples designation

ω (rpm)	V (mm/min)	Sample designation
400	250	400-250
600	150	600-150
800	150	800-150
800	250	800-250
1000	50	1000-50
1000	100	1000-100
1000	150	1000-150
1000	200	1000-200
1000	250	1000-250
1200	150	1200-150
1200	250	1200-250

CHAPTER 4

FRICTION STIR PROCESSING OF 6061 AA

In this chapter, the impact of friction stir processing on microstructure, mechanical properties, corrosion resistance and wear behavior of Al-Mg-Si alloy (6061AA) was studied in detail.

4.1 Effect of changing traveling speed

4.1.1 Generated torque

. Figure 4- 1 shows the effect of raising traveling speed from 100 mm/min to 250 mm/min on the generated torque. It can be observed from the figure that increasing traveling speed results in torque raising. Also, it is evident from the graph that either increasing traveling speed by 50 mm/min (from 100 to 150 mm/min) or by 100 mm/min (from 150 to 250 mm/min), the generated torque appreciably increases. The considerable increase in torque with traveling speed increasing can also be attributed to flow stress raising [87].

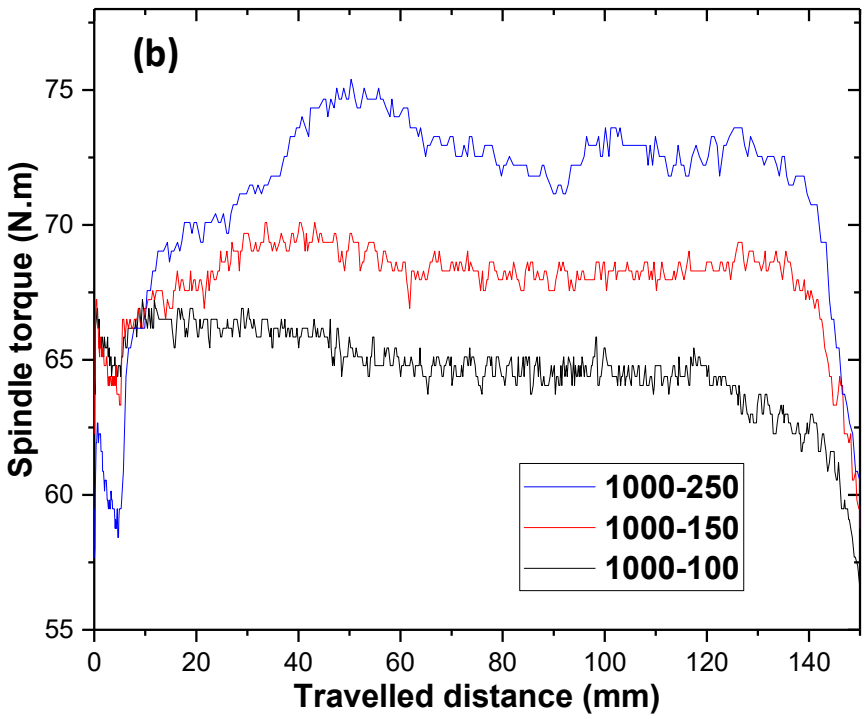

Figure 4- 1 Effect of traveling speed on generated torque

4.1.2 Microstructural analysis

The optical microscopic images of the processed surface for the samples fabricated at various traveling speeds, namely 100, 150 and 250 mm/min and as received sample (base) are presented in Figure 4- 2 (b), (c), (d) and (a), respectively. It is to be noted that the only source of heat during this investigation was due to the tool shoulder interaction with the workpiece material. As compared to the base metal, samples processed at different traveling speeds exhibited substantial grain refinement. In addition, the measured mean grain size for the base metal was 93.93 µm and after processing became 17.74, 16.38 and 15.58 µm for the 1000-100,1000-150 and 1000-250 samples, respectively as depicted in Table 3. The grain refinement with increasing traveling speed during friction stir

processing was extensively reported in the literature and was attributed to heat input reduction. It worthwhile to know that quantitative analysis of heat input did not establish yet; nevertheless, for specific process parameters. It is evident that rising tool traveling speed under constant rotation speed results in heat input reduction whereas increasing tool rotation speed and fixing tool traverse speed results in increase heat input during friction stir processing and vice versa. Accordingly, the heat input for each process parameter may calculate using the measured torque, rotating speed and traveling speed using eq. 4.1.

$$H = \frac{P}{v} = \frac{T.\omega}{v} \tag{4.1}$$

Where H is heat input in J/mm, T is the average spindle measured torque in N.m, ω is tool rotation speed in rad/s, v is tool traveling speed in mm/s.

Table 4- 1 Effect of process parameters on generated torque, heat input, and grain size

SAMPLE	Torque (N.m)	Heat input (J/mm)	Grain size (μm)
1000-100	65	4084.07	17.74
1000-150	68	2848.38	16.38
1000-250	72	1809.56	15.53

Correspondingly, heat input and mean grain size for the processed samples are presented in Table 4- 1. The obtained results are consistent with what was carried out in the literature. For example, Zhang et al. [49] have incorporated CNTs to a commercial aluminum 1060 via FSP and have concluded that finer grains were obtained under different process parameters; however, increasing heat input has resulted in a marginal coarsening of grains. Likewise, Azizieh et al. [88] fabricated AZ31/Al_2O_3 composite using FSP and reported that

with increasing rotation speed, the heat input improves and therefore grains size increases. Similarly, Moghaddas et al. [89] have investigated the impact of the thermal condition during friction stir processing of Al5754 and have demonstrated that with either reducing rotating speed or rising traveling speed, more grain refinement can be obtained. Various restoration mechanisms were proposed for grain refinement during friction stir processing/welding of aluminum and alloys therein, namely discontinuous dynamic recrystallization (DDRX), dynamic recovery (DRV) and geometric dynamic recrystallization (GDR)[90]–[93]. It should be emphasized that the peak temperature of friction stir welding/processing plays a vital role in determining grain size according to recrystallization principles [94]. Therefore, grain size decreases either with increasing of traveling speed or with rotation speed reduction [95].

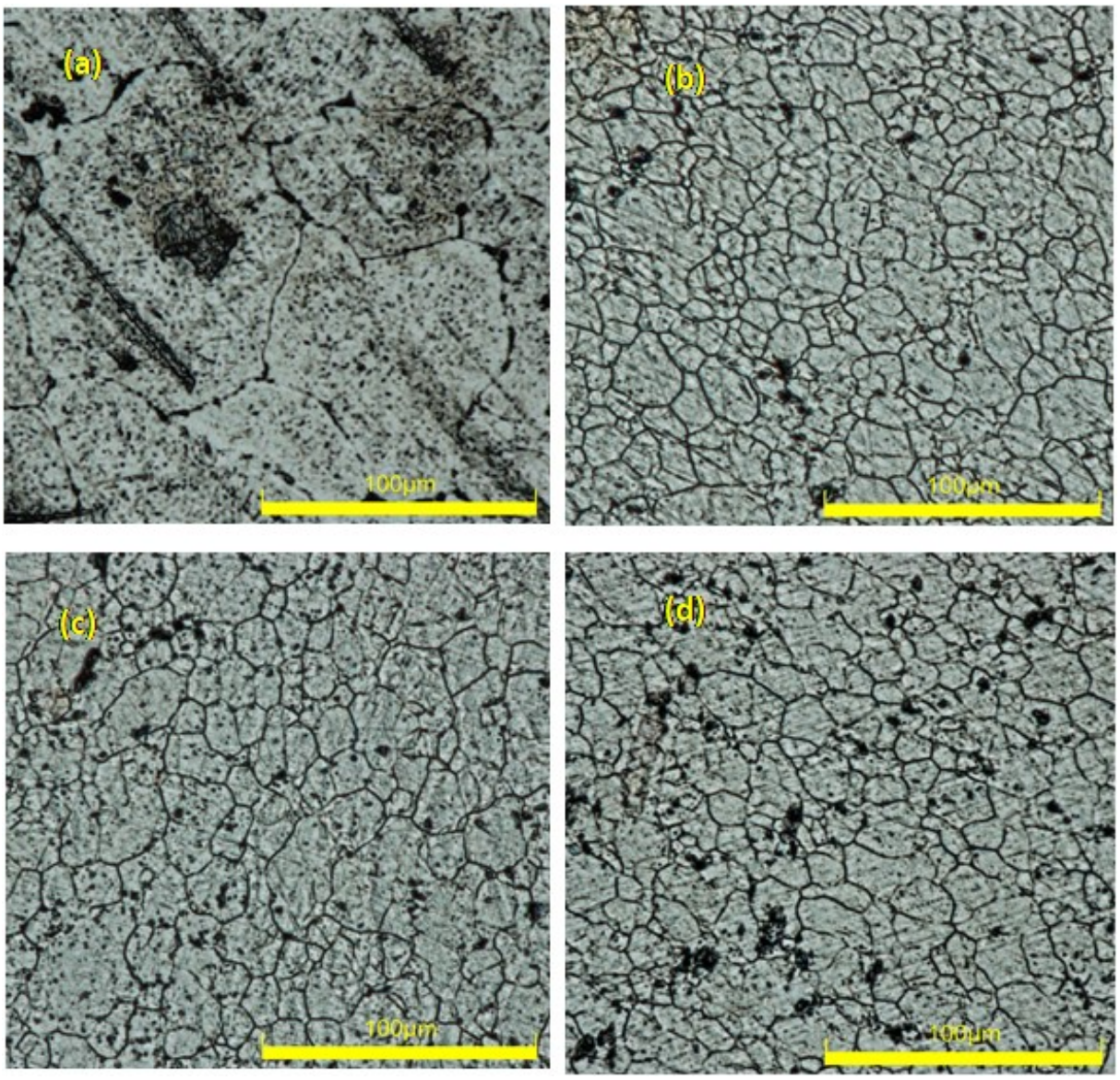

Figure 4- 2 Representative grain of (a) base, (b) 1000-100, (c) 1000-150, (d) 1000-250

4.1.3 XRD

Figure 4- 3 shows the influence of FSP on 6061 AA, where welding speed increased from 100 up to 250 mm/min on XRD patterns. As obviously depicted in Figure 4- 3 (a), only four aluminum matrix peaks were detected which proves that no intermetallic phases have been formed due to the high frictional heat. Fundamentally, the diffraction method is only able to catch phases with a minimum volume fraction of 2 % and therefore other peaks of alloying elements were not detected [96]. Interestingly, samples after processing showed an appreciable shift toward high 2θ and the sample processed at the highest processing speed showed the most pronounced shift as clearly presented in Figure 4- 3 (b). To our knowledge, a shift in aluminum peaks after FSP was not reported before, it is however reported for magnesium and copper after FSP. This phenomenon of peaks shifting was ascribed to the reduction in lattice parameters which caused compressive strength [97][98].

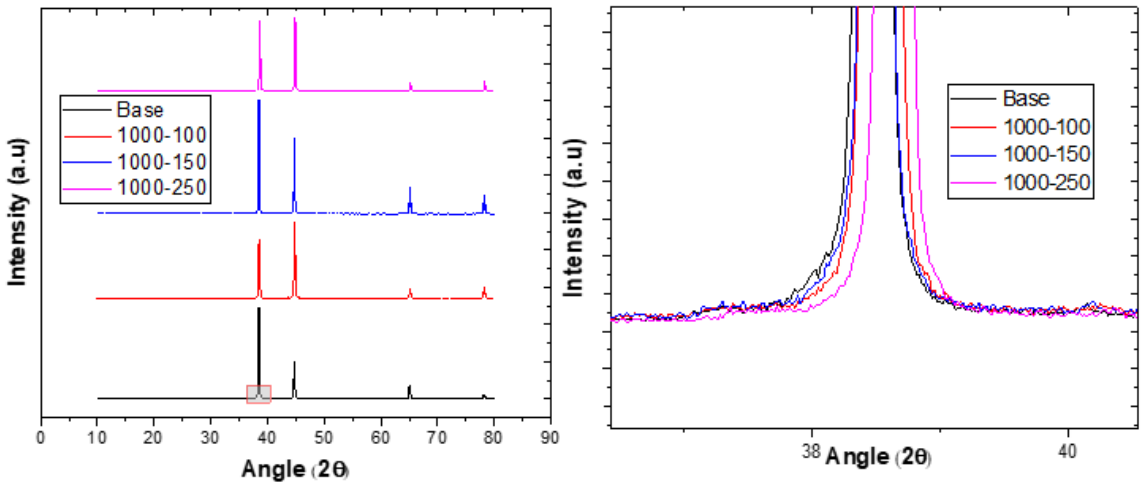

Figure 4- 3 XRD patterns for all sample before and after FSP at different traveling speeds

4.1.4 Micro-hardness and elastic modulus

Figure 4- 4 shows the effect of varying traveling speeds during FSP of 6061 AA on microhardness and elastic modulus. The microhardness and elastic modulus of the base sample were obviously much lower when compared with the processed samples, irrespective of the process parameter. The microhardness of the base sample is around 50 HV whereas, for the samples processed at 100, 150 and 250 mm/min are approximately 97, 74 and 70 HV. Interestingly, the hardness of the sample processed at the lowest traveling speed is almost two times that of the base metal. In addition, the elastic modulus of the base sample is around 64 GPa while after performing FSP at the lowest speed the elastic modulus increased to around 68 GPa. Moreover, the elastic modulus for the samples processed at moderate and the high speeds showed only marginal improvement to approximately 70 GPa. The enhanced hardness is ascribed to higher heat input that resulted in the diminishing of second precipitate particles[99]. Besides, the improvement in modulus of elasticity may be attributed to dynamic recrystallization [55].

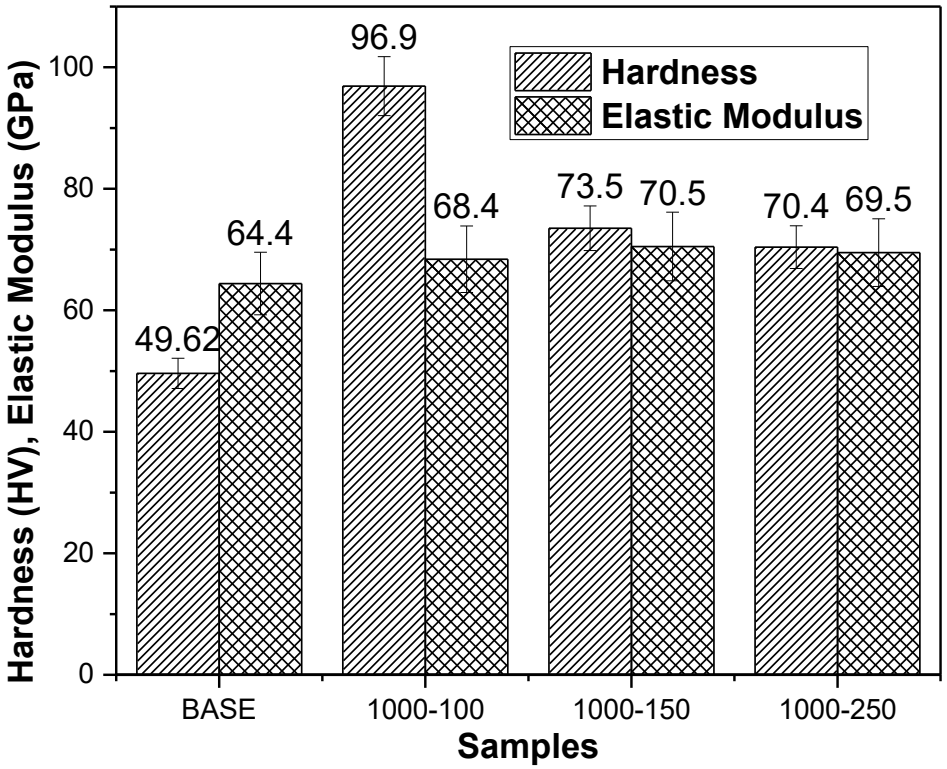

Figure 4- 4 Impact of increasing tool traveling speed on microhardness and elastic modulus

4.1.5 Electrochemical behavior.

4.1.5.1 Electrochemical Impedance Spectroscopy (EIS)

Alternating current impedance approach was implemented extensively in the investigation of the metal-electrolyte border, treatment of surfaces, oxides films, kinetics, mechanism analysis, and corrosion of coating on the metallic substrates [100], [101]. Thus, in order to investigate the effects of friction stir processing on kinetics and characteristics of the electrochemical process, Electrochemical impedance spectroscopy (EIS) measurements were carried out on base sample and all processed samples in 3.5% NaCl solution after 15 days of immersion.

Figure 4- 5 displays Nyquist curves, phase angle, and modulus for all samples. As depicted in Figure 4- 5 (a and b), the Nyquist plots illustrate relatively a larger semicircle capacitive arc at the low-frequency region and larger counterpart at a lower frequency for the base sample; however, for (1000-100) and (1000-150) processed samples the arc becomes larger at the high-frequency region and slighter at the low-frequency region. The larger uncompleted semicircle capacitive arc for processed samples may be ascribed to the charge transfer reaction at the interface between metal, the oxide film formed and NaCl electrolyte [102]. Accordingly, the charge transfer existed where an oxide film formed at the border between the electrolyte and metal. However, the occurrence of the second uncompleted semicircle arc is attributed to diffusion-controlled processes [103]. Depression phenomenon can be clearly identified through the uncompleted semicircle behavior of arcs which is probably caused by surface heterogeneities due to corrosion products and frequency dispersion [104], [105]. As can be observed from Figure 4- 5 (a) the capacitive arc radius raises with increasing the traveling speed. In addition, the smallest radius was observed for the base sample while the sample processed with the highest traveling speed (1000-250) demonstrates the highest radius. Moreover, the variation in radius between the base sample and the sample processed at the lowest traveling speed (1000-100) was remarkably low as compared to deviation in radius between the sample processed at moderate velocity (1000-150) and that fabricated at highest velocity (1000-250). Interestingly, the variance in radius between the base sample and (1000-250) sample was not even distinguishable without zooming the base sample area in the Nyquist plot as seen

in Figures 4- 5 (a and b). A huge alteration in semi-circle radii revealed that the corrosion rate is significantly affected by the surface processing. Furthermore, increment in semi arc radii with the process is interpreted by enhancement in surface protectiveness due to the rising of stability and compactness of the passive film formed [106], [107]. Therefore, the corrosion resistance is found to improve in the order of 1000-100, 1000-150, and 1000-250, demonstrating a markedly improved resistance as compared to that of the unprocessed sample.

The impedance-frequency bode plots for all samples are presented in Figure 4- 5 (c). It is evident from the figure that total impedance for all processed samples is significantly higher than that of the base metal at the low frequency of 0.01 Hz which reflects the corrosion protection provided by the surface processing technique. In addition, total impedance revealed a rapid increment with increasing traveling speed. Moreover, the deviation in total impedance was at its low level when comparing the base metal with sample processed at the lowest traveling speed; however, with increasing traveling speed, the deviation between sample processed the intermediate speed and another at the lowest speed was much higher. Furthermore, a huge variation was observed between (1000-150) sample and the sample processed at the highest speed which indicates a superior corrosion resistance for the highest speed sample compared to all other samples.

Typical Phase angle-frequency plots for both processed and base samples are shown in Figure 4- 5 (d). It can be detected that phase angle maxima of the base sample shifted toward -78° at a frequency of 25 Hz which suggests a deterioration in the barrier stability

even at higher frequency [108]. On the other hand, (1000-100) sample demonstrated two times constant, the first time constant shifted toward -71° at the frequency of 6.4 Hz, while second-time constant shifted toward -69° at the frequency of 241 Hz. Additionally, samples (1000-150) and (1000-250) exhibited phase angle maxima shifted toward -81 and -83 and at frequencies of 8 and 0.78 Hz respectively. Moreover, it can be noticed that the base sample demonstrated the narrowest phase peak and further broadening can be observed with increasing the traveling speed which ascribed to the interaction of two times constant [109]. Furthermore, more peak broadening indicates an enhancement in a passive protective barrier over a wide frequency range and consequently corrosion resistance improvement [108][110]. It should be emphasized that shifting of phase angle maxima to a higher frequency illustrating that the corrosion would have instigated at the sample surface for the long duration [111]. Therefore, the optimum traveling speed for processing to obtain the highest corrosion resistance in 3.5% NaCl media is 250 mm/min.

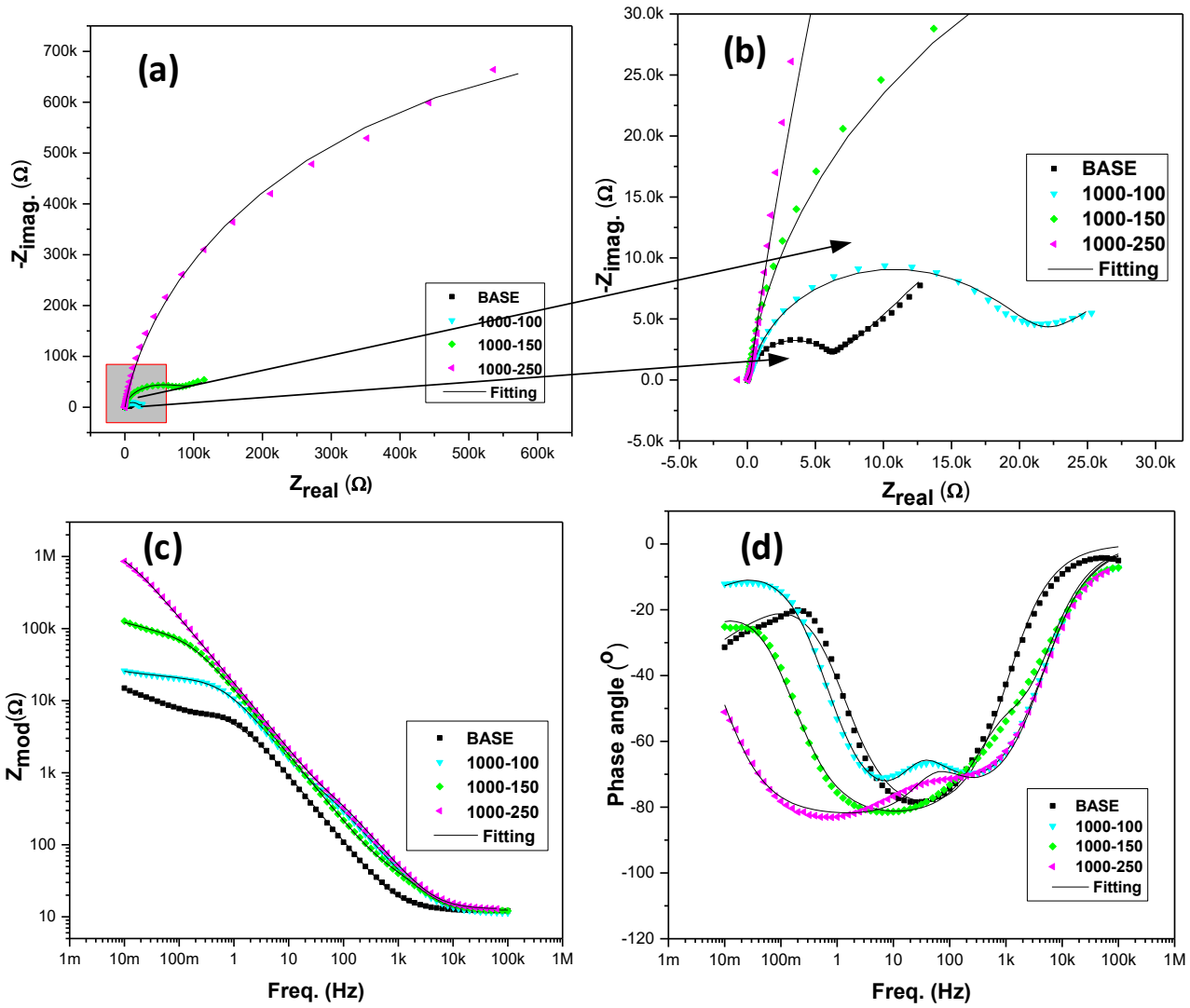

Figure 4- 5 (a,b) Nyquist plots, (c) impedance, (d) phase angle

All the impedance curves were fitted to appropriate corresponding circuits for further numerical estimation of the barrier characteristics of processed surfaces and properties of active corrosion protection. Accordingly, two equivalent circuits were used. The first one; shown in Figure 4- 6 (a), simulates the corrosion behavior at the base surface, which involves charge transfer resistance (R_{ct}) connected in series with Warburg resistance (W)

and in parallel to a constant phase element for double-layer capacitance (CPE_{dl}), while both (W, R_{ct}∥CPE_{dl}) are connected in series with solution resistance (R_S); between the reference and working electrodes. It is suggested that all processed samples contain two resistances, inner resistance and outer ones compared to the base sample which contains only one resistance. This suggest the improvement in corrosion resistance for all processed samples. The second circuit as illustrated in Figure 4- 6 (b) was used to simulate all processed surfaces contains charge transfer resistance serially connected to Warburg resistance (W) and both are in parallel with constant phase element accounting for the double-layer capacitance of the inner barrier layer(CPE_{dl}), and the mentioned three components are connected in series with film resistance (R_f). Further, W, R_{ct}, CPE_{dl}, and R_f are parallelly connected with the constant phase element of the outer passive film (CPE_f), and the previous circuit is serially connected with the solution resistance between reference and working electrodes (R_S).

It is worthwhile to know that constant phase elements were utilized as an alternative of pure capacitance because of non-ideal capacitive behavior indicated by the deviation in phase shifts from 90°. Therefore, double-layer capacitance (C_{dl}) for a cell containing a constant phase element (CPE) may be calculated from eq. 4.2

$$C_{dl} = Y_0 \, (\omega_{max})^{n-1} \qquad (4.2)$$

Here, ω_{max} is frequency when the imaginary part of impedance at its maximum value, Y_0 is the constant phase element component (admittance) and n is value corresponding to the surface roughness.

It can be seen from Table 4-2 that the double-layer capacitance (C_{dl}) of the constant phase element exhibits a significant reduction for all processed samples as compared to the base material and the order of decrease is (1000-100), (1000-150) and (1000-250). The dual-layer between the charged aluminum surface and 3.5 % NaCl is reflecting an electrical capacitance behavior [112]. Accordingly, the reduction in capacitance for the processed surfaces indicates a corrosion resistance enhancement with traveling speed changing which can be attributed to a rapid decrease in surface activeness resulted from the formation of a passive film [113][114]. In this regard, Deng et al. [115] interpreted the reduction in CPE by the improvement in electrical double layer thickness and/or local dielectric constant diminishing. Accordingly, the thickness of the passive film (t) may be calculated using the Helmholtz model [116] (eq. 3)

$$t = \frac{\varepsilon\, \varepsilon_0}{C_{dl}} \qquad (4.3)$$

where C_{dl} refers to double-layer capacitance (μF),ε_0 stands the vacuum permittivity (8.85e-14 F cm^{-1}[117]), ε represents passive layer dielectric constant (for aluminum, $\varepsilon = 10$)[117].

As illustrated in Table 4- 2, charge transfer resistance (R_{ct}) exhibited a rapid increment for all processed samples over the base material. Moreover, it is evident from the table that

charge transfer resistance rapidly increases with an increase in traveling speed which can be ascribed to the passive film formed at the metal-electrolyte interface. The presence of this film isolated aluminum metal surface from corrosion ions attack and thereby obstructing further transfer of charge or mass [118]. It should be noted the there is a remarkable difference between charge transfer resistance (R_{ct}) and film resistance (R_f) particularly if processing was carried out at higher speed which may be attributed to oxide film formed which took the key role in corrosion protection at a particular speed [119]. Moreover, the huge variation between the outer and inner resistances indicates that the resistance provided by the inner barrier is much higher when compared with the outer film [120].

Generally, Warburg resistance is added to stimulate the diffusion effect as indicated by the straight line close to 45° to the impedance imaginary axis. Comparing Warburg impedance, it is obvious from the table that the lowest Warburg resistance was obtained at the highest traveling speed of 250 mm/min and with reducing traveling speed to 150 mm/min, Warburg impedance demonstrated a slight increment. Moreover, with further reduction in traveling speed down to 100 mm/min, a considerable improvement in Warburg impedance was observed which is relatively comparable with the base metal. A lower Warburg value indicates a reduction in the diffusion of chloride ions through an oxide passive film and thereby improving corrosion resistance [121][111].

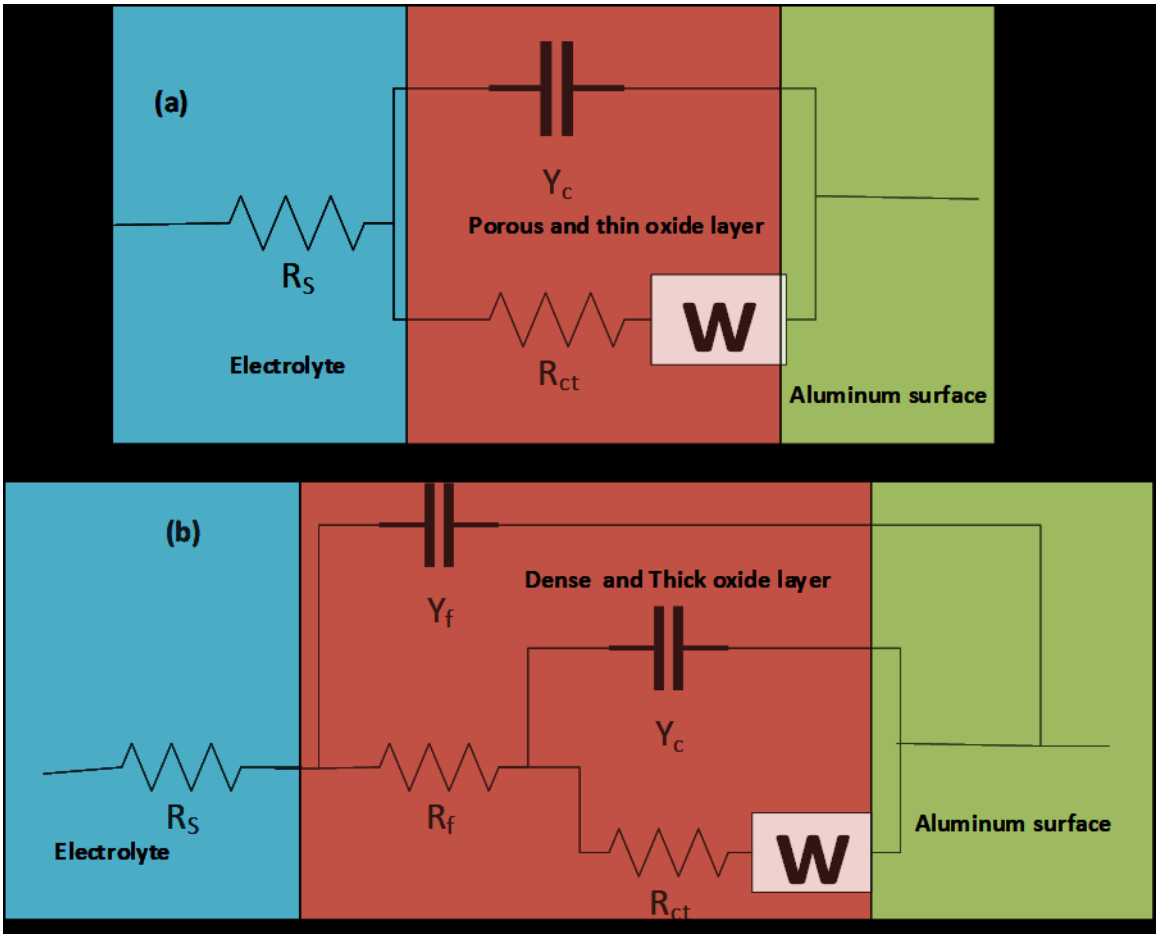

Figure 4- 6 Equivalent circuits for (a) base, (b) processed samples

Table 4- 2 Electrochemical parameters obtained from EIS plots

Samples	Rs (Ω)	Y_n*10^{-6} (S*s^a)	n	Rf (kΩ)	Y_c*10^{-6} (S*s^a)	c	R_{ct} (kΩ)	C_{dl} (μF)	$W*10^{-5}$ S*s^(1/2)
Base	12.38				23.5	0.924	6.14	33.3	41.4
1000-100	11.26	10.94	0.878	1.59	3.92	0.92	18.7	11.6	56.7
1000-150	12.24	6.94	0.921	0.088	5.25	0.93	83.9	9.99	7.26
1000-250	12.79	4.43	0.892	1.72	2.16	0.95	1500	7.28	4.20

4.1.5.2 Potentiodynamic polarization (PDP)

The typical potentiodynamic polarization curves after 15 days of immersion in 3.5 % NaCl solution are presented in Figure 4- 7. Various electrochemical parameters such as anodic Tafel slope (β_a), cathodic Tafel slope (β_c), corrosion current density (I_{corr}), and corrosion potential (E_{corr}) for the base sample as well as processed samples derived from potentiodynamic polarization curves are depicted in Table 4- 3. Polarization curves exhibited significant differences between all samples. As can be noticed from Figure 4- 7, there is a considerable variation in corrosion potential between the base and processed samples. It is evident that from Figure 4- 7 and Table 4- 3 that with an increase in traveling speed, corrosion potential (E_{corr}) is shifted to a more positive noble position. Moreover, 1000-100 sample exhibited the highest corrosion potential compared to 1000-250 sample that showed the noblest behavior among all processed and base samples. This shift to a noble direction is an indication of the improvement in corrosion resistance. Further, as can be inferred from Figure 4- 7 and Table 4- 3, the corrosion current density (I_{corr}) for all processed samples was lower than that of the base metal. Additionally, a further reduction can be observed as traveling speed increases. Diminish in $I_{corr.}$ is strong evidence that friction stir processing for 6061 AA enhanced the corrosion resistance. Furthermore, the ratio between corrosion current density for the worst sample (base) to the best sample (1000-250) is in the order of magnitude 600 which indicated outstanding corrosion protectiveness for 1000-250 sample. Also, as compared to a base sample, the pitting potential of 1000-250 sample raised from -780 mV to -600 mV which suggested an enhancement in pitting resistance.

A remarkable variation in cathodic and anodic Tafel slopes can be detected after the inspection of Table 4- 3. Particularly anodic behavior revealed that unprocessed sample had less tendency to be oxidized as compared to all processed samples where β_a value for the unprocessed sample was the highest and a further reduction in the anodic slope can be noticed with traveling speed increasing which suggest an improvement in oxidation tendency [122].

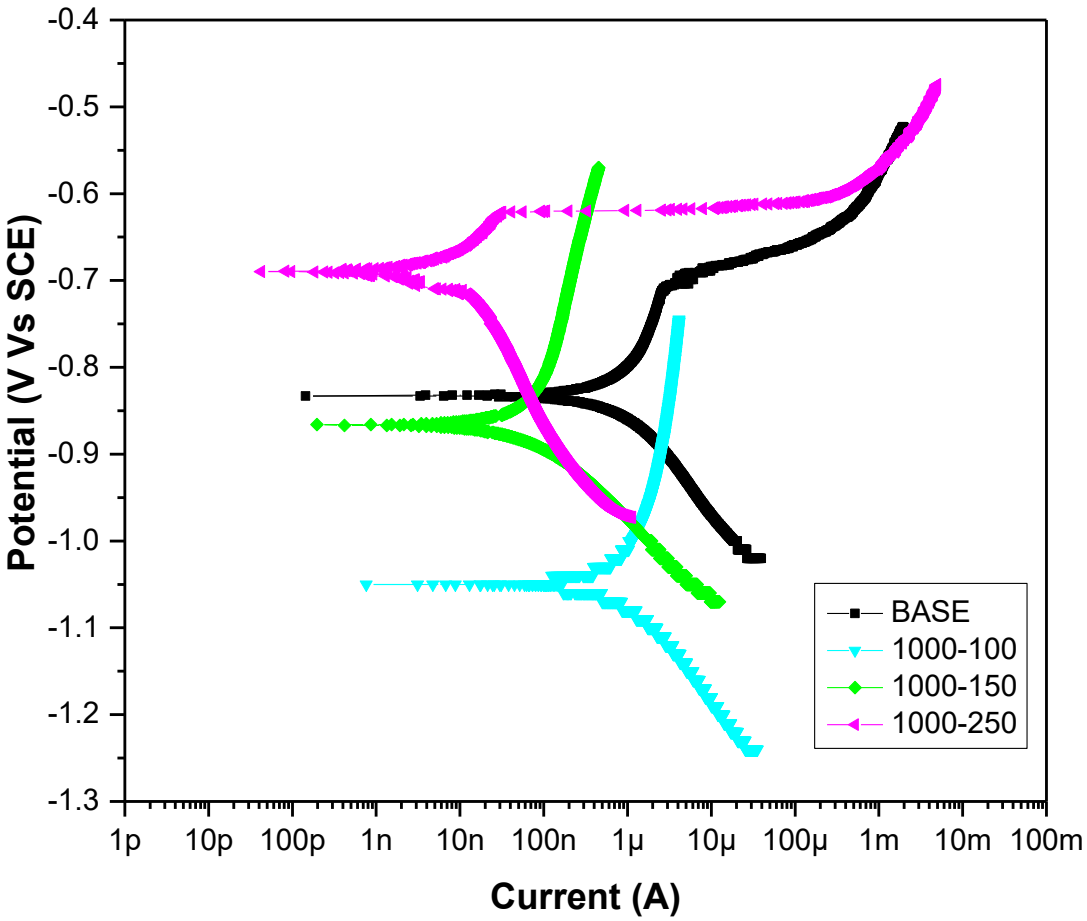

Figure 4- 7 Typical PDP curves for all samples after 15 days of immersion in 3.5% NaCl

Table 4- 3 Electrochemical parameters obtained from PDP plot

Samples	β_a	β_c	I_{corr} (μA)	E_{corr} (V)	corrosion rate (mpy)
Base	1.994	2.78E-01	3.28	-0.832	1.498
1000-100	7.38E-01	1.68E-01	1.7	-1.05	7.79E-01
1000-150	6.57E-01	1.10E-01	1.12E-01	-0.867	5.11E-02
1000-250	8.69E-02	7.60E-02	5.47E-03	-0.693	2.50E-03

4.1.5.3 Linear polarization resistance (LPR)

Linear polarization plots for different samples (processed and base) after 15 days of immersion in 3.5 % NaCl are presented in Figure 4- 8. The polarization resistance (R_P) was obtained as a slope of potential with the current. To calculate the corrosion current density based on the linear polarization resistance approach, the Stern Geary equation was utilized which correlated the current density (I_{corr}) with polarization resistance (RP) according to eq 4.4 [123].

$$I_{corr} = \frac{\beta_a \beta_c}{2.303\ R_P(\beta_a \beta_c)} \qquad (4.4)$$

Where R_p is polarization resistance obtained from LPR slope, β_c, β_a are the cathodic and anodic Tafel slopes derived from PDP curves.

Subsequently, to calculate the corrosion rate (mpy), eq. 4.5 was used

$$CR = \frac{0.131 * I_{corr} * EW}{\rho} \qquad (4.5)$$

Where **ρ** is the sample density, EW sample equivalent weight.

As indicated in Table 4- 4, the corrosion current density for all processed samples was lower than that of base metal counterpart. Additionally, the highest polarization resistance was obtained for sample processed at the highest speed and further reduction can be observed with traveling speed reduction. It should be emphasized that polarization resistance is proportional to corrosion resistance and therefore a sample with the highest polarization resistance exhibited the highest corrosion resistance.

All the linear polarization resistance results above demonstrate a strong consistency with the results obtained from Electrochemical impedance spectroscopy (EIS) and potentiodynamic polarization without a major difference where the base sample shows the highest corrosion susceptibility and after employing FSP further increment in corrosion resistance was observed upon rising tool traveling speed.

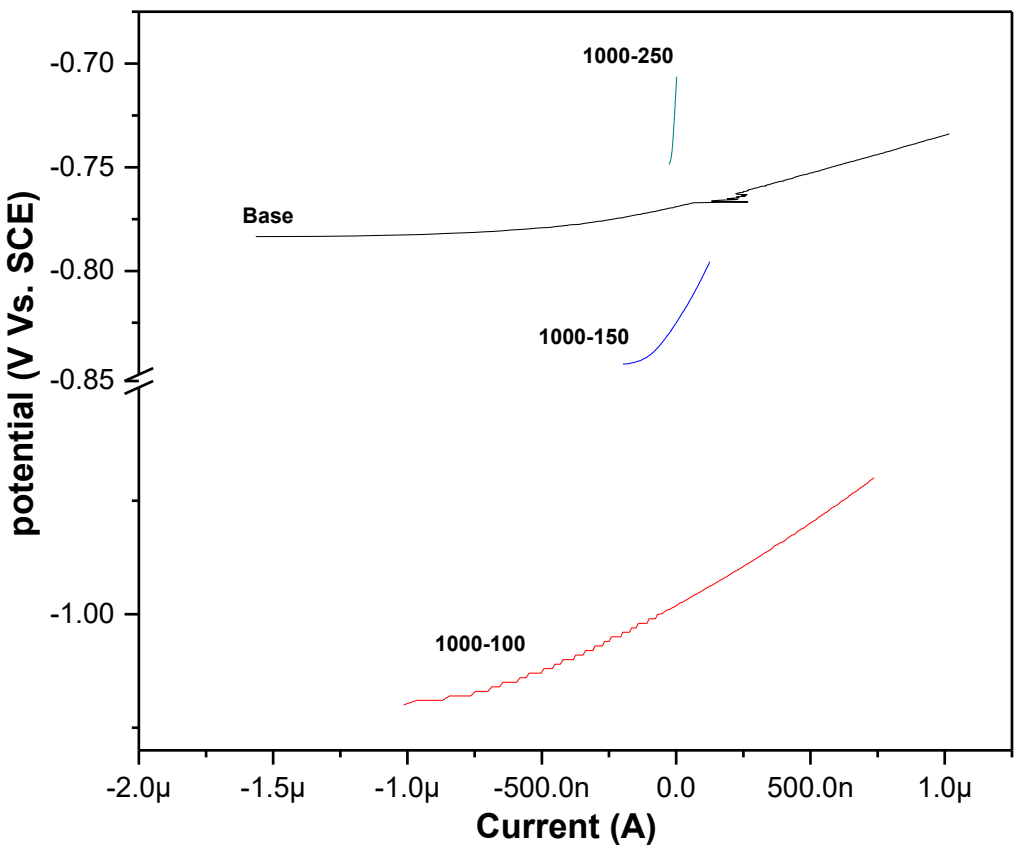

Figure 4- 8 Typical LPR plots for all samples after immersing all samples in 3.5% NaCl for 15 days

Table 4- 4 LPR data obtained after 15 days on immersion sample in 3.5% NaCl

Sample	R_p(kohms)	$I_{corr.}$ (µA)	C.R (mpy)
Base	35.87	2.724	1.168
1000-100	34.63	1.72	0.736
1000-150	220.1	0.185	0.0795
1000-250	2087	.00844	0.00362

4.1.5.4 SEM images for corroded samples processed at different traveling speeds

The morphology of intense corrosion attack for processed and base sample after 15 days of immersion in 3.5 % NaCl is depicted in Figure 4- 9. For the base sample, severe corrosion attack on the surface can be clearly noticed and indicated by corrosion products (C.Ps) adhered to the surface. Additionally, within the corrosion products, large pits are observed. Surprisingly, microcracks can also be detected beneath the corrosion products which may be ascribed to initiations of intergranular corrosion. Corrosion marks after processing samples using FSP demonstrated different appearance as seen in Figure 4- 9 (b), (c), and (d). Obviously, the size and the dense of pits became lower compared with that for the base sample. Moreover, the adsorption of corrosion products (C.Ps) is hardly detected on samples processed at 100 and 250 mm/min as shown in Figure 4- 9 (b and d) which attributed to grain refinement that enhanced passive film formed. Interestingly, the adhesion of corrosion products can be seen for 1000-150 sample Figure 4- 9 (d), nevertheless, with completely different characteristics compared base counterpart which interpreted by the reduction in outer film resistance for this sample (88.63 Ω) compared with (6.14 kΩ), (1.92 kΩ) and (2.16 kΩ) for the base, 1000-100 and 1000-250 samples respectively. Besides, a dense layer of corrosion products may act as a barrier to impede further corrosion attack.

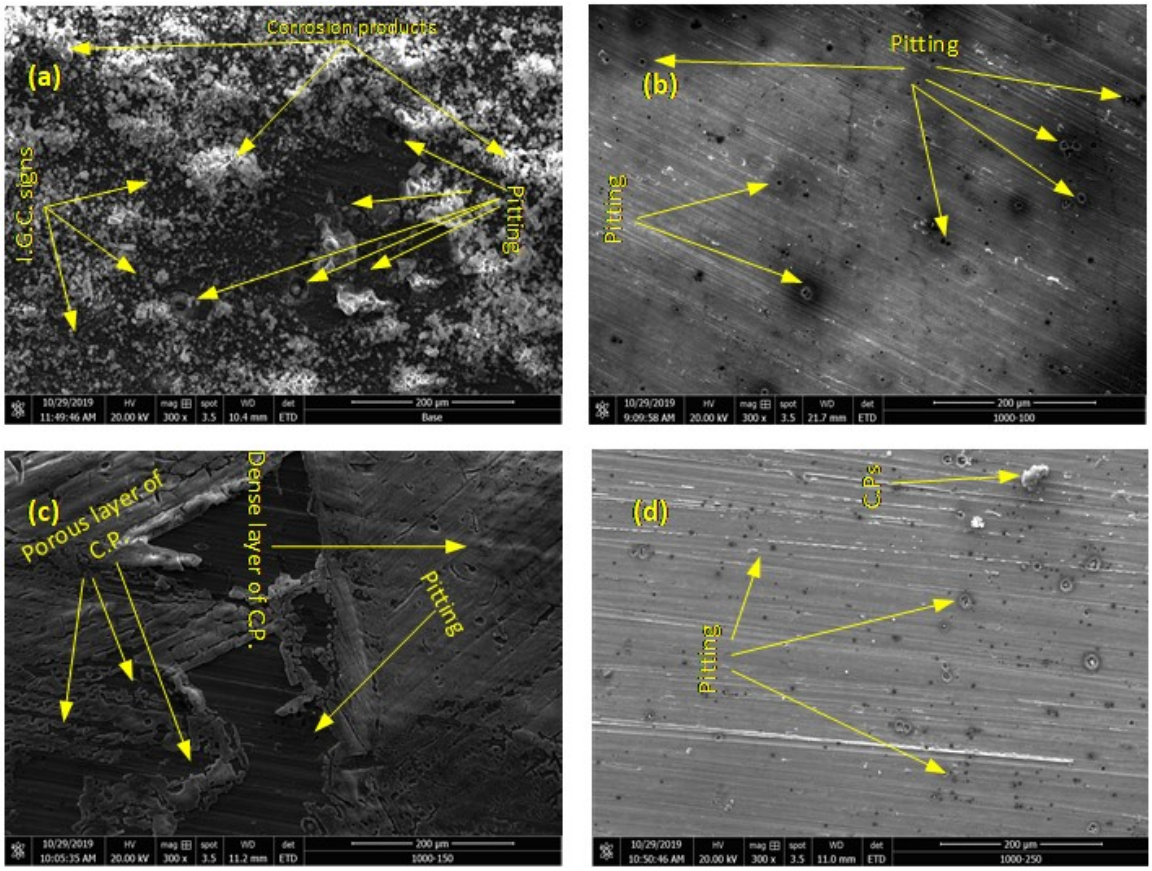

Figure 4- 9 SEM images for the corroded surface for (a) base sample, (b) 1000-100 sample, (c) 1000-150 sample, (d) 1000-250 sample after 21 days of immersion in 3.5 % NaCl

4.1.6 Discussion of corrosion results

Owing to its ability to form a spontaneous passive film in an atmospheric environment, aluminum and alloys therein demonstrate a good corrosion resistance. Nevertheless, their tendency to pitting corrosion rises in an aggressive environment of chloride media wherein the passive film is attacked by the ions. Formation of passive film is not instantaneously after immersion in aggressive media, it may need time. Subsequently, once the passive film is formed, chloride ions may attack the film and therefore cause pitting. Consequently, the rapid dissolution of a passive film results in corrosion current density increasing.

Therefore, it was suggested that passive film thickness and formality play a vital role in impeding ions attack for aluminum and its alloys. Thus, to study the corrosion behavior for aluminum and its alloys, it is worthwhile to investigate the key factor affecting the formation of the passive film which is grain size [128][129]. Due to its unique properties when compared with bulk material, namely diffusion rates, atomic coordination and reactivity, it is expected that reducing grain size will result in altering the electrochemical behavior [129]. It should be noted that the reduction in grain size results in a high density of grain boundary and thereby breaking intermetallic particles [130]. Also, surface with finer grain and more dense grain boundaries results in more readily passive film and thus improved the corrosion resistance [128]. Several studies have presented the corrosion behavior for aluminum-based alloys after grain refinement. For example, Jilani et al. [131] have studied the influence of varying the number of passes during equal channel angular pressing (ECAP) process on the passive film efficiency. The results have demonstrated that the ECAP process can improve the corrosion resistance of 1xxx aluminum alloys by reducing the grain size and enhancing the distribution of precipitate and thereby forming a continuous film. Likewise, the influence of severe plastic deformation of 2099 Al-Li on the formation of passive film was studied by Jinlong et al [132]. The results illustrated that the corrosion susceptibility reduces due to refinement in both grain and precipitates whereby grain refinement leads to electron work function decline and thus a thicker passive film.

Besides, various studies in the literature have shown that FSP resulted in rising the fraction of a high angle of grain boundaries [133][134]. The consequence of this shift to a higher fraction of a high angle of grain boundaries (HAGBs) on corrosion behavior was intensively investigated by Argade et. al., Dan et. al. and Rao [135][136] [137]. For example, Argade et al. have concluded that the corrosion enhancement after friction stir processing of AA 5083 was attributed grain refinement which resulted in improving the polarization resistance, passivation and pitting potential. Moreover, high angle grain boundaries provided by the process rises the corrosion resistance by accelerating the passivation re-passivation phenomenon [135]. Rao et al have demonstrated that the transformation from low angle grain boundaries to high angle counterparts after friction stir processing of Al–30Si alloy is a vital reason in the stability of the oxide film formed [136]. Dan et al. have studied the impact of grain refinement on corrosion behavior of pure aluminum and have disclosed a significant enhancement in corrosion and pitting resistance for the sample with finer grain and that was attributed to a denser passive film. Further, it was also suggested that the oxide film favored a higher grain boundary which protects the surface of the processed sample against chlorides attack and thereby enhancing the corrosion resistance [137]. Therefore, the obtained results may follow the same behavior whereby employing FSP significantly diminishing grain size and rising the fraction of high angle grain boundaries. Moreover, further reduction in grain size was detected upon rising tool traveling speed which resulted in superior corrosion resistance due to the more adhered and compacted passive film.

4.1.7 Wear behavior

Figure 4- 10 shows the coefficient of friction graph for the base and processed sample under a normal load of 20 N for 60 m sliding distance. It is clear from the plot that the base sample revealed a relatively higher friction coefficient as compared to processed samples. However, no major change was detected between various processed samples.

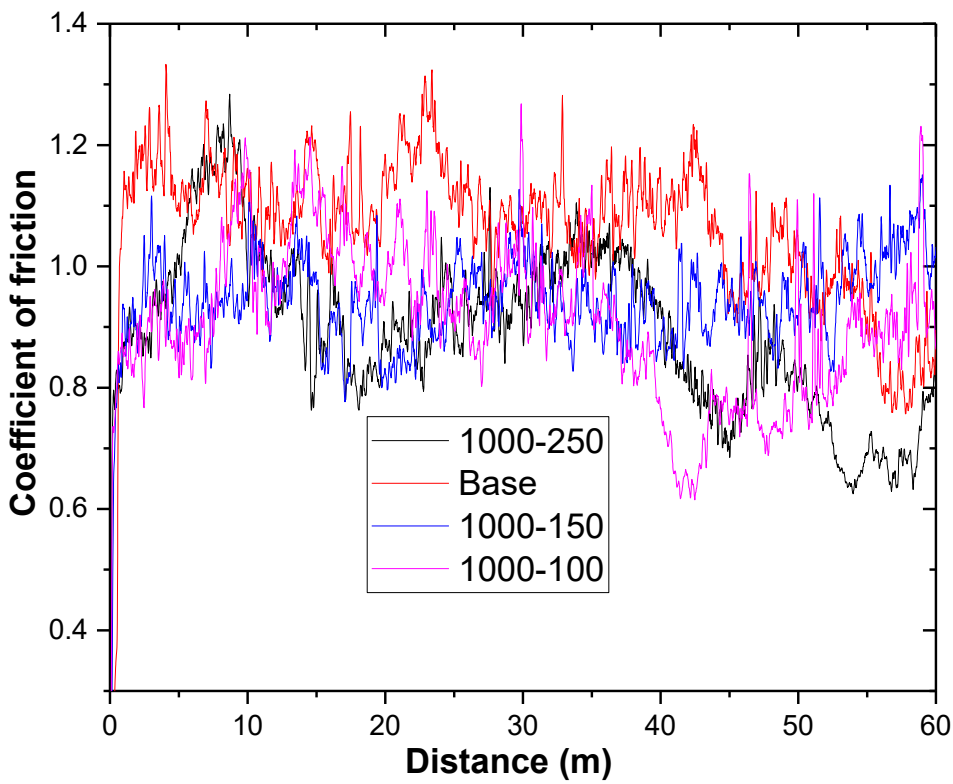

Figure 4- 10 COF for different samples processed at different traveling speeds

The effect of varying process conditions during FSP of 6061 AA on mass loss compared with that for the base sample is presented in Figure 4- 11. As obviously seen in the figure, most of the processed samples have demonstrated a considerable deterioration in wear

resistance. In addition, samples processed 150 and 250 mm/min have displayed a marginal rise in mass loss with approximately 8 and 3% respectively. Moreover, an appreciable decline in mass loss with about 11% is observed for the sample processed at the lowest traveling speed. It worth noting that the hardness is not the only important factor in evaluating wear properties [124].

It is should be emphasized that several studies have illustrated that the wear resistance of aluminum alloys has shown a significant decline after grain refinement despite hardness improvement [124][125][126]. They have ascribed the deterioration in wear resistance to grain refinement and loss in strain hardening capability.

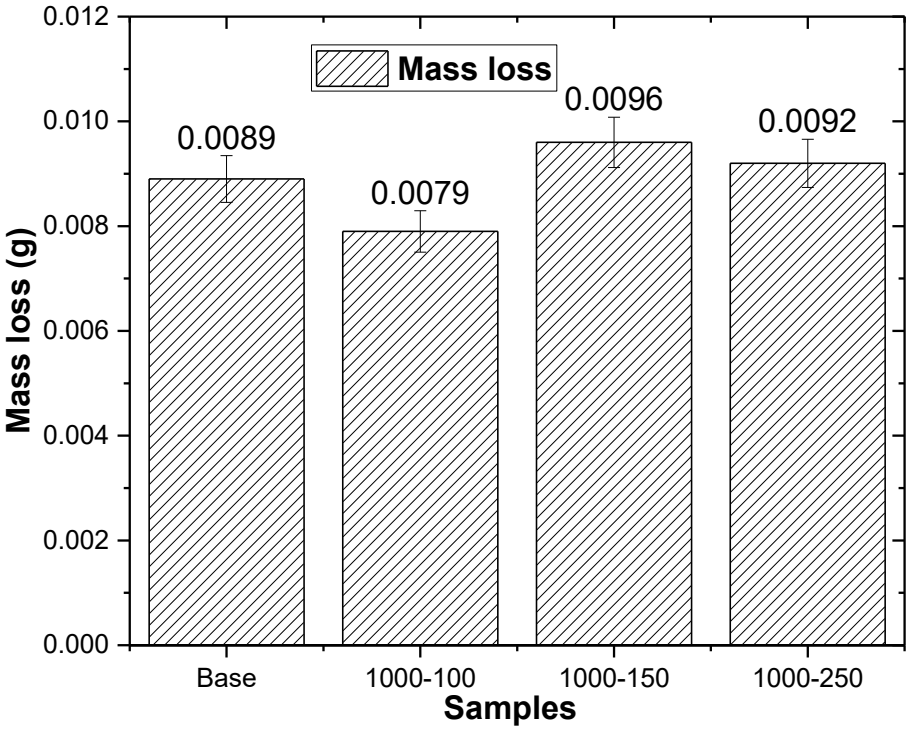

Figure 4- 11 Mass loss for different samples processed at different traveling speeds

The representative high magnification scanning electron images are depicted in Figure 4-12 Wear mechanism to demonstrate the wear mechanism for the base and processed samples. In fact, the wear mechanism does not demonstrate significant differences for processed samples when compared with the base metal. As obviously seen in Figure 4- 12 Wear mechanism a, b, c and d the predominant wear mechanisms are delamination, adhesive and abrasive wear which occurred simultaneously on all surfaces. Besides, the damage on the surface of the base sample due to delamination is more pronounced. Moreover, the adhesive wear accompanied by delamination caused the removal of small particles (debris particles) which act as 3 body abrasion and resulted in abrasive wear. Interestingly, the sample with a finer grain structure (1000-250) demonstrates a high density of small wear debris compared to all other samples and this possibly due to the high density of grain boundaries [127].

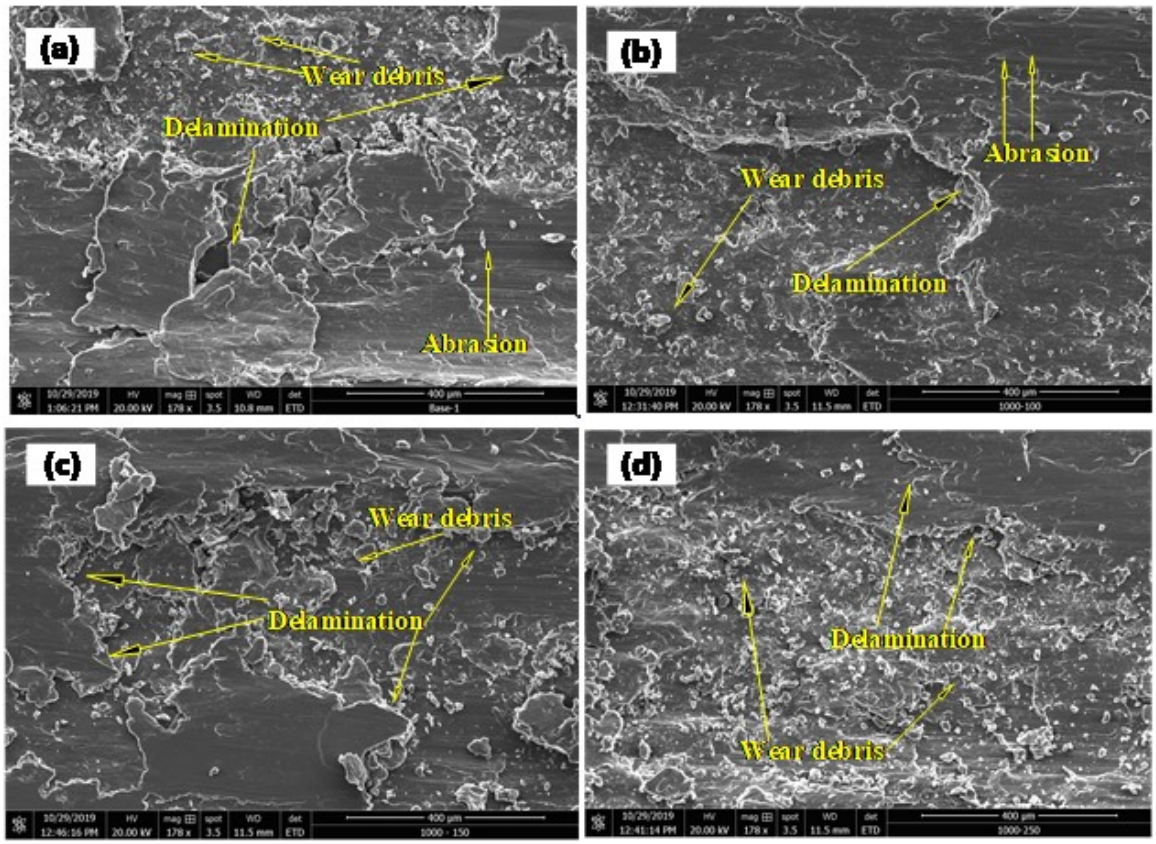

Figure 4- 12 Wear mechanism for (a) base, (b) 1000-100, (c) 1000-150, (d) 1000-250 samples

4.2 Effect of changing tool rotational speed

4.2.1 Generated torque

The influence of increasing rotational from 400 to 1200 rpm on generated torque during FSP is presented in Figure 4- 13. Generated torque from the samples processed at different rotational speeds. It should be mentioned that the traveling speed was maintained at 250 mm/min for all the tests. It is obvious from the graph that rising rotational speed from 400 rpm to 800 rpm resulted in decreasing the generated torque from about 100 to 80 N.m and further increment in tool rotation speed to 1200 rpm caused the decline of spindle torque to around

70 N.m. The reduction in generated torque with rising rotation speed may be ascribed to the heat input increment and thereby diminishing in flow stress [87]. Moreover, low fluctuation in recorded torque at 1200 rpm can be noticed from the plot as compared to other conditions. Lower values of spindle torque are observed at the first stage of the graph which is ascribed to transient traveling speed before steady-state condition.

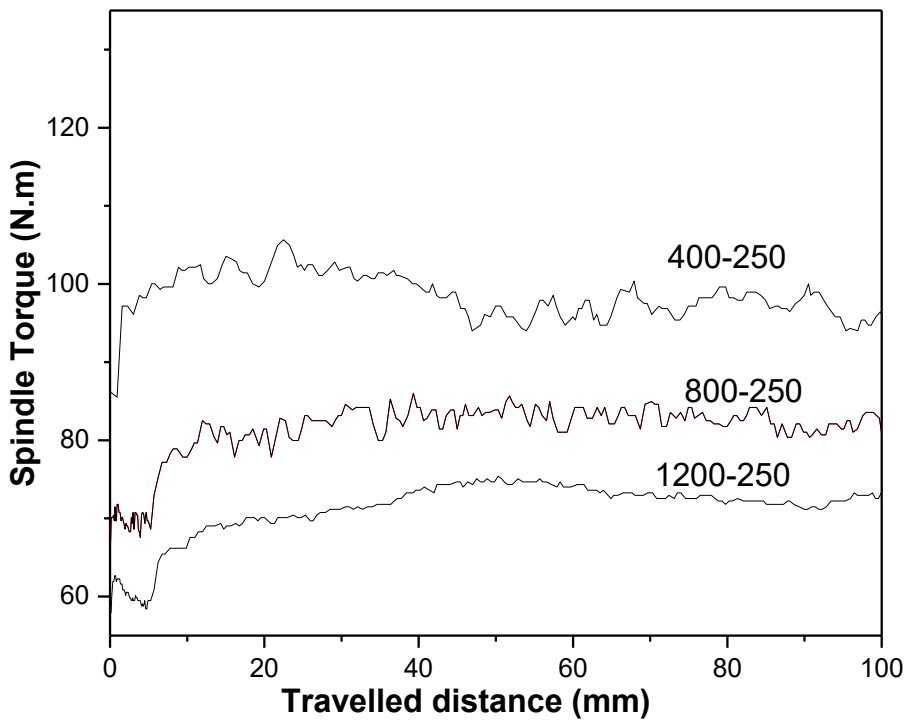

Figure 4- 13. Generated torque from the samples processed at different rotational speeds

4.2.2 Microstructural analysis

The impact of rising rotation speed from 400 to 1200 rpm at an unchanged tool traveling speed of 250 mm/min during friction stir processing of 6061 AA on grain structure compared to the base metal is illustrated in the optical micrograph in Figure 4- 14. It is evident from Figure 4- 14 that employing friction stir processing substantially change the

grain structure. Also, a considerable refinement can be observed for all processed samples. Further, as shown in **Error! Reference source not found.**, a significant reduction in the grains size from 94 µm for the base sample to 15.48 µm for the sample processed at 400 rpm. Moreover, with increasing tool rotational speed from 800 to 1200 rpm, the grain size demonstrated a slight increment from approximately 17.36 to 19.12 µm, while the heat input increased remarkably from 1608 to 2111 J/mm. Similar observation was extensively reported in the literature [88], [138]. It was suggested that rising tool rotation speed caused higher heat input and elevated temperature exposure and thereby increasing the grain size at the surface of these workpieces [88]. It is worthwhile to mention that the grain refinement of the processed zone during friction stir processing was ascribed to the combination of temperature increase and severe plastic deformation resulting from the rubbing action of the tool with the specimen[139]. Various mechanisms were proposed to be responsible for grain refinement during friction stir processing, namely discontinuous dynamic recrystallization (DDRX), Dynamic recovery (DRV), and geometric dynamic recrystallization (GDRX) [90]–[93].

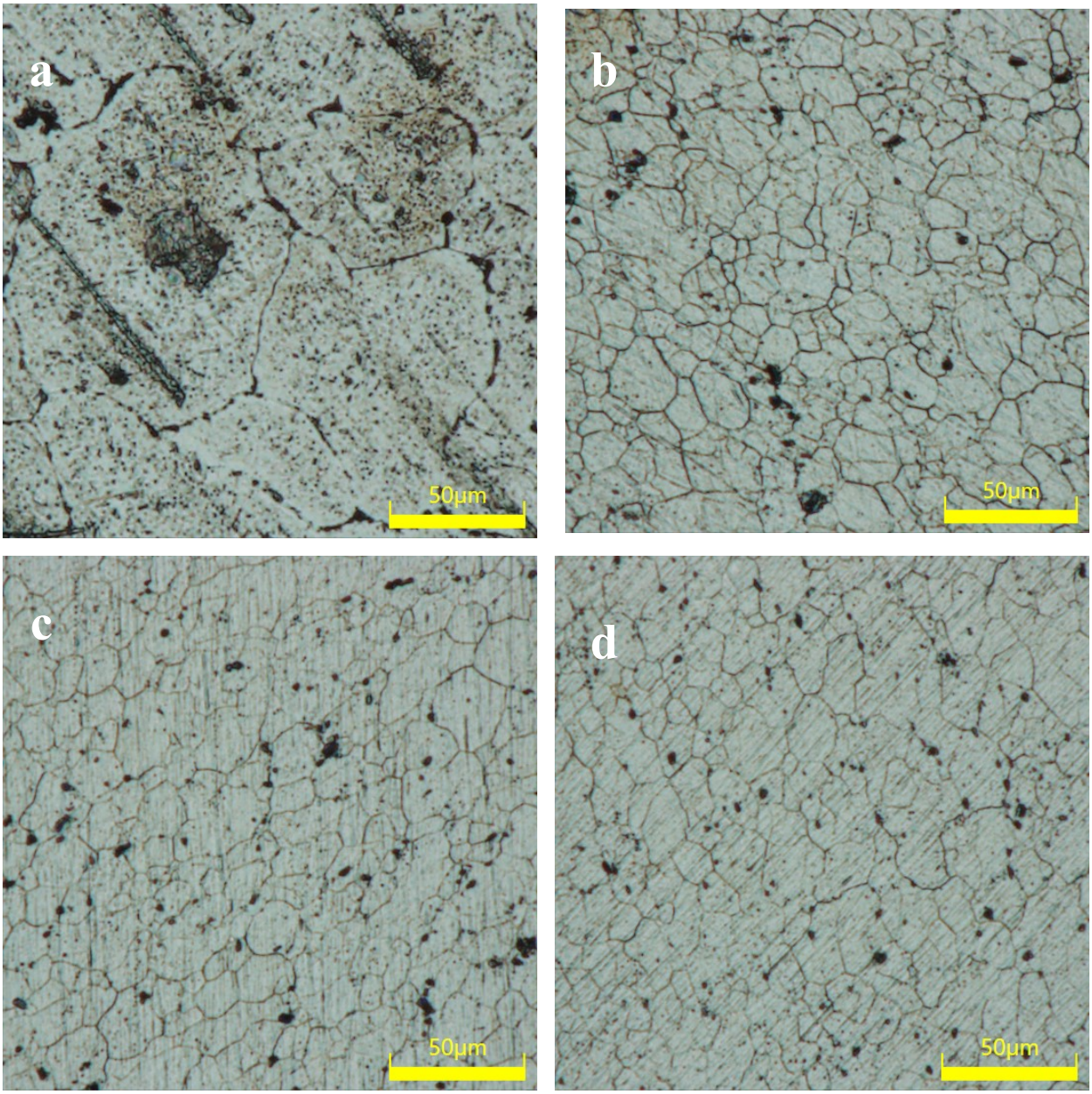

Figure 4- 14 . Optical micrograph of the grain structure for the (a) base, (b) 400-250, (c) 800-250 and (d) 1200-250 samples

Table 4- 5 Grain size for the base and processed samples

Samples	Generated torque (N.m)	Heat input (J/mm)	Grain size
Base	-		94 µm
400-250	100	1005.31	15.48 µm
800-250	80	1608.5	17.36 µm
1200-250	70	2111.15	19.12 µm

4.2.3 XRD

Figure 4- 15 (a) shows XRD patterns for the base sample as well as processed samples. It is obvious from the graph that the four aluminum peaks are found without any extra peaks which suggest that no intermetallic phases were formed due to the process. In addition, relatively narrow peaks were found for the base sample which indicates a higher grain size and a lower lattice distortion [140]. Moreover, a phase shift is clearly observed in Figure 4- 15 (b) for all processed samples toward a higher diffraction angle. A similar observation was reported before after friction stir processing of magnesium and copper and was attributed to the existence of compressive strength which resulted from the reduction in lattice parameter [97][98].

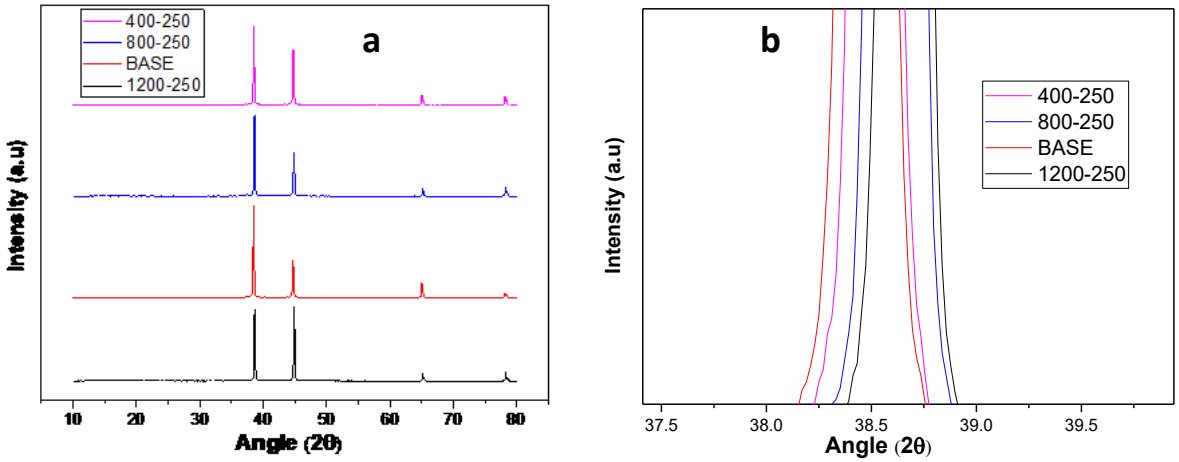

Figure 4- 15 . XRD (a) patterns of the base material and material processed at various rotational speeds, (b) first peak for all samples to demonstrate the phase shift

4.2.4 Evaluation of mechanical properties

The influence of rising tool rotation speed from 400 to 1200 rpm during friction stir processing of 6061 AA on processed surface microhardness, modulus of elasticity and indenter penetration depth is depicted in Figure 4- 16. It is evident from the figure that the average microhardness of the base sample is 49.7 HV and after processing samples using FSP, the microhardness significantly improved to 71.4, 69.1 and 68.3 HV for the samples processed at 400, 800 and 1200 rpm respectively. The substantial increment in microhardness after samples processing may be attributed to grain refinement which follows the Hall-Petch relationship [141]. Similarly, a marginal enhancement in elastic modulus was also attained after samples processing with 7%, 8% and 6% for 400-250,800-250 and 1200-250 samples respectively. Such an increment modulus of elasticity was reported before and may be ascribed to dynamic recrystallization [55].

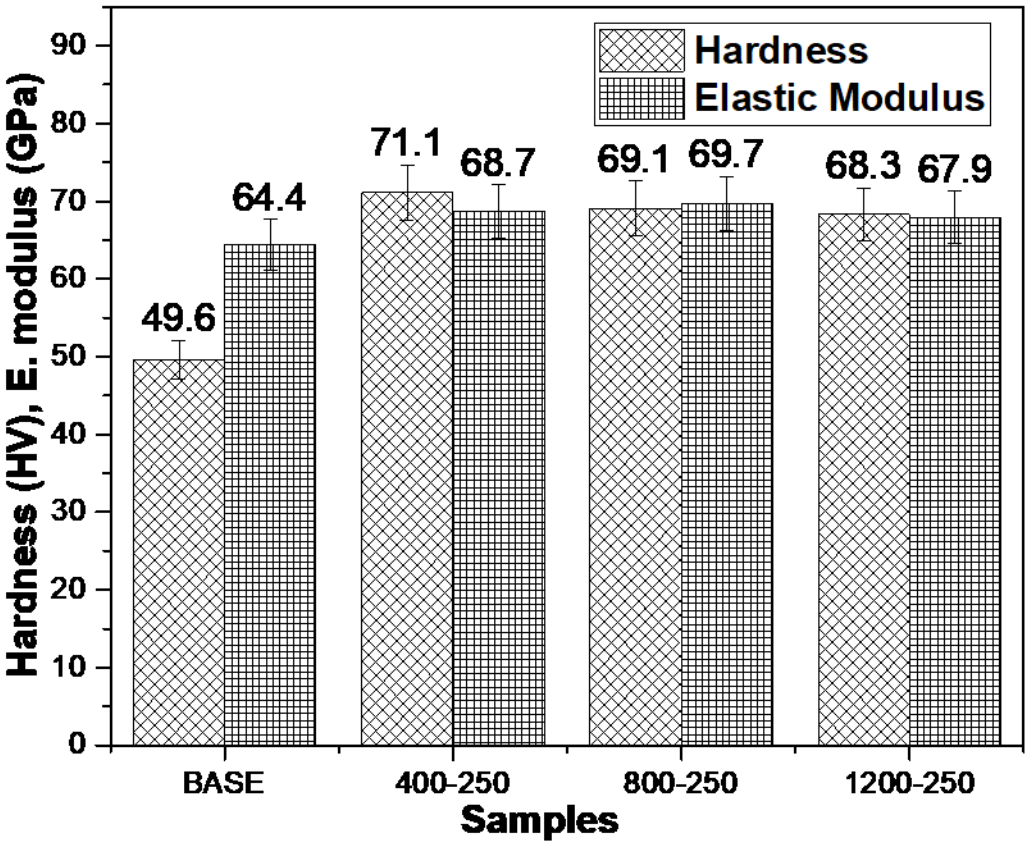

Figure 4- 16 Hardness, maximum penetration depth and modulus of elasticity for the base and processed samples

4.2.5 Evaluation of corrosion behavior

4.2.5.1 Electrochemical impedance spectroscopy (EIS)

In order to investigate surface metal oxides, corrosion mechanisms, kinetics, and surface treatment. Electrochemical impedance spectroscopy (EIS) is extensively deployed [100], [101]. Therefore, EIS measurements were done to explore the impact of changing tool rotational speed from 400 to 1200 rpm during friction stir processing of 6061 AA on corrosion kinetics as compared to the as-received specimen after immersing all samples in 3.5% NaCl electrolyte for 15 days.

Figure 4- 17 presents the Nyquist plot for the base sample as well as processed samples. As observed from the plot, all processed samples demonstrate a larger uncomplete arc at a higher frequency and smaller at a lower frequency compared to the base sample, which illustrates relatively smaller uncomplete semi-circle at a higher frequency and larger uncomplete arc at a lower frequency. It was suggested that the uncomplete capacitive arc for processed samples refers to charge transfer resistance at the border between passive film formed, sodium chloride electrolyte and the metal [102]. Consequently, the charge transfer resistance occurred when the passive film exists at the interface between the electrolyte and metal surface. It is worthy to mention that the existence of the second uncomplete arc may be attributed to diffusion-controlled processes [103]. It can be clearly seen in Figure 4- 17 that the radius of capacitive arc significantly increases with rotational speed rises and all processed samples displayed a larger radius as compared to the base metal. Interestingly, the radius of the capacitive arc for the base sample was not able to be captured without enlarging. A vast variation in capacitive arc radius between the base and processed samples demonstrated that the corrosion resistance was altered by friction stir processing. In addition, a raise in arc radius after processing is ascribed to improvement in surface protectiveness which resulted from stability and compactness increment of the passive film [106], [107].

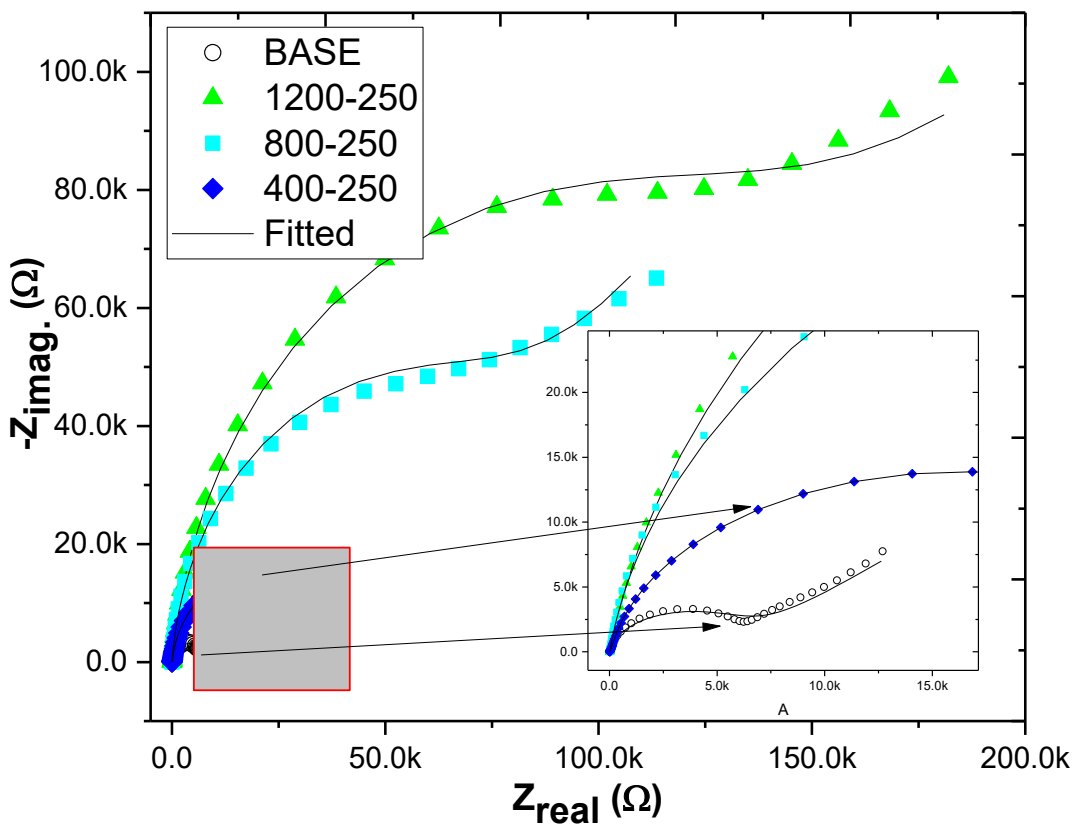

Figure 4- 17 Nyquist graph for both base and processed samples after immersing in 3.5 % NaCl for 15 days

Figure 4- 18 illustrates an impedance-frequency graph after immersing all samples in 3.5% NaCl electrolyte for 15 days. It is noticed from the graph that the total impedance at the low frequency of 0.01 Hz for all processed samples is greatly higher than that of the base sample which revealed the surface protectiveness provided by friction stir processing. Furthermore, a rise in total impedance was noticed with increasing rotation speed where 1200-250 sample reveals the highest corrosion resistance compared to 800-250 sample which showed lower resistance to corrosion. Moreover, the sample processed at the lowest rotational speed demonstrated the lowest corrosion resistance

among all processed samples; it is however showed markedly higher corrosion resistance when compared with the base sample.

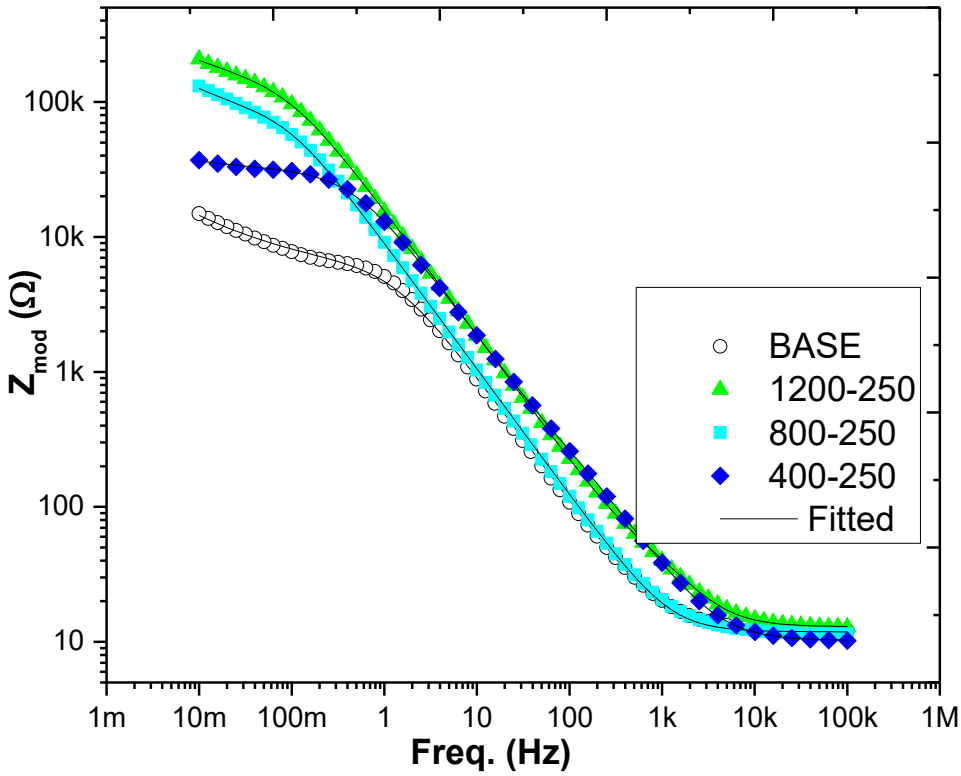

Figure 4- 18 Impedance plot for the base as well as processed samples after immersing in 3.5 % NaCl for 15 days

Figure 4- 19 shows a typical plot for phase angle-frequency for the base sample as well as processed samples after 15 days of immersion in 3.5% NaCl. As clearly seen in the figure, the base sample exhibits a phase angle maxima of -78.5° at a frequency of 25 Hz. Further, observing maxima at such a high frequency revealed a weakening in the stability of the barrier at high frequency [108].

In contrast, all 400-250, 800-250 and 1200-250 samples illustrated a shift in phase angle maxima toward 76.2°, 84° and 81.9° at a frequency of 12.4, 6.3 and 6.3 Hz respectively. It is evident from the figure that the base sample shows the narrowest phase peak; however, after deploying FSP further widening was captured with rising the rotational speed which could account for two times constant interaction [109]. In addition, peak widening after surface processing may ascribe to improvement in a passive layer over a wide range of frequencies and thereby enhancing corrosion resistance [108][110]. It is worthwhile to mention that phase angle maxima shifting to a higher frequency demonstrating that the corrosion would have launched on the sample for a long exposure time [111]. Thus, a severe corrosion attack is expected on the surface of unprocessed sample and consequently a higher corrosion rate when compared with other processed samples.

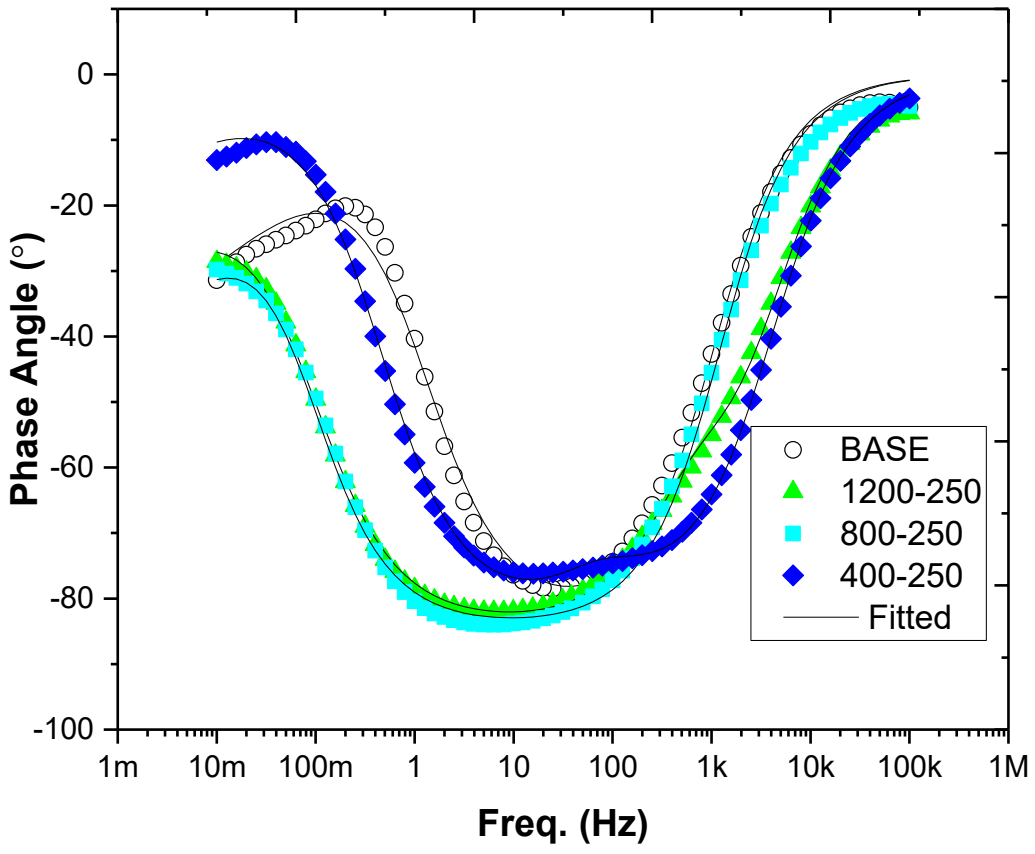

Figure 4- 19 Phase angle graph for the base and processed samples after immersing in 3.5 % NaCl for 15 days

With an objective of numerical estimation for the characteristics of the barrier for the base sample as well as processed samples, all curves were fitted to equivalent circuits. Consequently, two corresponding circuits were utilized to simulate the corrosion behavior of base and processed surfaces. Figure 4- 20 illustrates the corresponding circuit that simulates the corrosion behavior on the surface of the base sample which consists of polarization resistance (R_p) connected in series with Warburg resistance (W) and both are connected in parallel to constant phase element of double-layer capacitance, and the

previous configuration is serially connected to the solution resistance (Rs). On the other hand, to simulate the behavior of corrosion on samples processed at 400, 800 and 1200 rpm a circuit involve charge transfer resistance (R_{ct}) serially connected to Warburg resistance (W) and both are parallelly linked to constant phase element of double-layer capacitance and all are serially connected to polarization resistance which connected in parallel to constant phase element and the whole previous circuit is connected in series to the solution resistance (Rs). It should be emphasized that pure capacitance was replaced by constant phase elements due to non-ideal capacitive behavior that revealed by the deviation from 90° in the phase angle. Thus, to calculate the double layer capacitance, eq. 4.2 was used.

Table 4- 6 presents the electrochemical parameters derived from two electric circuits. It evident from Table 4- 6 that double-layer capacitance (C_{dl}) of constant phase element demonstrates a significant drop for all processed samples as compared to the base metal and the order of reduction for the samples was the base, 800-250, 1200-250 and 400-250. It is worthwhile to know that the diminishing in double-layer capacitance after surface processing suggesting an improvement in the corrosion resistance which may be ascribed to the decline in the activeness of the surface as a result of passive film formation [113][114]. Accordingly, a reverse relationship between the double-layer capacitance (C_{dl}) and the thickness of the protective film was disclosed in the Helmholtz model (eq. 4.3). [142][143][144].

As clearly seen in Table 4- 6, all processed samples have shown a lower value of double-layer capacitance (C_{dl}) and therefore a higher protective film thickness when compared with the base sample. It is also obvious from Table 4- 6 that charge transfer resistance (R_{ct}) for the base sample is 6.4 kΩ and after deploying FSP the R_{ct} revealed a noticeable boost to 29.4 kΩ for the sample processed at the lower speed. Additionally, further increment in tool rotational speed from 800 to 1200 rpm resulted in remarkable improvement in R_{ct} from 80.7 to 144 kΩ. It should be emphasized that the raise in charge transfer resistance after samples processing may be interpreted by the formation of the passive film at the border between the electrolyte and surface of the metal. Therefore, the existence of such a passive film protects the metal surface from ions attack and thereby impeding the addition of charge or mass transfer [118]. Commonly, Warburg resistance (W) is added to stimulate the influence of diffusion and it is signaled by a straight line in the Nyquist plot near to 45° to the real axis of impedance. It is clear from the table that most of the processed samples illustrated a lower Warburg resistance value when compared with the base sample. It should be mentioned that a lower value of this resistance implies a diminishing in the flow of chloride ions across the passive film and thereby enhancing corrosion resistance [121][111].

Table 4- 6 Electrochemical parameters derived from Nyquist plot

Samples	Rs (Ω)	Y_{01} (S*s^a) 10^{-6}	a1	Rp (kΩ)	Y_{02} (S*s^a) 10^{-6}	a2	R_{ct} (kΩ)	Cdl (μF)	W S*s^(1/2)*10^{-6}	X ^{2}*10^{-4}
Base	12.38	23.5	0.92	6.14				0.340	413	0.29
400-250	10.2	11	0.90	1.89	1.61	0.97	29.4	0.138	527	4.64
800-250	11.54	12.94	0.955	0.044	5.78	0.94	80.7	0.159	57.6	6.20
1200-250	12.92	7.39	0.92	0.118	4.04	0.94	144	0.165	41.5	5.50

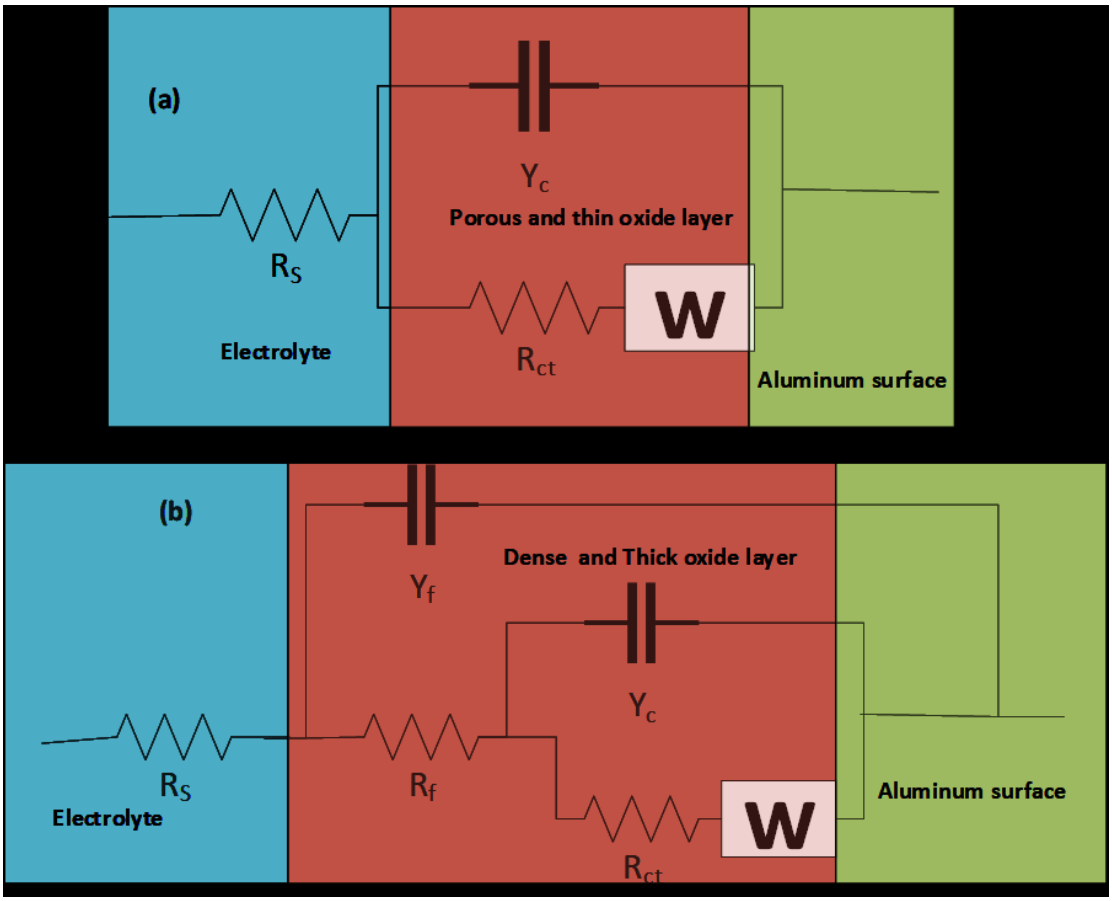

Figure 4- 20 Equivalent circuits utilized to fit: (a) the base sample, (b) 400-250, 800-250 and 1200-250 samples

4.2.5.2 Potentiodynamic polarization (PDP)

Figure 4- 21 presents typical potentiodynamic polarization curves of the base as well as processed samples after immersing for 15 days in 3.5% NaCl electrolyte. Table 4- 7 reveals different parameters obtained from the fitting of potentiodynamic curves for all samples, namely corrosion potential ($E_{corr.}$), corrosion current density (I_{corr}) and both cathodic and anodic Tafel slopes (β_c&β_a). Interestingly, corrosion potential exhibits a significant shift to the positive direction after rising the tool rotation speed from 800 to 1200 rpm, however, the base sample shows more positive potential. Despite the lower corrosion potential (E_{corr}) of the unprocessed sample when compared with the processed counterpart, the samples processed at 400 and 1200 rpm showed a lower pitting potential as depicted in Figure 4-21 which reveals an enhancement in pitting resistance for these processed samples.

The inspection of Table 4- 7 demonstrates that the corrosion current density of the base sample is 3.22 µA and after employing friction stir processing the corrosion current density sharply drops. Additionally, with increase tool rotation speed from 400 to 800 rpm, the corrosion current density drastically reduced from 0.914 to 0.468 µA. Interestingly, the sample processed at the highest tool rotation speed of 1200 rpm revealed the maximum resistance to corrosion with corrosion current density of 0.057 µA. Hence, a considerable reduction in (I_{corr}) and therefore corrosion rate revealed that the friction stir processing has a great potential in reducing the corrosion susceptibility of 6061 AA.

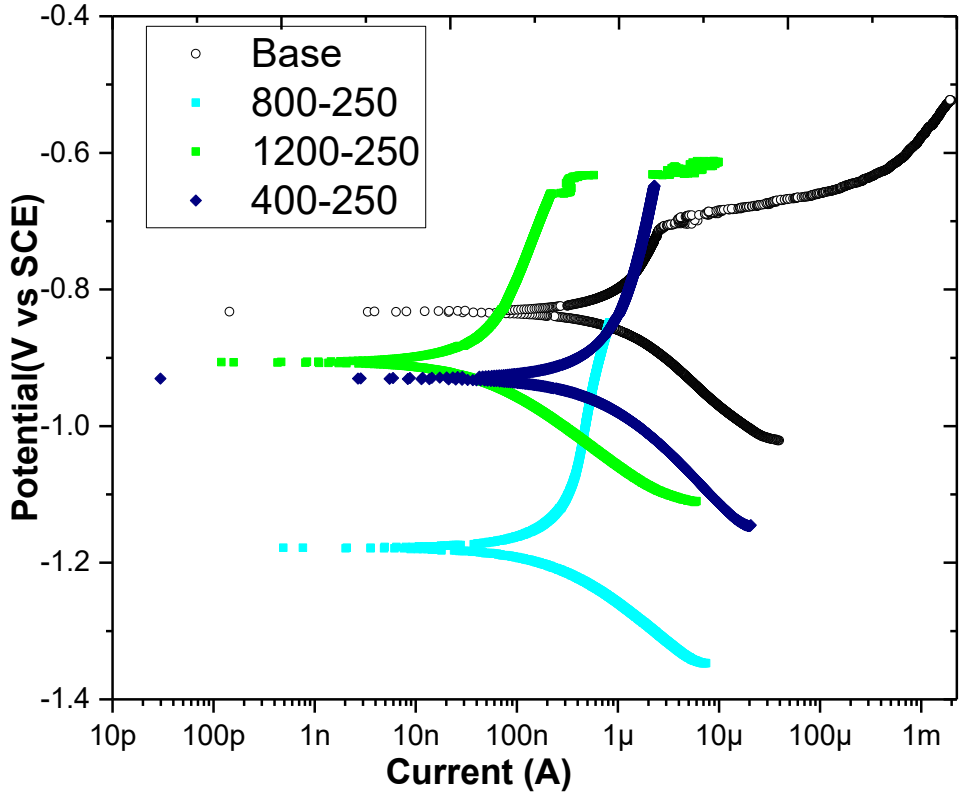

Figure 4- 21 Potentiodynamic Polarization curves after 15 days of immersion in 3.5 % NaCl for the base and processed samples

Table 4- 7 Corrosion parameters derived from Tafel curves fitting

Samples	b_a	b_c	I_{corr} (μA)	E_{corr} (V)	corrosion rate (mpy)
Base	1.856	2.56E-01	3.22	-0.832	1.469
400-250	6.62E-01	1.74E-01	0.914	-0.93	3.92E-01
800-250	1.830	1.52E-01	0.468	-1.18	2.13E-01
1200-250	4.43E-01	1.25E-01	5.68E-02	-0.906	2.59E-02

4.2.5.3 Linear polarization resistance (LPR)

Figure 4- 22 illustrates linear polarization curves for all samples after immersing in 3.5% NaCl for 15 days. Accordingly, polarization resistance was observed as the slope of corrosion potential vs current. Consequently, the Stern-Geary equation was used to obtain the corrosion current density (I_{corr}) knowing the polarization resistance (R_p) according to eq. 4.4 and subsequently eq. 4.5 was used to calculate the corrosion rate.

Inspecting Table 4- 8 reveals that the corrosion current density of all processed samples is lower than that of the base metal and the sample processed at the highest rotational speed displayed the lowest corrosion current density and therefore the lowest corrosion rate.

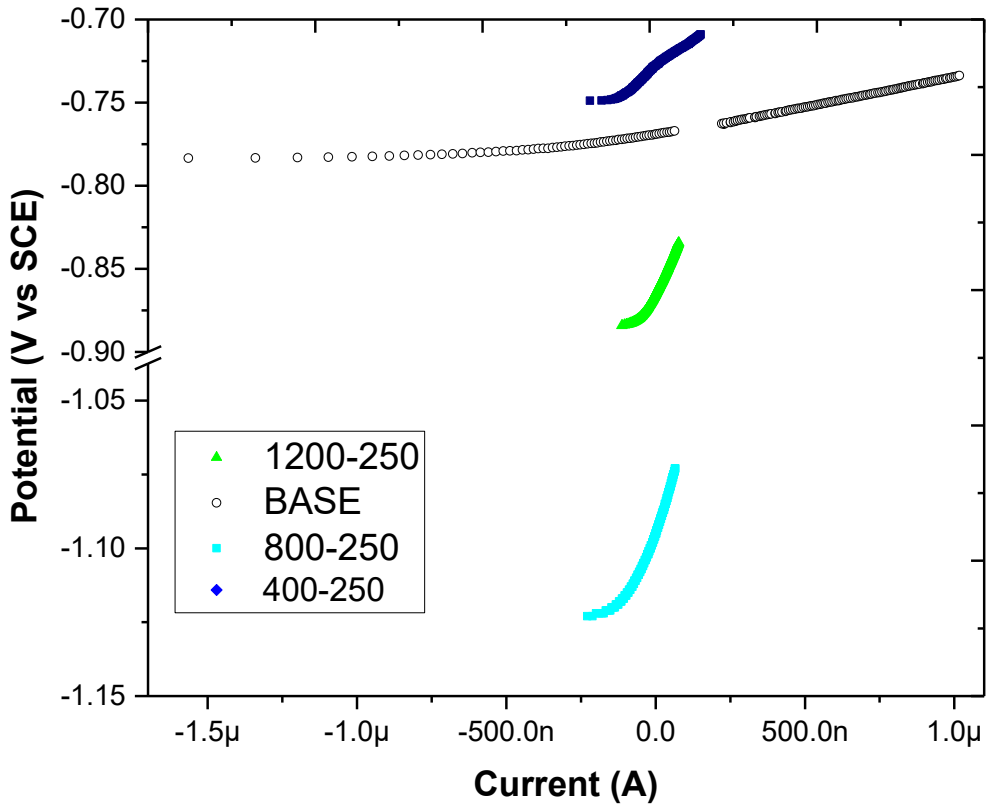

Figure 4- 22 Linear polarization curved for all samples after immersing in 3.5% NaCl for 15 days

Table 4- 8 Polarization resistances values obtained from LPR curves

Samples	R_p (kohms)	$I_{corr.}$ (μA)	C.R. (mpy)
Base	35.87	2.724	1.168
400-250	119	0.503	0.2157
800-250	322.8	0.1889	0.0389
1200-250	379.4	0.1115	0.0291

4.2.5.4 SEM images for corroded samples processed at different rotational speeds

To study the morphology of the corroded surfaces and to compare the influence of processing samples using friction stir processing, various scanning electron images were taken from the area that was exposed to 3.5 % NaCl for 15 days and after potentiodynamic polarization test. As depicted in Figure 4- 23 (a), deeper corrosion pits were noticed for the base sample especially around the corrosion products. Additionally, as compared to processed samples, the base metal demonstrates a severe corrosion attack which confirmed the results obtained from the phase angle-frequency plot b, c and d. Further, the higher pit potential for all processed samples compared to the base sample is another way to explain the higher severity of corrosion attack on the base sample.

4.2.5.5 Discussion of corrosion results

To sum up, besides scanning electron images, all electrochemical tests show a strong agreement in the trend of corrosion resistance where the base sample revealed the highest corrosion rate and a further reduction in corrosion susceptibility was observed upon rising

the tool rotational speed. A similar observation has been disclosed by Surekha et al. and Navaser et al. upon friction stir processing of 2219 AA and 7075 AA respectively [145] [146]. For both cases, the enhancement in corrosion resistance with increasing tool rotation speed was ascribed to precipitation dissolution[ref]. Likewise, Zhou et al. [147] have studied the influence of increasing rotation speed on the microstructure of Al-Mg-Si alloy and have concluded that the rise in tool rotation speed resulted in the dissolution of Mg_2Si precipitate due to the increase in heat input. Indeed, the corrosion behavior of this precipitate relative to the aluminum matrix was extensively studied in the literature [148][149][150]. There is a strong agreement between all authors that Mg_2Si has cathodic behavior and therefore it is expected that its dissolution will have a positive impact on corrosion resistance. It should be emphasized that the corrosion behavior after grain refinement is not fully understood yet. Nevertheless, according to electrochemical results in Table 4- 6, there is mismatching between the increase in passive film thickness and the reduction in corrosion susceptibility.

It is strongly believed that a combination of both grain refinement and precipitation dissolution are the main reasons for superior corrosion resistance obtained after processing the samples surfaces.

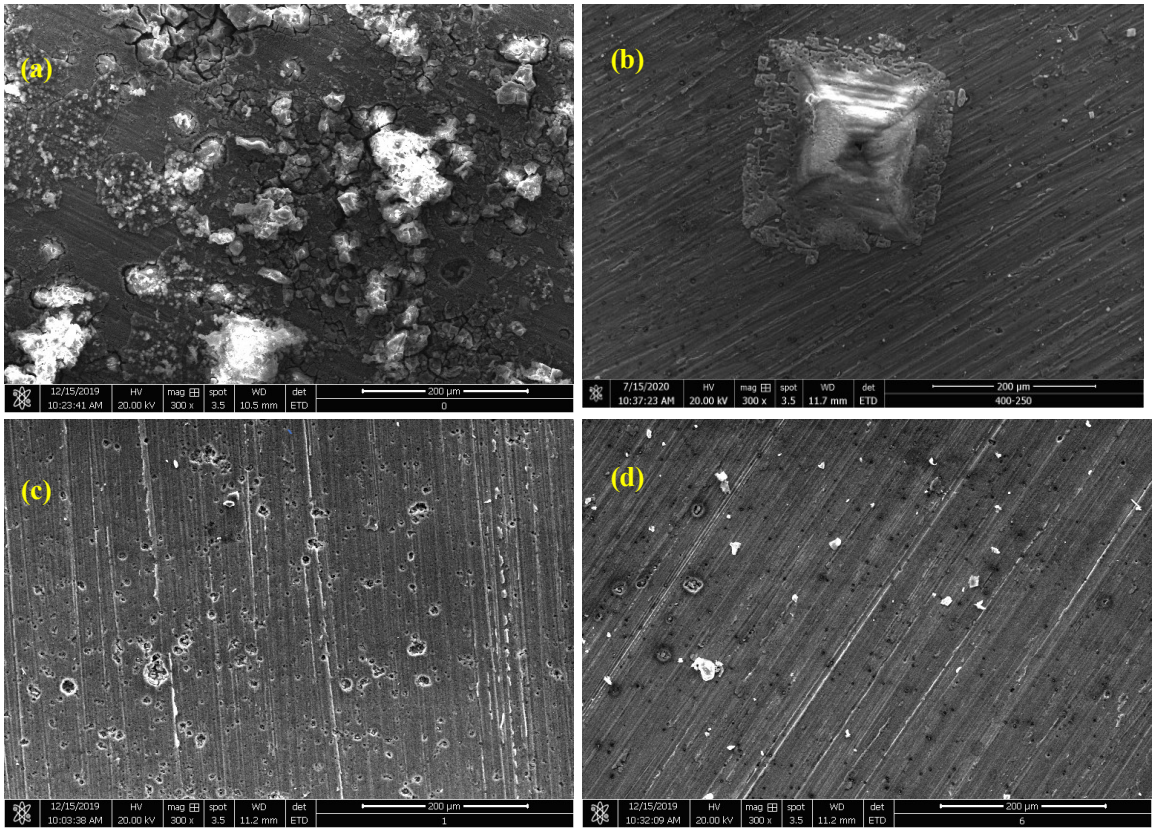

Figure 4- 23 Scanning electron images of (a) base, (b) 800-250, (c) 1200-250 samples after 15 days of immersion in 3.5% NaCl.

CHAPTER 5

FRICTION STIR PROCESSING OF 2099 AA

In this chapter, the influence of FSP on microstructure and corrosion resistance of Al-Cu-Li alloy (2099-T83) was studied in detail.

Figure 5- 1 shows an optical image of etched as an extruded sample which was taken in the extrusion direction. As clearly seen in the figure, an unprocessed sample illustrates unrecrystallized elongated grains parallel to the extrusion line, despite the heat-treatment that the sample experienced. Besides, recrystallized grains can be seen in low proportion which their formation is ascribed to heat-treatment.

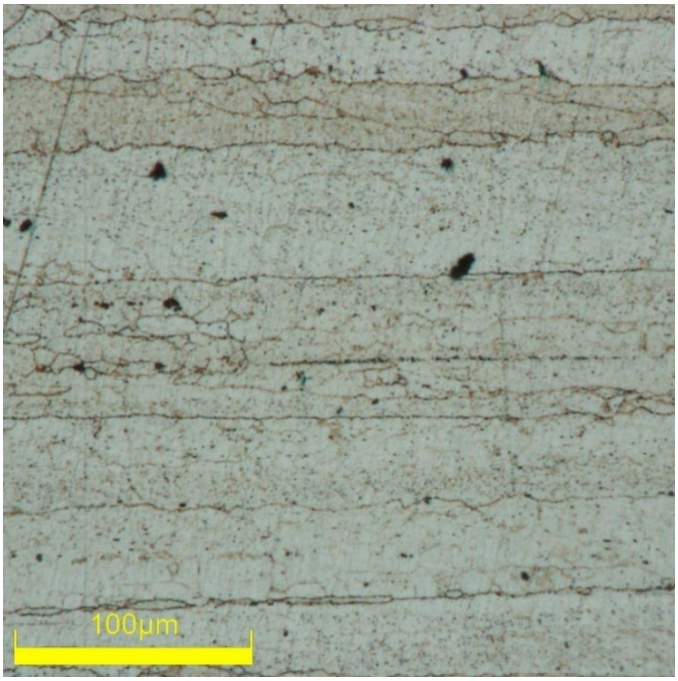

Figure 5- 1 Optical image of an as extruded 2099 T83 base sample

5.1 Effect of changing traveling speed

5.1.1 Generated Torque

Figure 5- 2 Influence of changing tool traveling speed on spindle torque shows the effect of changing tool traveling speed from 50 to 200 mm/min while keeping tool rotation speed constant at 1000 rpm on resultant spindle torque. As clearly seen, all samples showed a jump at the beginning of the process which is attributed to the cold run. In addition, spindle toque of around 26 N.m resulted from moving of tool at a rate of 100 mm/min. Besides, rising tool traveling speed from 150 to 200 mm/min caused a remarkable increment in spindle torque from approximately 29 N.m to 33 N.m. High fluctuations in spindle torque is observed at the lowest traveling speed which revealed the crucial role played by traveling speed in determining heat input.

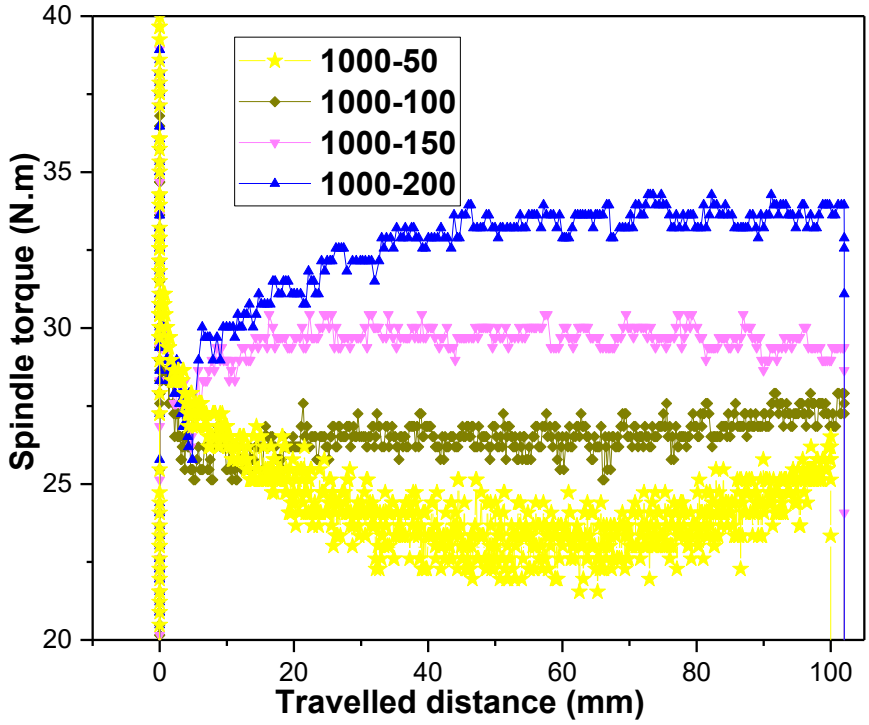

Figure 5- 2 Influence of changing tool traveling speed on spindle torque

5.1.2 Microstructure analysis

Figure 5- 3 (a), (b), (c) and (d) show the microstructure of processed zone after deploying FSP at four different traveling speeds i.e. 50, 100, 150 and 200 mm/min and fixed rotating speed of 1000 rpm. As clearly seen in the figure, FSP remarkably refines and homogenized the microstructure of the processed zone. Additionally, with traveling speed increment, the grain size demonstrates a noticeable reduction. Further, heat input, generated torque and grain size for different samples are listed in Table 5- 1. It is evident from the table that with at constant rotational speed of 1000 rpm, increasing the tool traveling speed caused

an appreciable increase in generated torque, while the both heat input and grain size substantially reduced. It should be emphasized that the more grain refinement after increasing tool traveling speed was reported before. Such a refinement was ascribed to reduction in heat input which play a crucial role in determining grain size according to the principles of recrystallization [94].

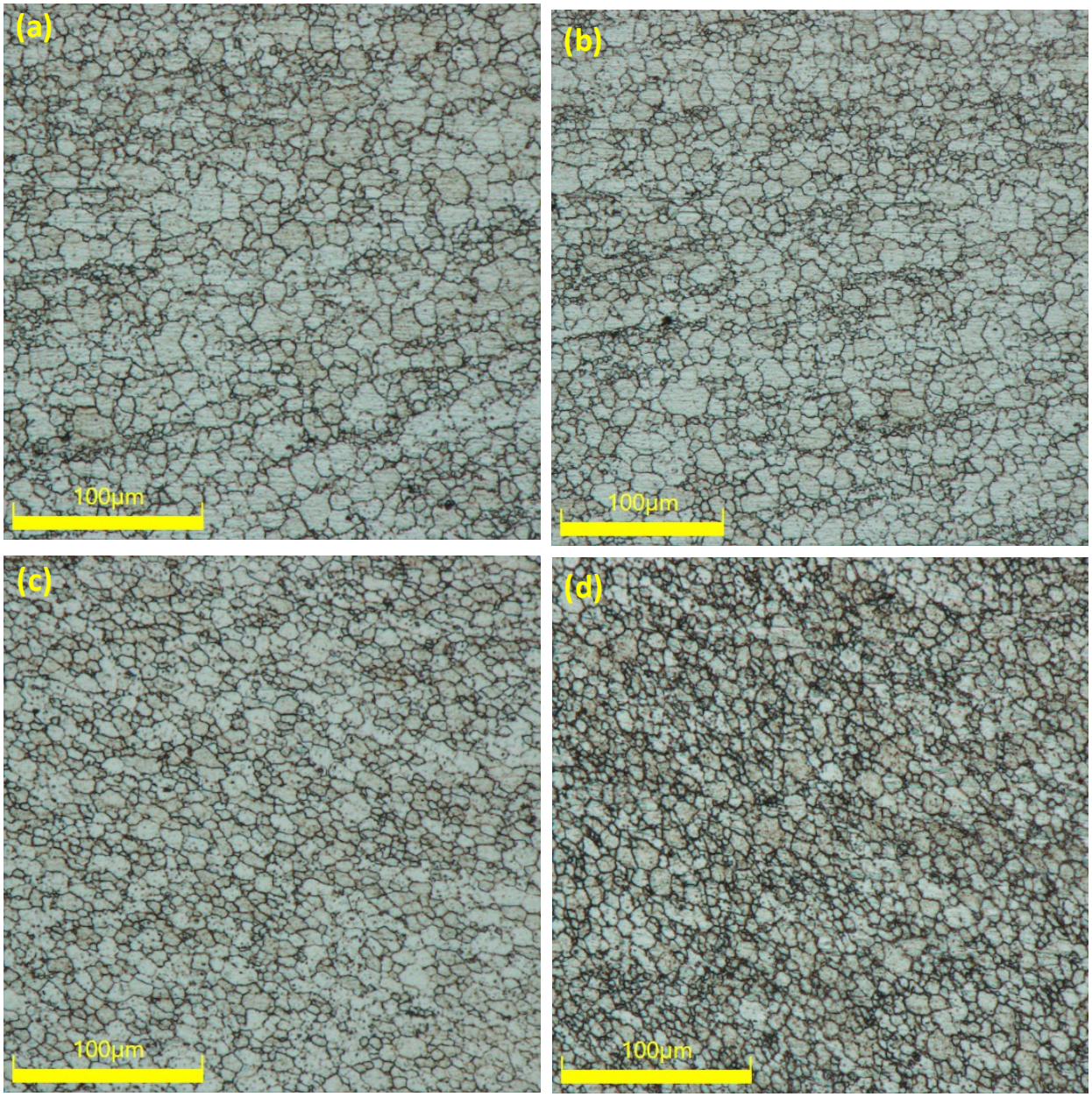

Figure 5- 3 Impact of changing tool traveling speed on the microstructure of the processed zone for samples processed at (a) 50 mm/min, (b) 100 mm/min, (c) 150 mm/min and (d) 200 mm/min

Table 5- 1 Effect of process conditions on heat input and grain size

Samples	Generated torque (N.m)	Heat input (J/mm)	Grain size (μm)
Base	-		34
1000-50	23	2890	12.5
1000-100	26	1633.628	10.3
1000-150	29	1214.749	8.7
1000-200	33	1036.726	7.5

Microstructure across processed zones for samples processed at a constant rotation speed of 1000 rpm and tool traveling speed of 50, 100, 150 and 200 mm/min is displayed in Figure 5- 4. Interestingly, samples processed at 50 mm/min and 100 mm/min showed a similar shape of processed zone. However, rising tool rotation speed from 50 mm/min to 100 mm/min resulted in homogenizing the microstructure and further homogeneity is clearly observed at a higher traveling speed. Three distinct zones namely stir zone (SZ), thermomechanically affected zone (TMAZ) and heat affected zone (HAZ) have been identified. In addition, fine recrystallized grains formation within the stir zone is consequence of frictional heating and severe plastic deformation. Further, the creation of TMAZ during FSP is ascribed to both temperature and deformation. This region is characterized by its deformed unrecrystallized gains resulted from insufficient deformation strain. Moreover, HAZ is located next to TMAZ where no plastic deformation occurs; however, the formation of this region is attributed to thermal cycle. Further, under studied

process parameters no defects were captured, and basin shaped of stir zone with wide top region was detected.

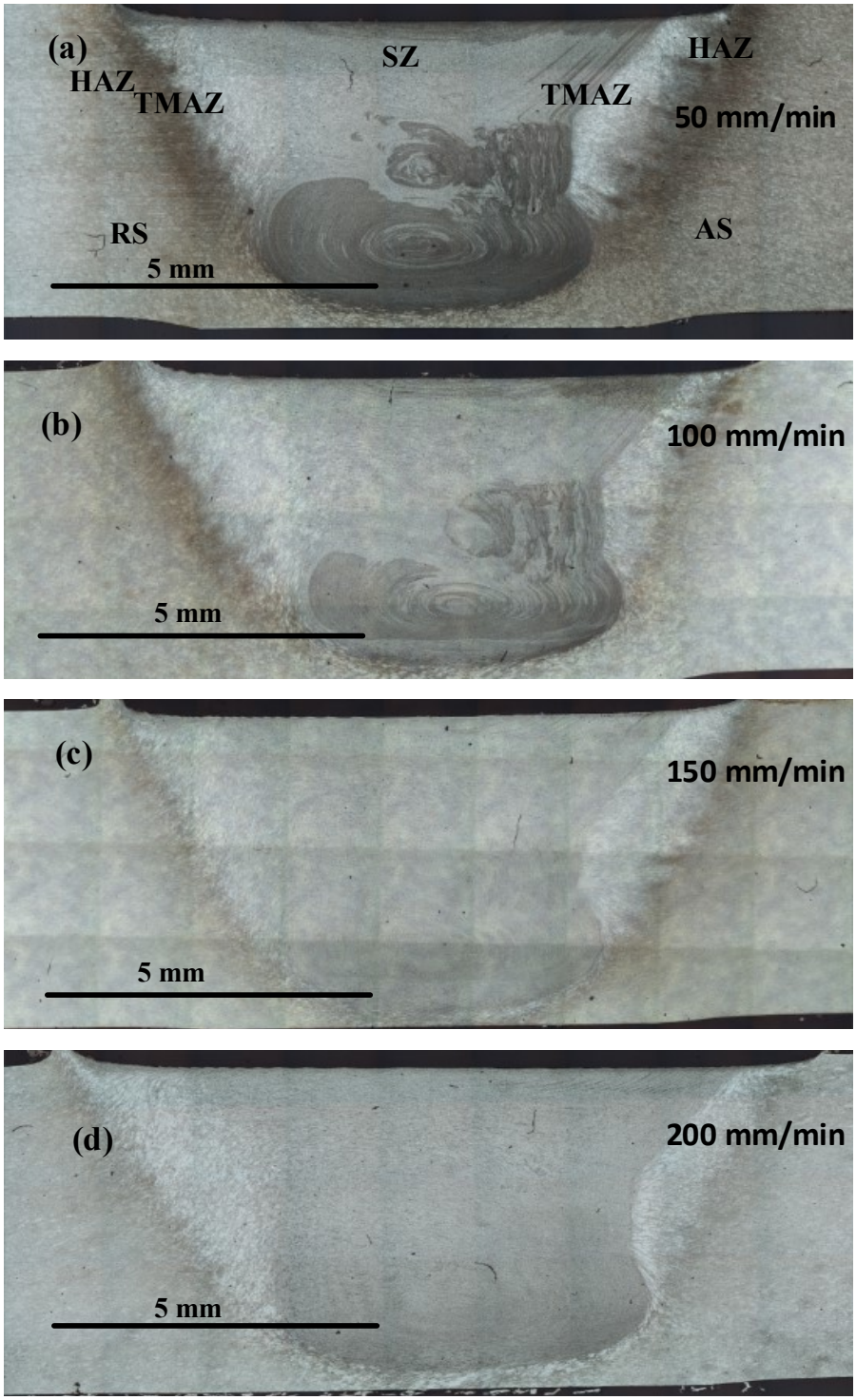

Figure 5- 4 Optical images across the processed zone for samples processed at a constant rotational speed of 1000 rpm and different traveling speeds.

5.1.3 Electrochemical behavior

5.1.3.1 Electrochemical impedance spectroscopy (EIS)

Electrochemical impedance spectroscopy (EIS) has been widely used to characterize the electrochemical properties of metal surfaces. Electrochemical impedance spectroscopy was carried out to investigate the impact of changing traverse speed over a wide range from 50 mm/min to 200 mm/min at a constant interval of 50 mm/min during friction stir processing of 2099 AA on corrosion protection performance. Nyquist plots after immersing all samples (base and processed) for 7 days in 3.5 NaCl are depicted in Figure 5- 5. It is clear from the figure that all samples have revealed the same behavior where two capacitive loops (two times constant) are clearly found over the entire frequency range. Additionally, diameters of unfinished circles have shown remarkable variance between all samples where all samples processed at different traveling speeds have demonstrated higher unfinished arc when compared with the base sample which reflected the better corrosion resistance offered by surface processing. Moreover, the sample processed at the lowest traveling speed, i.e. 1000-50, has shown the smallest unfinished arc among all processed samples which followed by 1000-150 and 1000-200 samples that exhibited comparatively the same radii. In addition, the sample processed at a traveling speed of 100 mm/min showed the highest corrosion resistance among all samples processed at different traveling speeds.

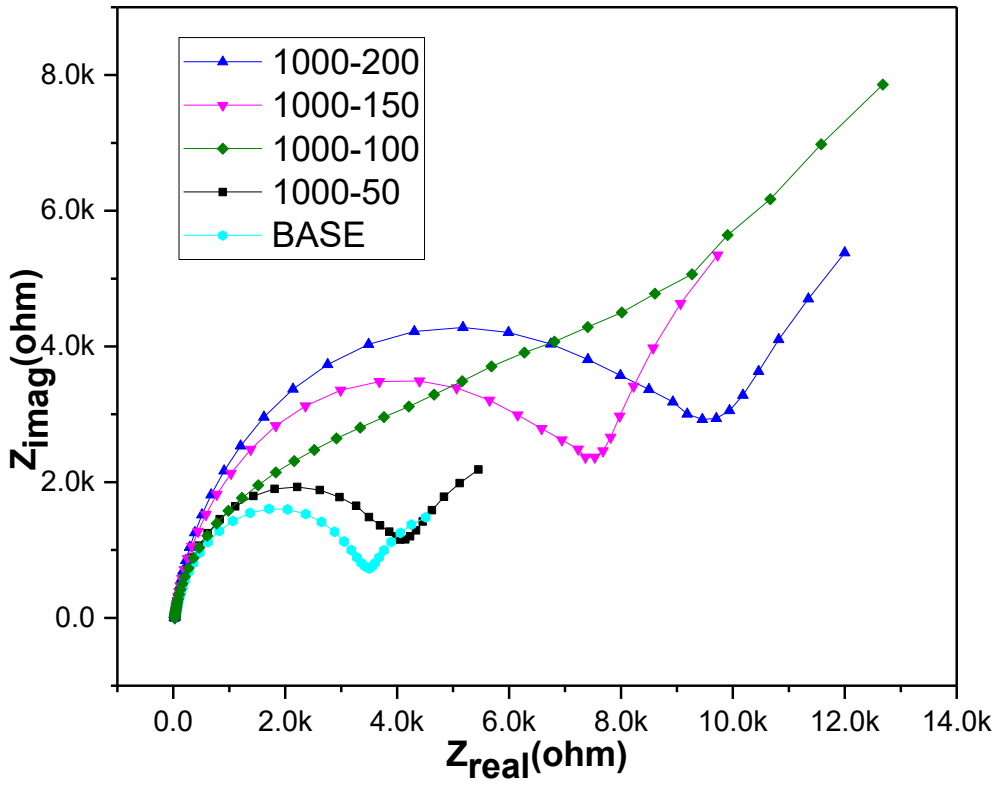

Figure 5- 5 Nyquist plots for samples processed at different traveling speeds after 7 days of immersion in 3.5% NaCl

Typical impedance and phase angle plots for samples processed at several traveling speeds as well as the base sample (unprocessed) after 7 days of immersion in 3.5% NaCl are depicted in Figure 5- 6. As obviously seen in the graph, the lowest impedance was detected for the base sample while, after samples processing via FSP, impedance illustrated remarkable increment. Moreover, samples processed at higher traveling speeds have shown relatively same impedance whereas, the sample processed at the lowest traveling speed demonstrated the lowest impedance in comparison to other processed samples; however, its impedance still noticeably higher than that of the base sample. Furthermore, the base

sample, as well as the sample processed at the lowest traveling speed revealed relatively narrower phase peak as compared to higher traveling speeds samples. It worth mentioning that peak widening for higher speeds samples is possibly attributed to enhancement in passive protective film over a wider frequency range and therefore better corrosion resistance. As clearly depicted from the figure that the phase angle maxima for all samples were far less than 90°.

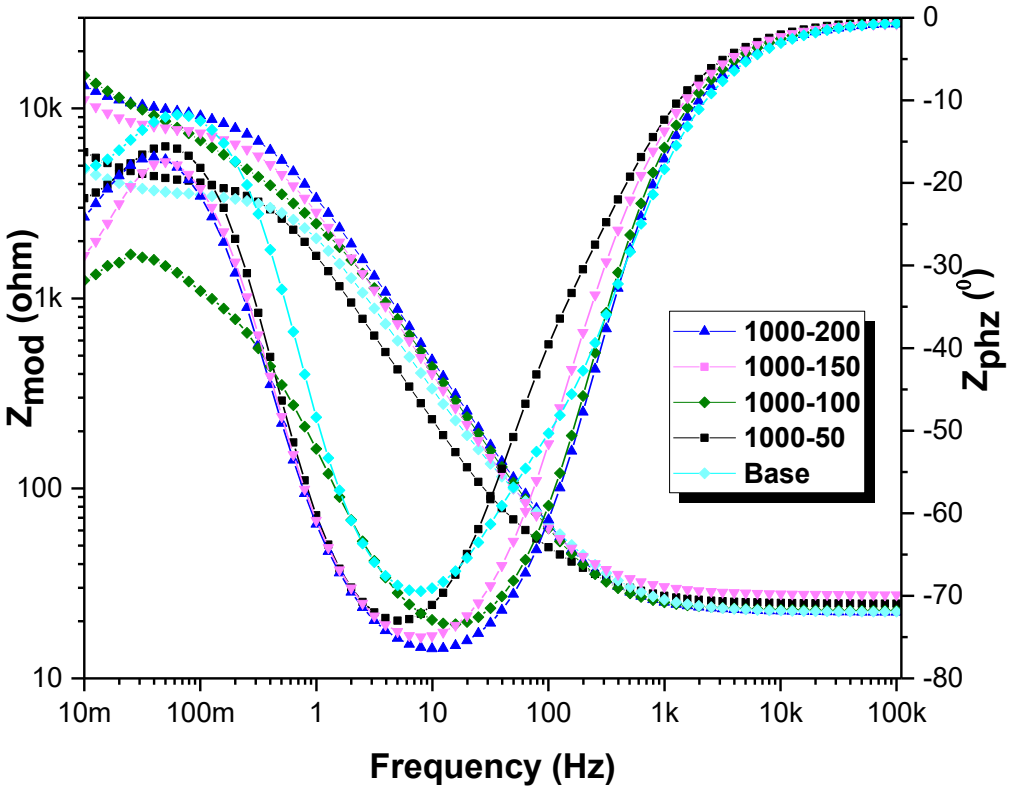

Figure 5- 6 Impedance and phase angle plots for samples processed at different traveling speeds after 7 days of immersion in 3.5% NaCl

For further numerical analysis of barrier characteristics, all EIS plots for all samples were fitted to corresponding circuit which contained solution resistance (R_S) serially connected

to 3 circuits each one of them include constant phase element (CPE) parallelly connected to resistance as depicted in Figure 5- 7. Electrochemical parameters obtained after fitting EIS data of samples processed at different traveling speeds are listed in Table 5- 2. It is clearly observed from the table that the lowest total resistance was seen for the base sample and all processed samples exhibited an improved corrosion resistance. In addition, the sample processed at the lowest traveling speed (1000-50) showed the lowest total resistance among all processed samples. Moreover, rising tool traveling speed to 100 mm/min, significantly improve the total resistance to its peak. Furthermore, both samples processed at 150 mm/min and 200 mm/min exhibit a total resistance lower than that of the sample processed at 100 mm/min; however, the later samples showed total resistance noticeably higher than that of the sample processed at 150mm/min. Additionally, a significant reduction in CPE component of the outer circuit (Y_f) is clearly seen for all processed samples compared to the base metal. This reduction is generally attributed to the reduction in activeness of the surface which resulted from the formed passive film [113][114].

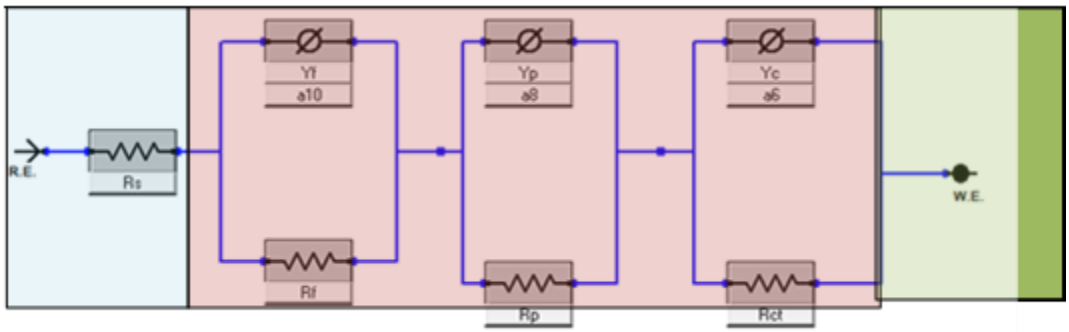

Figure 5- 7 Equivalent circuit for all samples

Table 5- 2 Electrochemical parameters obtained from EIS plots

Samples	$R_s(\Omega)$	R_f *E+3 (k Ω)	R_{ct} *E+3 (k Ω)	R_p *E+3 (k Ω)	Y_p *E-5(*)	a6	Y_c *E-4(*)	a8	Y_f *E-5(*)	a10	R_t (k Ω)	Chi *E-5
base	22.43	3.25	3.49	0.04	6.91	0.93	2.04	0.80	693	0.98	6.78	3.09
1000-50	24.54	4.15	0.02	4.48	39.4	0.74	53.6	1.00	9.85	0.93	8.86	4.15
1000-100	22.65	5.32	1.13	30.8	8.77	1.00	7.08	0.76	15.6	0.86	37.3	39.8
1000-150	27.31	17.3	7.27	2.25	6.01	0.93	32.4	0.55	296	0.98	26.8	8.11
1000-200	22.29	21	9.31	0	5.14	0.91	2.27	0.86	167	0.85	30.3	4.45

$*=S*s^a$

5.1.3.2 Potentiodynamic Polarization (PDP)

Figure 5- 8 shows typical potentiodynamic polarization curves for different samples after 1 week of immersion in 3.5% NaCl. Table 5- 3 presents several electrochemical parameters obtained from fitting of PDP curves, namely corrosion current density I_{corr}, corrosion potential E_{corr}, cathodic and anodic Tafel slopes (β_c&β_a). It is clear from the figure that most of the processed samples displayed a shift to positive corrosion potential. Interestingly, the only processed sample with a more negative corrosion potential when compared to the base sample was (1000-50) sample which exhibited a noticeable improvement in pitting potential. The inspection of Table 5- 3 revealed that the highest corrosion current density (I_{corr}) and therefore the worst corrosion performance was observed for the base sample with I_{corr} of 3.55 uA. Moreover, deploying FSP at the lowest traveling speed resulted in a considerable drop in I_{corr} to about 2.15 µA. Furthermore, with further increment in traveling speed from 100 to 150 mm/min, the resulted I_{corr} exhibited a significant drop comparing with the base sample from 0.282 µA to 0.268 µA. However,

processing the surface at the highest traveling speed of 200 mm/min resulted in a significant increment in I_{corr} to approximately 1.6 µA.

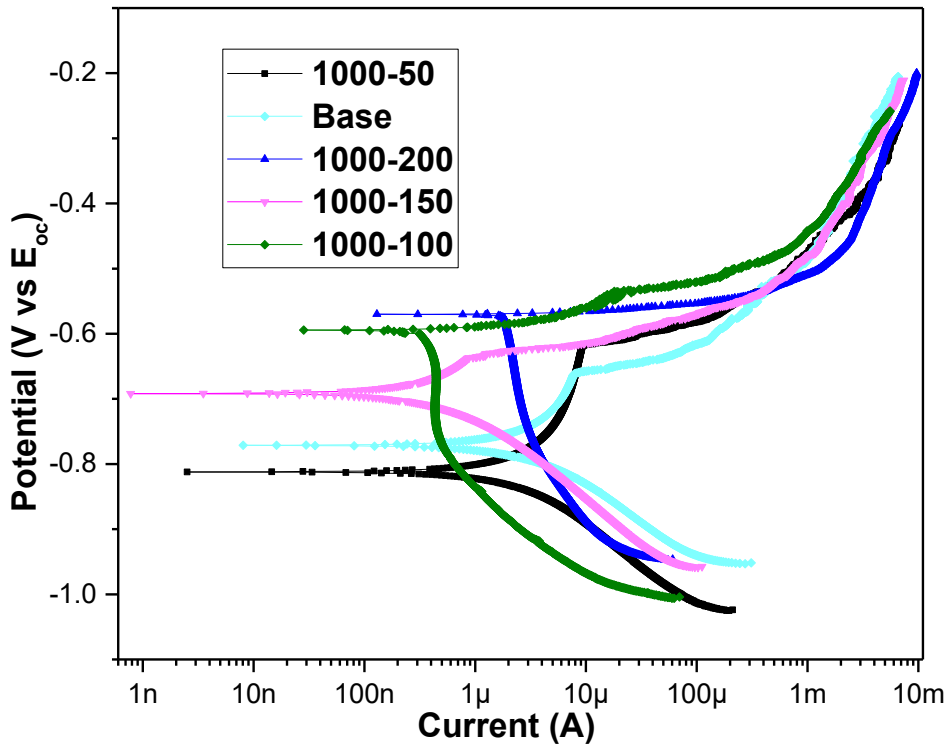

Figure 5- 8 PDP curves for the base sample and samples processed at different traveling speed after 7 days of immersion in 3.5% NaCl

Table 5- 3 Results obtained from PDP test for the base and processed samples at different traveling speed

Samples	βa (V/decade)	βc (V/decade)	I_{corr} (µA)	E_{corr} (mV)	Corrosion rate (mpy)
Base	2.17E-01	1.05E-01	3.55	-771	1.563
1000-50	1.35E-01	9.56E-02	2.15	-812	0.95
1000-100	5.46E-02	4.47E-01	0.282	-594	0.12
1000-150	8.09E-02	5.88E-02	0.268	-692	0.12
1000-200	8.92E-02	4.66E-01	1.6	-567	0.70

5.1.3.3 Linear Polarization Resistance (LPR)

Linear polarization curves for samples processed at different traveling speeds as well as the base sample after immersion for 1 week in 3.5 % NaCl is depicted in Figure 5- 9. The linear polarization resistance (R_P) was found from the slope of lines. Consequently, the Stern Gearty equation (eq. 4.4) was used to get corrosion current density I_{corr} utilizing the Tafel slopes β_a and β_b which were acquired from PDP curves. Table 5- 4 shows polarization resistance (R_p), corrosion current density (I_{corr}) and corrosion rate. Careful inspection of the table demonstrated that the highest corrosion current density and therefore corrosion rate was detected for the base sample whereas all processed samples revealed an improved corrosion resistance. It is evident from the table that the sample processed at the lowest traveling speed (1000-50) showed the poorest corrosion performance among all processed samples and with traveling speed rising the corrosion rate exhibited a remarkable reduction.

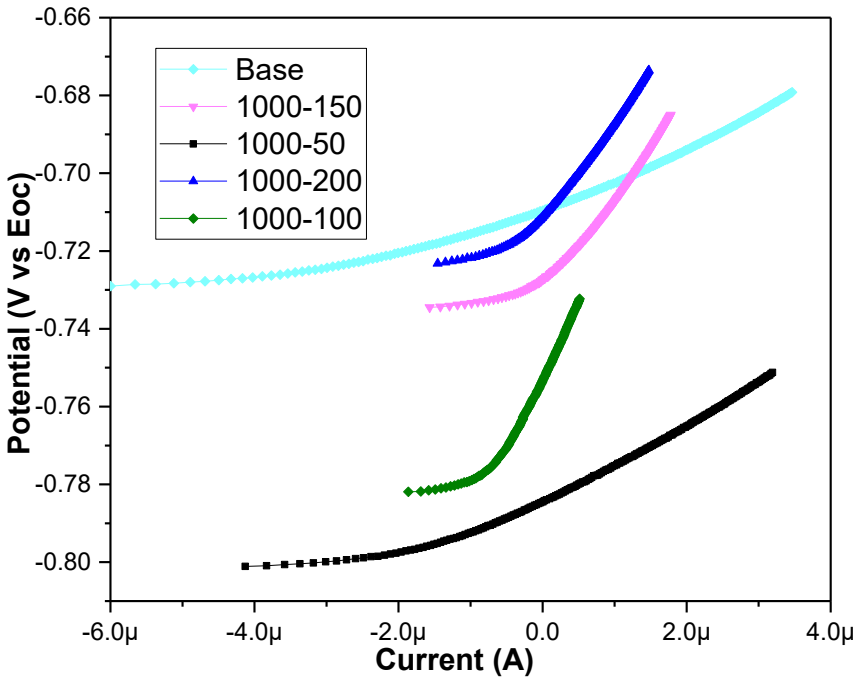

Figure 5- 9 LPR curves for the base sample and samples processed at different traveling speed after 7 days of immersion in 3.5% NaCl.

Table 5- 4 Results obained from LPR curves

Samples	$I_{corr.}$ (μA)	R_P (kohms)	Corrosion rate (mpy)
Base	3.273	7.96	1.441
1000-50	2.591	10.05	1.141
1000-100	0.676	38.57	0.298
1000-150	0.995	26.18	0.438
1000-200	0.987	26.39	0.435

5.1.3.4 SEM images for corroded samples processed at different traveling speeds

SEM images of different samples processed at several traveling speeds and the base counterpart after exposure to sodium chloride environment for 1 week is presented in Figure 5- 10. It is evident from the figure that corrosion pits are clearly noticed on the surfaces of the base as well as the sample processed at the lowest traveling speed as seen in Figure 5- 10 (a and b). Additionally, increasing tool traveling speed from 100 mm/min to 200 mm/min resulted in reducing the adhesion of corrosion products on aluminum surfaces as shown in Figure 5- 10 (c, d and e).

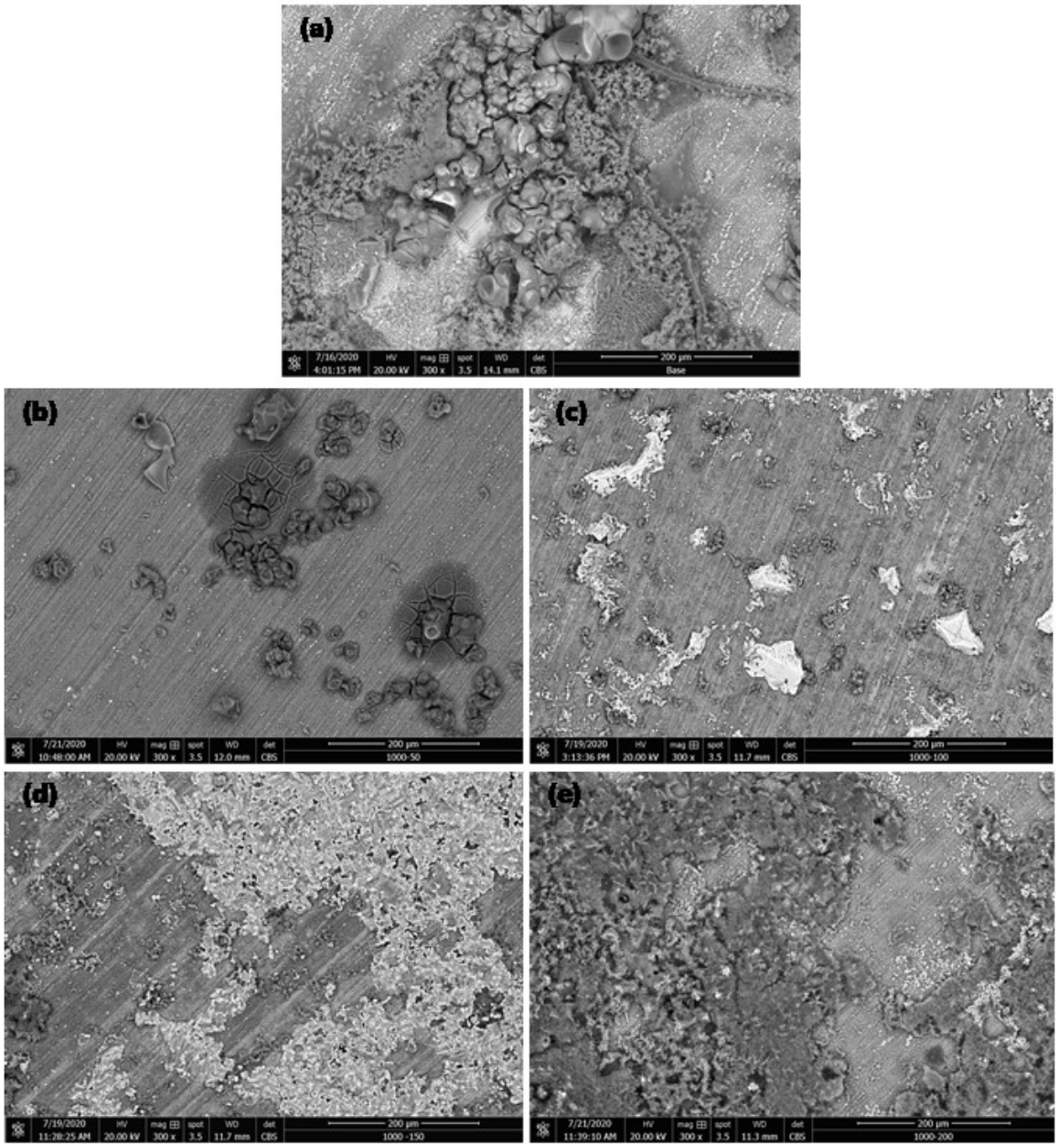

Figure 5- 10 SEM images for (a) base, (b) 1000-50, (c) 1000-100, (d) 1000-150, (e) 1000-200 samples after 7 immersion days in 3.5 % NaCl

5.2 Effect of changing rotation speed

5.2.1 Generated torque

Spindle torque resulted from changing tool rotation speed 800 to 1200 rpm at a fixed traveling speed of 150 mm/min is presented in Figure 5- 11 Influence of changing tool rotation speed on spindle torque. As observed from the figure that processing the sample at the lowest rotational speed of 600 rpm resulted in spindle torque of approximately 46 N.m. Moreover, rising tool rotational speed from 800 to 1000 rpm resulted in reducing spindle torque from about 36 N.m to around 29 N.m and far reduction in spindle torqued to 25 N.m is noticed upon increasing tool rotation speed to 1200 rpm.

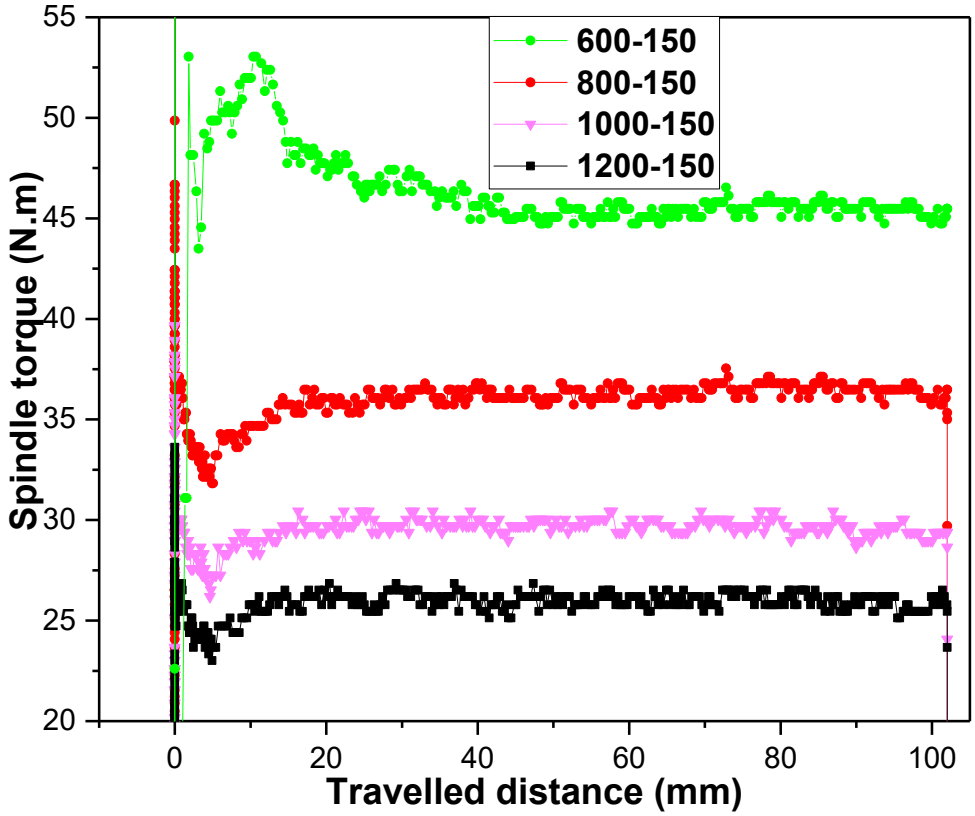

Figure 5- 11 Influence of changing tool rotation speed on spindle torque

5.2.2 Microstructure analysis

The impact of increasing tool rotating speed from 600 up to 1200 rpm while keeping the tool traverse speed constant at 150 mm/min on the microstructure of processed surfaces is depicted in Figure 5- 12 (a), (b), (c) and (d). It is evident from the figure that FSP markedly alters the microstructure where the grain sizes of all processed samples are significantly lower than that of the as extruded specimen. In addition, recrystallized and relatively homogenous grains are clearly observed in the center of processed zones. Moreover, the grains exhibit a slight coarsening after rising tool traveling speed from 600 to 1200 rpm. The impact of varying tool rotational speed at constant traveling speed of 150 mm/min on generated torque, heat input and grain size is listed in Table 5- 5. It is obvious from the table that increasing tool rotation speed resulted in a noticeable reduction generated torque, while heat input and grain size marginally increased. The grain coarsening with rotation speed increasing is due to the increase in heat input that plays a vital role in determining the grain size.

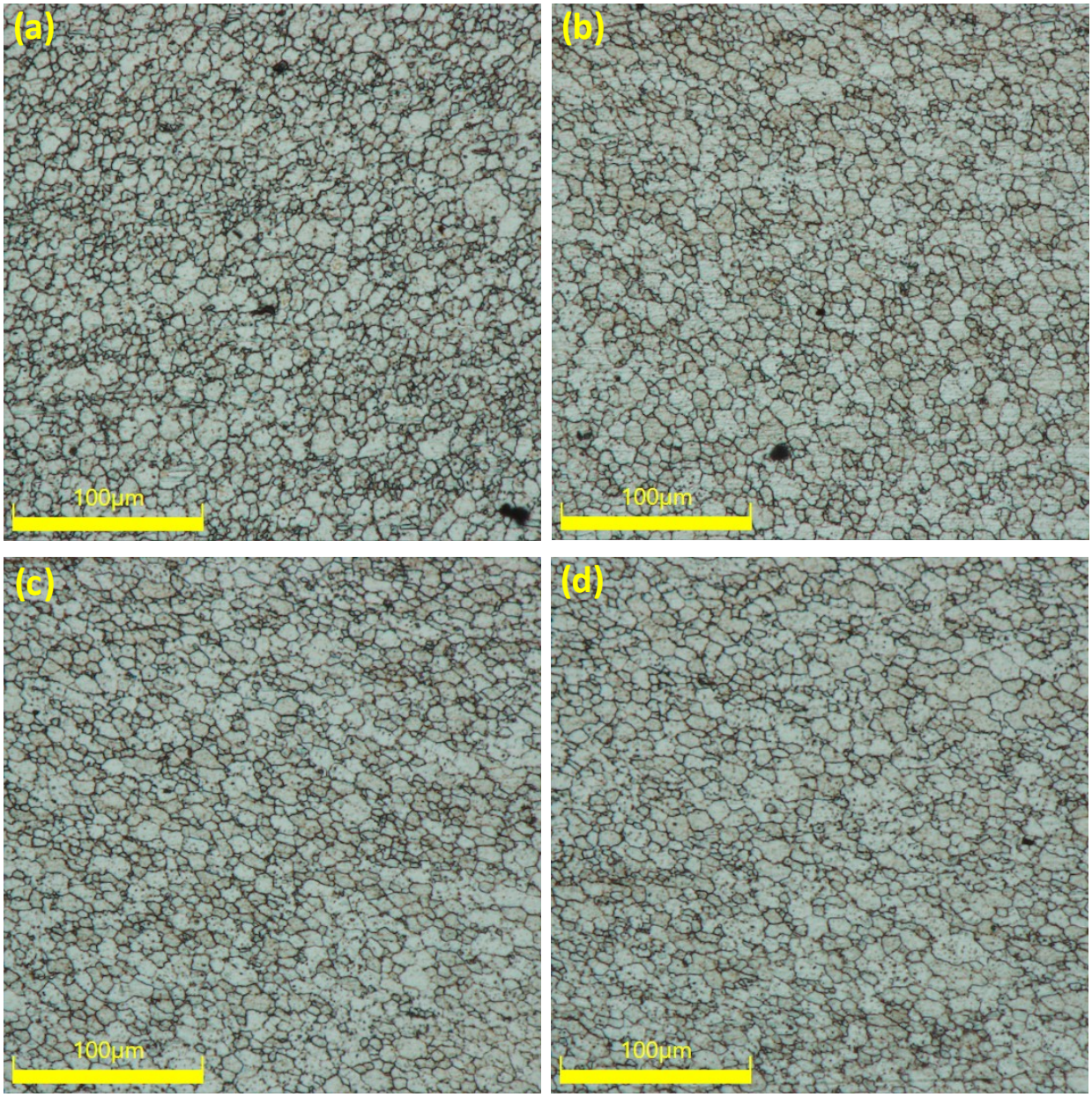

Figure 5- 12 Impact of changing tool rotation speed on the microstructure of the processed zone for samples processed at (a) 600 rpm, (b) 800 rpm, (c) 1000 rpm, (d) 1200 rpm

Table 5- 5 Effect of process conditions on heat input and grain size

Samples	Generated torque (N.m)	Heat input (J/mm)	Grain size (µm)
Base	-		34
600-150	46	1156	7.5
800-150	36	1206.372	8
1000-150	29	1214.749	8.7
1200-150	25	1256.637	9.5

Microstructural images across the processed zone for samples processed at 600, 800, 1000 and 1200 rpm are displayed in Figure 5- 13. Four different zones, namely base metal, heat affected zone, thermomechanical affected zone and stir zone can be easily identified. It can be seen that the width of the processed zone is the lowest for the samples processed at 600 rpm and upon rise tool rotation speed, the width of the processed zone relatively increases. In addition, there is an obvious dark area at the bottom of the processed zone of the sample processed at 600 rpm which is a sign of more grain refinement at the bottom. Moreover, the dark bottom region is gradually disappearing with rising tool rotation speed and this may be ascribed to more grain homogeneity across the processed region. Sharp edges were noticed on the advancing sides for all processed samples which is attributed to material flow around the tool.

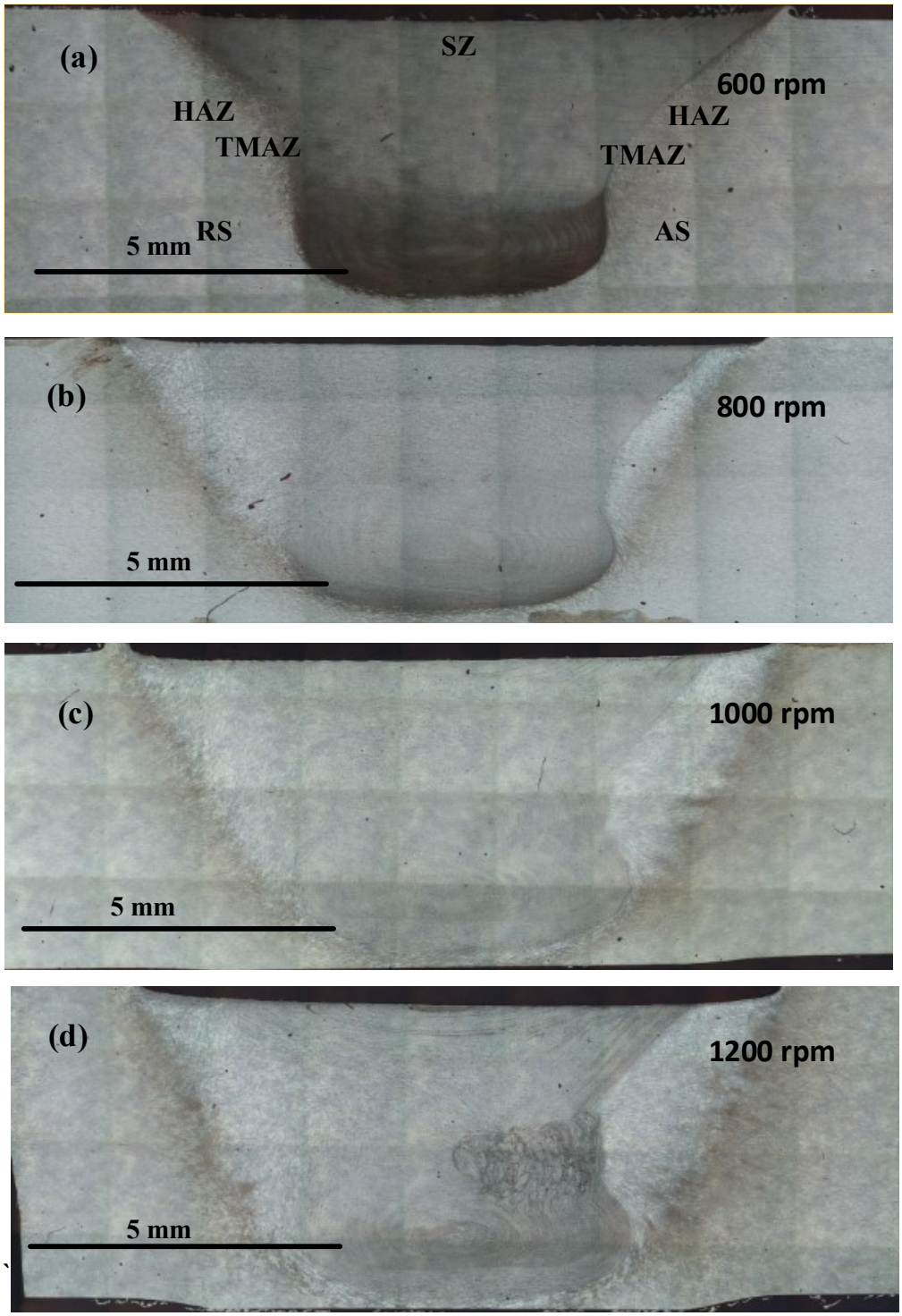

Figure 5- 13 Optical images across the processed zone for samples processed at a constant traveling speed of 150 mm/min and different rotational speeds

5.2.3 Electrochemical behavior

5.2.3.1 Electrochemical impedance spectroscopy (EIS)

Nyquist plots for samples processed at different rotational speeds as well as the base sample after 7 days of immersion in 3.5% NaCl are displayed in Figure 5- 14. It is evident from the figure that two capacitive loops are identified over the entire frequency range where at low frequency is referred to diffusion control process and at high frequency referred to capacitive behavior. In addition, a huge variation in an uncompleted arc was observed between all samples where the lowest radius was detected for the base sample. Moreover, employing FSP at the lowest rotation speed of 600 rpm caused a noticeable increment in radius. Further, samples processed at very high speed showed a remarkable increase in the uncompleted arc radius. It is obvious from the figure that the sample processed at 800 rpm showed the highest arc radius whereas the radius of the sample processed at 1200 rpm is relatively higher than that processed at 1000 rpm.

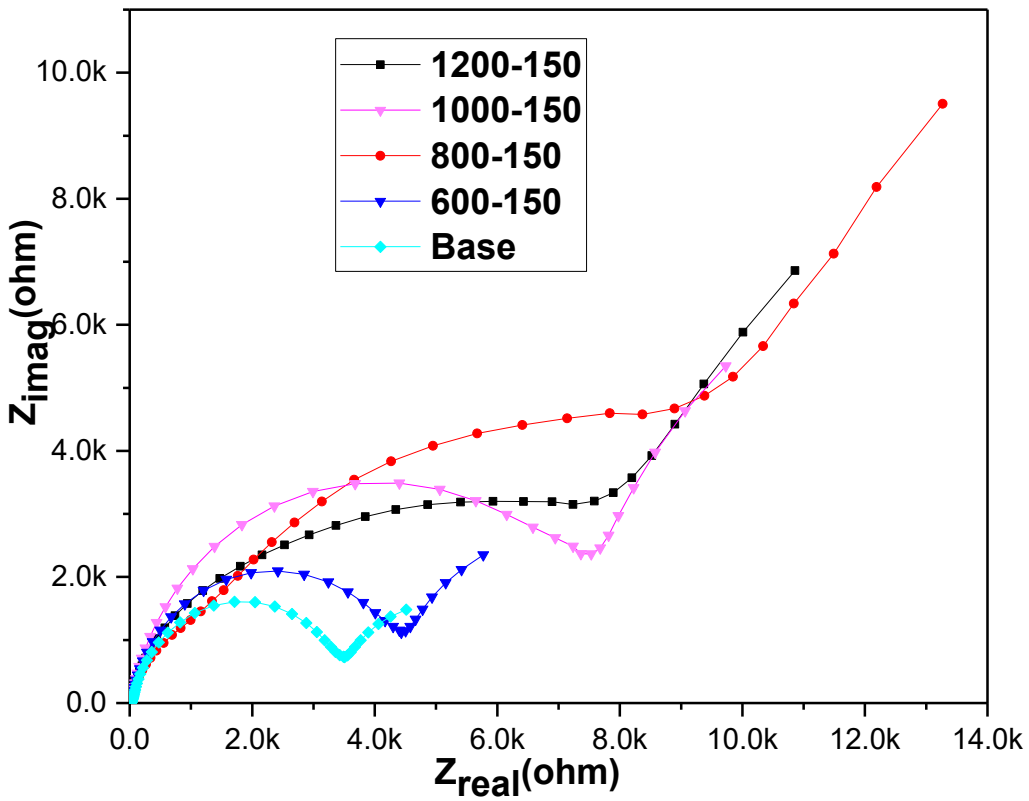

Figure 5- 14 Nyquist plots for samples processed at different rotation speeds after 7 days of immersion in 3.5% NaCl

Impedance and phase angle plots for several samples processed at different rotation speeds and the base sample are depicted in Figure 5- 15. As obviously shown in the figure that the lowest impedance value was reported for the base sample; however, a noticeable increase in total impedance is seen after processed the surface using FSP at the lowest tool rotational speed. Additionally, a remarkable increase in total impedance was observed for various samples processed at higher rotation speeds i.e. 800 rpm, 1000 rpm and 1200 rpm. In addition, it is evident from the figure that the base and 600-150 samples are shown the narrowest peaks among all samples while other processed samples displayed wider peaks.

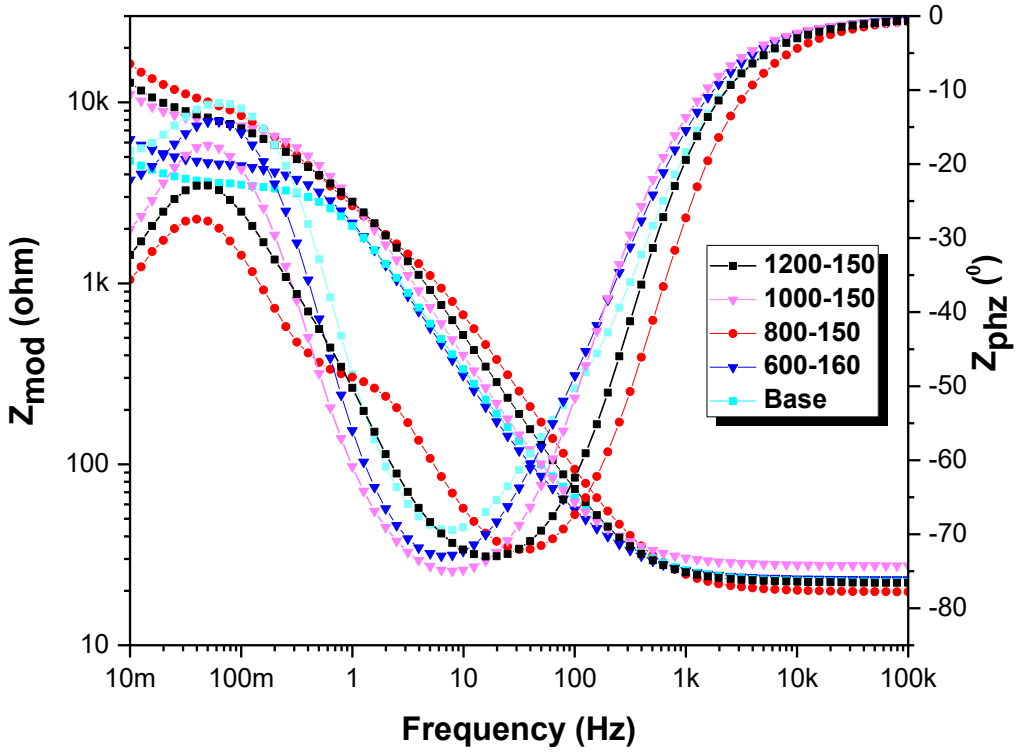

Figure 5- 15 Impedance and phase angle plots for samples processed at different rotation speeds after 7 days of immersion in 3.5% NaCl.

For numerical estimation of electrochemical parameters, all samples were fitted to circuit presented in Figure 5- 7 Equivalent circuit for all samples. Table 5- 6 shows electrochemical parameters acquired from fitting of EIS data for samples processed at different rotation speeds. It is evident from the table that all processed samples showed better corrosion resistance when compared to the unprocessed counterpart. Additionally, the lowest total resistance among all processed samples was detected for the sample processed at lowest rotational speed of 600 rpm, whereas the highest total resistance was observed for the sample processed at 800 rpm. Moreover, rising tool rotational speed from 1000 rpm to 1200 rpm significantly increase the total resistance. Furthermore, phase

element component (Y_f) exhibited a significant reduction for all processed samples when compared to the base sample which revealed the reduction in surface activeness due to formation of dense passive film.

Table 5- 6 Electrochemical parameters obtained from EIS plots

Samples	R_s(Ω)	R_f *E+3 (k Ω)	R_{ct} *E+3 (k Ω)	R_p *E+3 (k Ω)	Y_p *E-5(*)	a6	Y_c *E-4(*)	a8	Y_f *E-5(*)	a10	R_t (k Ω)	Chi *E-5
base	22.43	3.25	3.49	0.04	6.91	0.93	2.04	0.80	693	0.98	6.78	3.09
600-150	22.95	4.43	0.024	6.9	40	0.75	41.8	0.92	7.17	0.94	11.42	1.85
800-150	19.79	1.09	67.23	7.9	89.5	0.80	1.18	0.86	5.02	0.93	76.34	4.39
1000-150	27.31	17.29	7.27	2.25	6.01	0.93	32.4	0.55	296	0.98	26.81	8.11
1200-150	22.22	5.28	2.2	36.7	7.17	0.91	12.5	0.81	16	0.88	44.24	6.91

=Ss^a

5.2.3.2 Potentiodynamic polarization (PDP)

Potentiodynamic polarization plots for samples processed at different rotational speeds and the base counterpart after 7 immersion days in 3.5% NaCl are shown in Figure 5- 16. Different electrochemical parameters obtained from plots fitting are displayed in Table 5- 7. It is clear that all processed samples exhibited a shift toward more positive potential. In addition, the pitting potential of all processed samples remarkably improved. The highest corrosion current density was found for the base sample while all processed samples had displayed an enhanced corrosion resistance, as can be depicted from Table 5- 7. Besides, the lowest corrosion rate was found for the sample processed at the highest rotation speed of 1200 rpm, and with reducing tool rotation speed to 1000 rpm, the corrosion rate marginally increased. Moreover, the sample processed at the lowest rotation speed of 600

rpm showed higher corrosion resistance when compared to that of the sample processed at 800 rpm.

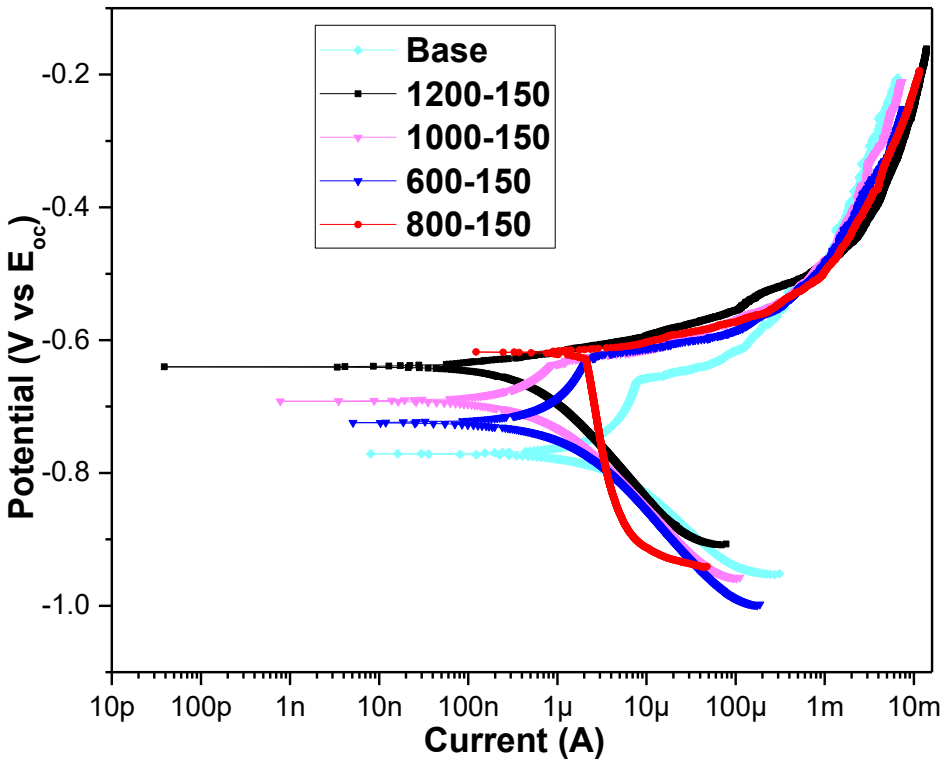

Figure 5- 16 PDP curves for the base sample and samples processed at different rotation speeds after 7 days of immersion in 3.5% NaCl

Table 5- 7 Results obtained from PDP test for the base and processed samples at different rotation speeds

Samples	βa (V/decade)	βc (V/decade)	I_{corr} (μA)	E_{corr} (mV)	Corrosion rate (mpy)
Base	2.17E-01	1.05E-01	3.55	-771	1.563
600-150	4.24E-01	1.50E-01	1.53	-724	6.74E-01
800-150	2.60E-02	1.071	2.37	-618	1.045
1000-150	8.09E-02	5.88E-02	0.268	-692	1.18E-01
1200-150	3.57E-02	8.87E-02	0.203	-640	8.96E-02

5.2.3.3 Linear polarization resistance (LPR)

Figure 5- 17 shows linear polarization plots for samples processed at several rotation speeds after immersion for 1 week in 3.5% NaCl. Polarization resistance obtained as a slope is used to calculate the corrosion rate using the Stern Gary equation (eq. 4.4). Table 5- 8 displays corrosion rates for different samples. It is evident from the table that the highest corrosion rate was detected for the base sample. In addition, processing sample at the lowest rotation speed of 600 rpm resulted in a significant enhancement in corrosion resistance compared to the base sample. Rising tool rotation speed to 800 rpm resulted in reducing the corrosion rate to approximately one-fourth of that for 600-150 sample. Moreover, processing sample at the highest rotation speed of 1200 rpm resulted in higher corrosion resistance when compared to that of the sample processed at 1000; it is however, lower than that of the sample processed at 800 rpm.

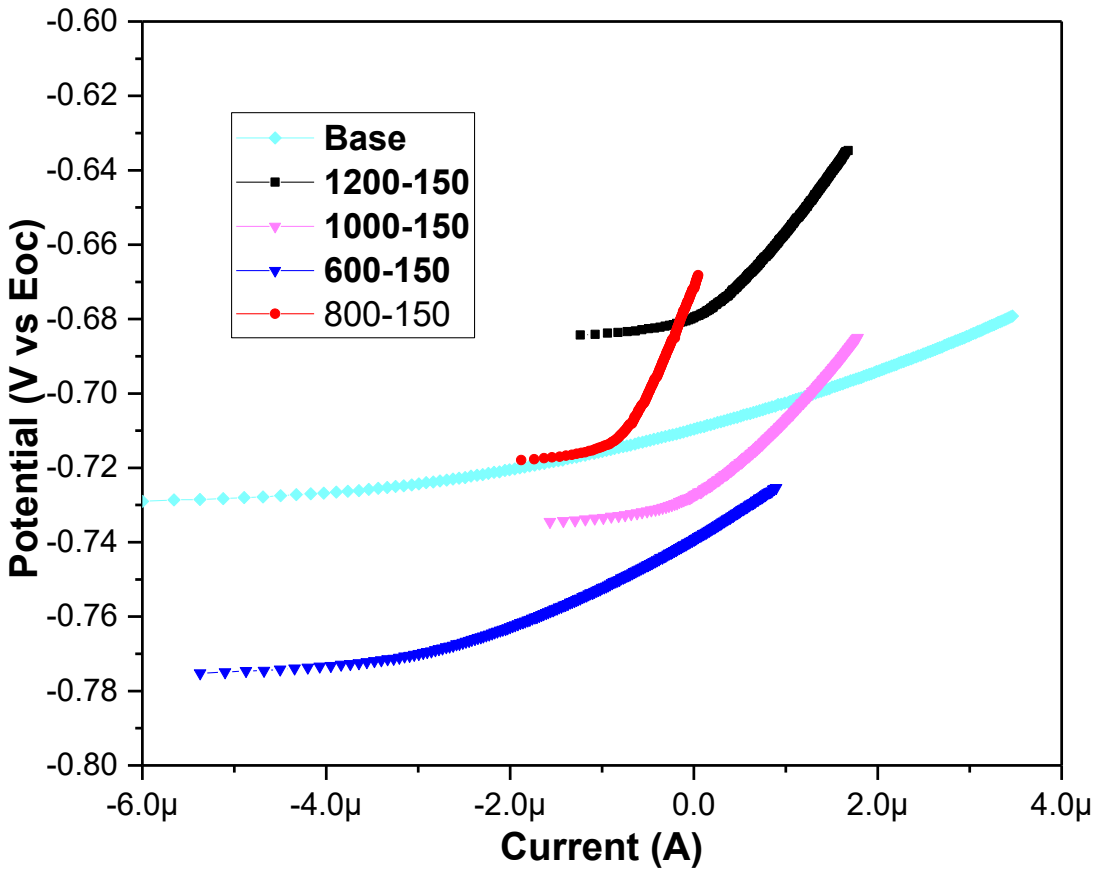

Figure 5- 17 LPR curves for the base sample and samples processed at different rotation speed after 7 days of immersion in 3.5% NaCl

Table 5- 8 Results obained from LPR curves

Samples	$I_{corr.}$ (μA)	R_P (kohms)	Corrosion rate (mpy)
Base	3.273	7.96	1.441
600-150	1.972	13.21	8.69E-01
800-150	0.461	56.51	2.03E-01
1000-150	0.995	26.18	4.38E-01
1200-150	0.839	31.03	3.70E-01

5.2.3.4 SEM images for corroded samples processed at different rotational speeds

After finalizing the corrosion test, all corroded surfaces of processed and base samples were examined using SEM. Corrosion morphology of samples processed at different rotation speeds as well as the base sample after exposure to 3.5% NaCl for 1 week is depicted in Figure 5- 18. SEM images indicated a high severity of corrosion attack on the base sample compared to other processed samples. In addition, localized pits can be clearly observed especially around the corrosion products as shown in Figure 5- 18 (a, b and c). Moreover, the corrosion products are hardly detected on the surface of the sample processed at the highest rotation speed while a porous film of corrosion products was formed on the top of the sample processed at 1000 rpm as seen in Figure 5- 18 (e and d).

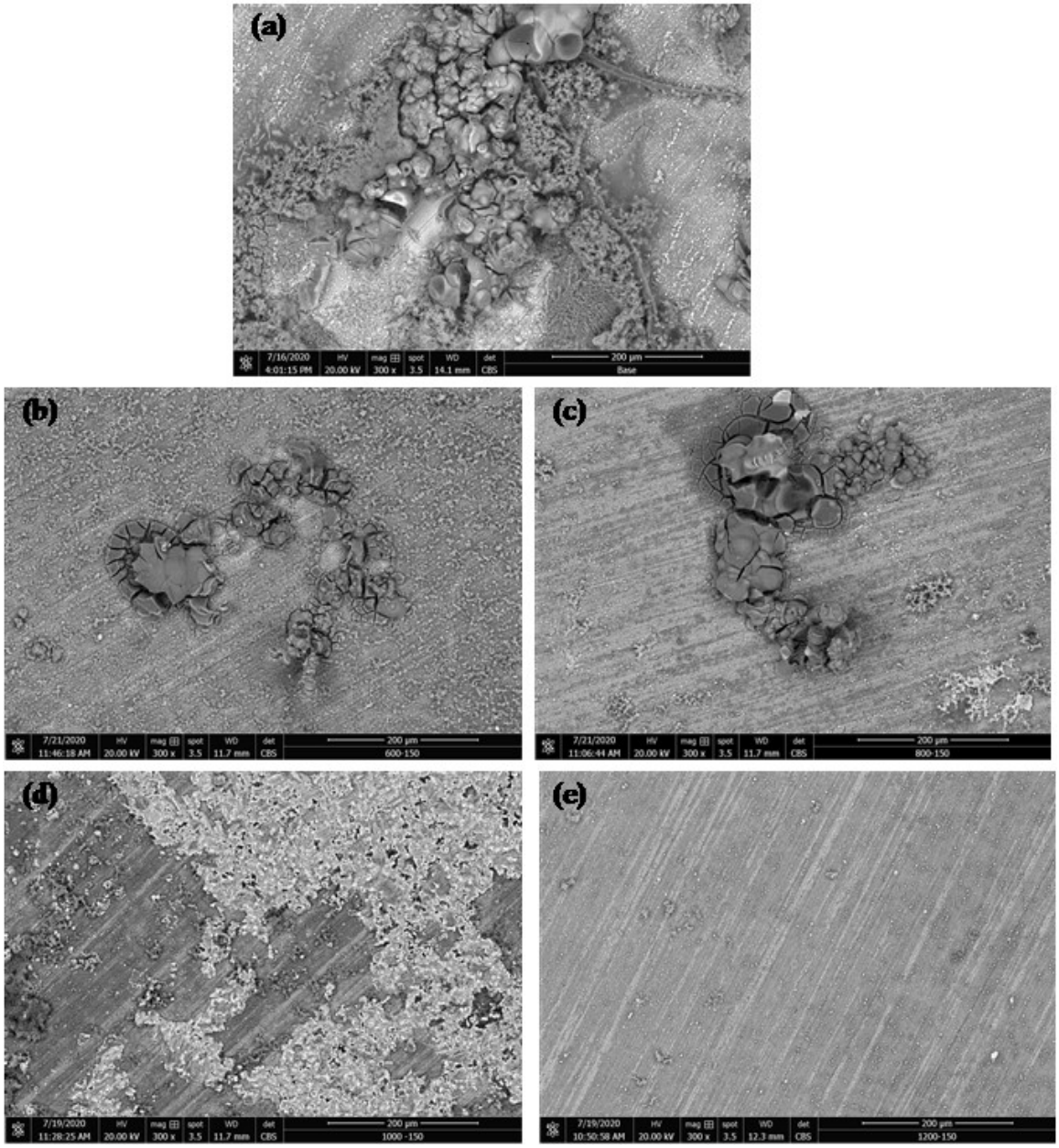

Figure 5- 18 SEM images for (a) base, (b) 600-150, (c) 800-150, (d) 1000-150, (e) 1200-150 samples after 7 immersion days in 3.5 % NaCl

5.3 Discussion

It is to be noted that several precipitates maybe exist along grain boundaries or/and within grains of Al-Cu-Li alloys such as $T_1(Al_2CuLi)$, $\delta'(Al_3Li)$, $\theta'(Al_2Cu)$, $\beta'(Al_3Zr)$ and -$S'(Al_2CuMg)$ [151]. The impact of FSW on precipitations formation and dissolution of Al-Cu-Li alloys was extensively investigated so far [76][77][152][153][154][155][156]. For example, Liu et al. [76] have reported that friction stir welding of Al-Cu-Li at lower rotational speed markedly reduced the density of T1 + δ' + β' precipitates and remarkably improve their distribution in weld nugget. In addition, further increment in tool rotation speed resulted in the complete dissolution of precipitates in the aluminum matrix. Likewise, Qin et al. [77] have disclosed that FSW of 2095 AA has resulted in the complete dissolution of $T_1(Al_2CuLi)$ precipitates in the nugget zone. Influence of FSW on 2099AA precipitates was investigated by Lin et al. [155]. The results showed that $T_1(Al_2CuLi)$, $\delta'(Al_3Li)$ precipitates that existed in the base metal completely dissolved first; however, $\delta'(Al_3Li)$ phase reprecipitated subsequently. Similarly, $T_1(Al_2CuLi)$ precipitate completely dissolved into Al matrix after FSW of 2198 AA [156]. The impact of changing tool traveling speed during FSW of 2060 on precipitates was studied by Mao et al. [157]. the obtained results showed that with reducing tool traveling speed, the precipitates were coarsened. Besides, Yan et al. [158] have studied the impact of rising tool rotation speed from 400 rpm to 1300 rpm on the precipitates in 2060 AA. The results showed that increasing rotation speed markedly reduced the density of precipitates and the vast majority of $T_1(Al_2CuLi)$ and $\theta'(Al_2Cu)$ precipitates dissolved which deteriorated the mechanical

properties. In fact, the impact of different precipitates, namely T1, T2, S′, β′, θ′ and Ƞ on corrosion behavior of different Al-Cu-Li alloys was extensively investigated [159][160][161][162] [163][164][165]. There is full agreement between all authors on the behavior of T_1 precipitates [159][163][160][161][162] [166]. It was suggested that T_1 precipitate has more cathodic corrosion potential when compared to the aluminum matrix which resulted in anodic dissolution. Therefore, the enhancement in corrosion resistance that occurred with rotation speed rising may be ascribed to the dissolution of T_1 precipitate into the aluminum matrix. Conversely, the reasons of corrosion resistance improvement after grain refinement of 2099 Al-Li alloy has been revealed by Jinlong et al [132]. The obtained results showed that grain refinement is accompanied by precipitates refinement. Consequently, electron work function exhibited a noticeable reduction which promotes a thicker passive film. Therefore, the enhanced corrosion resistance obtained with increasing traveling speed is attributed to a thicker passive film formed at the surface with finer grain structure.

CHAPTER 6

CONCLUSIONS AND RECOMMENDATIONS

This thesis is encouraged by quickly rising concerns about surface modification using friction stir processing and lack of previous literature in studying the impact of process conditions effect of base material without the addition of additives.

Friction stir processing was successfully applied; under different process parameters, on structural aluminum alloy 6061 and high strength low density third generation Al-Li 2099 T83 alloy. Consequently, under various process conditions, it was found that FSP has a remarkable effect on microstructure, mechanical properties and corrosion resistance whereas wear-resistance was not found to be affected significantly by FSP.

The following conclusions can be reported:

1- It was observed that friction stir processing resulted in considerable grain refinement, where either reducing rotational speed by 2 times or increasing traveling speed (2x) caused marginal grain refinement for both alloys.

2- A significant enhancement in microhardness was reported for all processed samples, where increasing traveling speed resulted in a noticeable reduction in microhardness and reducing tool rotational speed resulted in a remarkable reduction in surface microhardness for 6061-O AA.

3- Several electrochemical techniques were utilized in the current study, namely electrochemical impedance spectroscopy, linear polarization resistance and

potentiodynamic polarization. Outstanding corrosion resistance was achieved after deploying FSP on 6061-O and 2099 T-83 aluminum alloys, where either increasing rotational or traveling speeds caused rapid improvement in corrosion resistance.

4- The wear resistance did not show a major change and the wear mechanisms were mainly adhesive, abrasive and delamination wear. Wear results are in good agreement with previous studies disclosed that the hardness isn't the single dominant factor in determining the improvement or deterioration of wear resistance.

Recommendations

The present investigation shows only the effect of tool rotational and traverse speeds on microstructure and subsequently mechanical, corrosion and wear characteristics. Therefore, the impact of several additional parameters on microstructure, mechanical properties and corrosion resistance can be studied such as:

1- Effect of the number of passes either in the same direction and/or in reverse.

2- Effect of tool design (profile, dimensions, and materials).

3- Effect of forging force (performing FSP under force control).

4- Effect of heat treatment after surface processing.

5- Effect of post processing the samples using pinless tool after bulk material processing.

REFERENCES

[1] Y. Mazaheri, A. Heidarpour, M. M. Jalilvand, and M. Roknian, "Effect of Friction Stir Processing on the Microhardness, Wear and Corrosion Behavior of Al6061 and Al6061/SiO2 Nanocomposites," *J. Mater. Eng. Perform.*, vol. 28, no. 8, pp. 4826–4837, 2019.

[2] S. Kheirkhah, M. Imani, R. Aliramezani, M. H. Zamani, and A. Kheilnejad, "Microstructure, mechanical properties and corrosion resistance of Al6061/BN surface composite prepared by friction stir processing," *Surf. Topogr. Metrol. Prop.*, vol. 7, no. 3, p. 035002, 2019.

[3] N. Seyed Pourmand and H. Asgharzadeh, "Aluminum Matrix Composites Reinforced with Graphene: A Review on Production, Microstructure, and Properties," *Crit. Rev. Solid State Mater. Sci.*, vol. 0, no. 0, pp. 1–49, 2019.

[4] R. S. Mishra and Z. Y. Ma, "Friction stir welding and processing [J]," *Mater. Sci. Eng. R Reports*, vol. 50, no. 1–2, pp. 1–78, 2005.

[5] J. Xu, B. Zou, S. Tao, M. Zhang, and X. Cao, "Fabrication and properties of Al2O3–TiB2–TiC/Al metal matrix composite coatings by atmospheric plasma spraying of SHS powders," *J. Alloys Compd.*, 2016.

[6] J. L. Shi, H. G. Yan, B. Su, J. H. Chen, S. Q. Zhu, and G. Chen, "Preparation of a functionally gradient aluminum alloy metal matrix composite using the technique of spray deposition," *Mater. Manuf. Process.*, 2011.

[7] S. Rathee, S. Maheshwari, A. N. Siddiquee, and M. Srivastava, "A Review of Recent Progress in Solid State Fabrication of Composites and Functionally Graded Systems Via Friction Stir Processing," *Critical Reviews in Solid State and Materials Sciences*. 2018.

[8] S. C. Tjong and Z. Y. Ma, "Microstructural and mechanical characteristics of in situ metal matrix composites," *Mater. Sci. Eng. R Reports*, 2000.

[9] N. Gangil, A. N. Siddiquee, and S. Maheshwari, "Aluminium based in-situ composite fabrication through friction stir processing: A review," *J. Alloys Compd.*, vol. 715, pp. 91–104, 2017.

[10] W. M. Thomas, E. D. Nicholas, J. C. Needham, M. G. Murch, P. Templesmith, and C. J. Dawes, "GB Patent application no. 9125978.8," *Int. Pat. Appl. No. PCT/GB92/02203*, no. 54, 1991.

[11] K. Yang, W. Li, Y. Xu, and X. Yang, "Using friction stir processing to augment corrosion resistance of cold sprayed AA2024/Al 2 O 3 composite coatings," *J. Alloys Compd.*, vol. 774, pp. 1223–1232, 2019.

[12] Z. Y. Ma, "Friction stir processing technology: A review," *Metallurgical and Materials Transactions A: Physical Metallurgy and Materials Science*. 2008.

[13] A. J. Leonard, H. R. Shercliff, and P. J. Withers, "Friction stir welding of aluminium alloys AU - Threadgill, P L," *Int. Mater. Rev.*, vol. 54, no. 2, pp. 49–93, 2009.

[14] Y. N. Zhang, X. Cao, S. Larose, and P. Wanjara, "Review of tools for friction stir welding and processing," *Canadian Metallurgical Quarterly*. 2012.

[15] I. O. for Standardization, "Friction stir welding - Aluminium Part 1: Vocabulary," 2011.

[16] R. S. Mishra, Z. Y. Ma, and I. Charit, "Friction stir processing: A novel technique for fabrication of surface composite," *Materials Science and Engineering A*. 2003.

[17] S. A. Alidokht, A. Abdollah-Zadeh, S. Soleymani, T. Saeid, and H. Assadi, "Evaluation of microstructure and wear behavior of friction stir processed cast aluminum alloy," *Mater. Charact.*, vol. 63, pp. 90–97, 2012.

[18] B. Zahmatkesh, M. H. Enayati, and F. Karimzadeh, "Tribological and microstructural evaluation of friction stir processed Al2024 alloy," *Mater. Des.*, vol. 31, no. 10, pp. 4891–4896, 2010.

[19] N. Yuvaraj, S. Aravindan, and Vipin, "Fabrication of Al5083/B 4 C surface composite by friction stir processing and its tribological characterization," *J. Mater. Res. Technol.*, vol. 4, no. 4, pp. 398–410, 2015.

[20] M. Sivanesh Prabhu, A. Elaya Perumal, S. Arulvel, and R. Franklin Issac, "Friction and wear measurements of friction stir processed aluminium alloy 6082/CaCO3 composite," *Meas. J. Int. Meas. Confed.*, vol. 142, pp. 10–20, 2019.

[21] A. Thangarasu, N. Murugan, I. Dinaharan, and S. J. Vijay, "Synthesis and characterization of titanium carbide particulate reinforced AA6082 aluminium alloy composites via friction stir processing," *Arch. Civ. Mech. Eng.*, vol. 15, no. 2, pp. 324–334, 2015.

[22] C. N. Shyam Kumar, R. Bauri, and D. Yadav, "Wear properties of 5083 Al-W surface composite fabricated by friction stir processing," *Tribol. Int.*, vol. 101, pp. 284–290, 2016.

[23] A. Kurt, I. Uygur, and E. Cete, "Surface modification of aluminium by friction stir processing," *J. Mater. Process. Technol.*, vol. 211, no. 3, pp. 313–317, 2011.

[24] A. Manochehrian, A. Heidarpour, Y. Mazaheri, and S. Ghasemi, “On the surface reinforcing of A356 aluminum alloy by nanolayered Ti3AlC2 MAX phase via friction stir processing,” *Surf. Coatings Technol.*, vol. 377, no. July, p. 124884, 2019.

[25] R. D. Bourkhani, A. R. Eivani, and H. R. Nateghi, “Through-thickness inhomogeneity in microstructure and tensile properties and tribological performance of friction stir processed AA1050-Al2O3 nanocomposite,” *Compos. Part B Eng.*, vol. 174, no. June, p. 107061, 2019.

[26] H. Rana, V. Badheka, A. Kumar, and A. Satyaprasad, “Strategical parametric investigation on manufacturing of Al–Mg–Zn–Cu alloy surface composites using FSP,” *Mater. Manuf. Process.*, vol. 33, no. 5, pp. 534–545, 2018.

[27] S. A. Alidokht, A. Abdollah-zadeh, S. Soleymani, and H. Assadi, “Microstructure and tribological performance of an aluminium alloy based hybrid composite produced by friction stir processing,” *Mater. Des.*, 2011.

[28] N. Yuvaraj, S. Aravindan, and Vipin, “Wear Characteristics of Al5083 Surface Hybrid Nano-composites by Friction Stir Processing,” *Trans. Indian Inst. Met.*, vol. 70, no. 4, pp. 1111–1129, 2017.

[29] H. Eskandari, R. Taheri, and F. Khodabakhshi, “Friction-stir processing of an AA8026-TiB2-Al2O3 hybrid nanocomposite: Microstructural developments and mechanical properties,” *Mater. Sci. Eng. A*, vol. 660, pp. 84–96, 2016.

[30] R. Palanivel, I. Dinaharan, R. F. Laubscher, and J. P. Davim, “Influence of boron nitride nanoparticles on microstructure and wear behavior of AA6082/TiB2 hybrid aluminum composites synthesized by friction stir processing,” *Mater. Des.*, vol. 106, pp. 195–204, 2016.

[31] M. AMRA, K. RANJBAR, and S. A. HOSSEINI, “Microstructure and wear performance of Al5083/CeO2/SiC mono and hybrid surface composites fabricated by friction stir processing,” *Trans. Nonferrous Met. Soc. China (English Ed.*, vol. 28, no. 5, pp. 866–878, 2018.

[32] S. Soleymani, A. Abdollah-zadeh, and S. A. Alidokht, “Microstructural and tribological properties of Al5083 based surface hybrid composite produced by friction stir processing,” *Wear*, vol. 278–279, pp. 41–47, Mar. 2012.

[33] M. JANBOZORGI, M. SHAMANIAN, M. SADEGHIAN, and P. SEPEHRINIA, “Improving tribological behavior of friction stir processed A413/SiCp surface composite using MoS2 lubricant particles,” *Trans. Nonferrous Met. Soc. China (English Ed.*, vol. 27, no. 2, pp. 298–304, 2017.

[34] A. Mostafapour Asl and S. T. Khandani, “Role of hybrid ratio in microstructural,

mechanical and sliding wear properties of the Al5083/Graphite p/Al 2O 3p a surface hybrid nanocomposite fabricated via friction stir processing method," *Mater. Sci. Eng. A*, vol. 559, pp. 549–557, 2013.

[35] R. Srinivasu, A. Sambasiva Rao, G. Madhusudhan Reddy, and K. Srinivasa Rao, "Friction stir surfacing of cast A356 aluminium–silicon alloy with boron carbide and molybdenum disulphide powders," *Def. Technol.*, vol. 11, no. 2, pp. 140–146, 2015.

[36] I. Sudhakar, V. Madhu, G. Madhusudhan Reddy, and K. Srinivasa Rao, "Enhancement of wear and ballistic resistance of armour grade AA7075 aluminium alloy using friction stir processing," *Def. Technol.*, vol. 11, no. 1, pp. 10–17, 2015.

[37] E. R. I. Mahmoud, M. Takahashi, T. Shibayanagi, and K. Ikeuchi, "Wear characteristics of surface-hybrid-MMCs layer fabricated on aluminum plate by friction stir processing," *Wear*, vol. 268, no. 9–10, pp. 1111–1121, 2010.

[38] H. A. Deore, J. Mishra, A. G. Rao, H. Mehtani, and V. D. Hiwarkar, "Effect of filler material and post process ageing treatment on microstructure, mechanical properties and wear behaviour of friction stir processed AA 7075 surface composites," *Surf. Coatings Technol.*, vol. 374, no. May, pp. 52–64, 2019.

[39] R. Hashemi and G. Hussain, "Wear performance of Al/TiN dispersion strengthened surface composite produced through friction stir process: A comparison of tool geometries and number of passes," *Wear*, vol. 324–325, pp. 45–54, 2015.

[40] G. Huang, Y. Shen, R. Guo, and W. Guan, "Fabrication of tungsten particles reinforced aluminum matrix composites using multi-pass friction stir processing: Evaluation of microstructural, mechanical and electrical behavior," *Mater. Sci. Eng. A*, vol. 674, pp. 504–513, 2016.

[41] S. Ahmadifard, A. Momeni, S. Bahmanzadeh, and S. Kazemi, "Microstructure, tribological and mechanical properties of Al7075 / Ti3AlC2 MAX-phase surface composite produced by friction stir processing," *Vacuum*, vol. 155, no. June, pp. 134–141, 2018.

[42] J. Gao, S. Zhang, H. Jin, and Y. Shen, "Fabrication of Al7075 / PI composites base on FSW technology," *Int. J. Adv. Manuf. Technol.*, 2019.

[43] M. Eftekhari, M. Movahedi, and A. H. Kokabi, "Microstructure, Strength, and Wear Behavior Relationship in Al-Fe3O4 Nanocomposite Produced by Multi-pass Friction Stir Processing," *J. Mater. Eng. Perform.*, vol. 26, no. 7, pp. 3516–3530, 2017.

[44] A. Shafiei-Zarghani, S. F. Kashani-Bozorg, and A. Z. Hanzaki, “Wear assessment of Al/Al2O3 nano-composite surface layer produced using friction stir processing,” *Wear*, vol. 270, no. 5–6, pp. 403–412, 2011.

[45] S. K. Patel, V. P. Singh, and B. Kuriachen, “Microstructural, Tribological and Mechanical Properties Evolution of ZrSiO4/A4047 Surface Composite Fabricated through Friction Stir Processing,” *Trans. Indian Inst. Met.*, vol. 72, no. 7, pp. 1765–1774, 2019.

[46] S. S. Mirjavadi *et al.*, “Effect of multi-pass friction stir processing on the microstructure, mechanical and wear properties of AA5083/ZrO2 nanocomposites,” *J. Alloys Compd.*, vol. 726, pp. 1262–1273, 2017.

[47] Y. Chen *et al.*, “Influence of tool pin eccentricity on microstructural evolution and mechanical properties of friction stir processed Al-5052 alloy,” *Mater. Sci. Eng. A*, vol. 739, no. July 2018, pp. 272–276, 2019.

[48] G. Hussain, R. Hashemi, H. Hashemi, and K. A. Al-Ghamdi, “An experimental study on multi-pass friction stir processing of Al/TiN composite: some microstructural, mechanical, and wear characteristics,” *Int. J. Adv. Manuf. Technol.*, vol. 84, no. 1–4, pp. 533–546, 2016.

[49] S. Zhang *et al.*, “Effects of energy input during friction stir processing on microstructures and mechanical properties of aluminum/carbon nanotubes nanocomposites,” *J. Alloys Compd.*, vol. 798, pp. 523–530, 2019.

[50] X. Cao, Q. Shi, D. Liu, Z. Feng, Q. Liu, and G. Chen, “Fabrication of in situ carbon fiber/aluminum composites via friction stir processing: Evaluation of microstructural, mechanical and tribological behaviors,” *Compos. Part B Eng.*, vol. 139, no. December 2017, pp. 97–105, 2018.

[51] A. Sharma, V. M. Sharma, B. Sahoo, S. K. Pal, and J. Paul, “Effect of multiple micro channel reinforcement filling strategy on Al6061-graphene nanocomposite fabricated through friction stir processing,” *J. Manuf. Process.*, 2019.

[52] A. SHARMA, V. M. SHARMA, and J. PAUL, “A comparative study on microstructural evolution and surface properties of graphene/CNT reinforced Al6061−SiC hybrid surface composite fabricated via friction stir processing,” *Trans. Nonferrous Met. Soc. China (English Ed.*, vol. 29, no. 10, pp. 2005–2026, 2019.

[53] A. Sharma, D. Narsimhachary, V. M. Sharma, B. Sahoo, and J. Paul, “Surface modification of Al6061-SiC surface composite through impregnation of graphene, graphite & carbon nanotubes via FSP: A tribological study,” *Surf. Coatings Technol.*, vol. 368, no. February, pp. 175–191, 2019.

[54] A. Sharma, V. M. Sharma, S. Mewar, S. K. Pal, and J. Paul, “Friction stir processing of Al6061-SiC-graphite hybrid surface composites,” *Mater. Manuf. Process.*, vol. 33, no. 7, pp. 795–804, 2018.

[55] R. Maurya, B. Kumar, S. Ariharan, J. Ramkumar, and K. Balani, “Effect of carbonaceous reinforcements on the mechanical and tribological properties of friction stir processed Al6061 alloy,” *Mater. Des.*, vol. 98, pp. 155–166, 2016.

[56] H. Riaz, T. Mnazoor, and A. Raza, “Fabrication and characterization of AA6061/CNTs surface nanocomposite by friction stir processing,” *Int. J. Adv. Manuf. Technol.*, 2019.

[57] M. Balakrishnan, I. Dinaharan, R. Palanivel, and R. Sathiskumar, “Influence of friction stir processing on microstructure and tensile behavior of AA6061/Al 3 Zr cast aluminum matrix composites,” *J. Manuf. Process.*, 2019.

[58] I. Dinaharan, G. Ashok Kumar, S. J. Vijay, and N. Murugan, “Development of Al3Ti and Al3Zr intermetallic particulate reinforced aluminum alloy AA6061 in situ composites using friction stir processing,” *Mater. Des.*, 2014.

[59] M. Balakrishnan, I. Dinaharan, R. Palanivel, and R. Sathiskumar, “Effect of friction stir processing on microstructure and tensile behavior of AA6061/Al3Fe cast aluminum matrix composites,” *J. Alloys Compd.*, 2019.

[60] I. Dinaharan, K. Kalaiselvan, and N. Murugan, “Influence of rice husk ash particles on microstructure and tensile behavior of AA6061 aluminum matrix composites produced using friction stir processing,” *Compos. Commun.*, 2017.

[61] I. Dinaharan, M. Balakrishnan, J. David Raja Selvam, and E. T. Akinlabi, “Microstructural characterization and tensile behavior of friction stir processed AA6061/Al2Cu cast aluminum matrix composites,” *J. Alloys Compd.*, 2019.

[62] M. Barati, M. Abbasi, and M. Abedini, “The effects of friction stir processing and friction stir vibration processing on mechanical, wear and corrosion characteristics of Al6061/SiO2 surface composite,” *J. Manuf. Process.*, 2019.

[63] Z. Zhang *et al.*, “Microstructural evolution and mechanical properties of ZrB2/6061Al nanocomposites processed by multi-pass friction stir processing,” *Mater. Sci. Eng. A*, 2017.

[64] D. Aruri, K. Adepu, K. Adepu, and K. Bazavada, “Wear and mechanical properties of 6061-T6 aluminum alloy surface hybrid composites [(SiC + Gr) and (SiC + Al<inf>2</inf>O<inf>3</inf>)] fabricated by friction stir processing,” *J. Mater. Res. Technol.*, vol. 2, no. 4, pp. 362–369, 2013.

[65] A. Devaraju, A. Kumar, and B. Kotiveerachari, “Influence of rotational speed and reinforcements on wear and mechanical properties of aluminum hybrid composites

via friction stir processing," *Mater. Des.*, vol. 45, pp. 576–585, 2013.

[66] A. Devaraju, A. Kumar, A. Kumaraswamy, and B. Kotiveerachari, "Influence of reinforcements (SiC and Al2O3) and rotational speed on wear and mechanical properties of aluminum alloy 6061-T6 based surface hybrid composites produced via friction stir processing," *Mater. Des.*, vol. 51, pp. 331–341, 2013.

[67] A. Devaraju, A. Kumar, and B. Kotiveerachari, "Influence of addition of Grp/Al2O3p with SiCp on wear properties of aluminum alloy 6061-T6 hybrid composites via friction stir processing," *Trans. Nonferrous Met. Soc. China (English Ed.*, vol. 23, no. 5, pp. 1275–1280, 2013.

[68] S. R. Anvari, F. Karimzadeh, and M. H. Enayati, "Wear characteristics of Al-Cr-O surface nano-composite layer fabricated on Al6061 plate by friction stir processing," *Wear*, vol. 304, no. 1–2, pp. 144–151, 2013.

[69] D. K. Sharma, V. Patel, V. Badheka, K. Mehta, and G. Upadhyay, "Fabrication of Hybrid Surface Composites AA6061/(B4C + MoS2) via Friction Stir Processing," *J. Tribol.*, vol. 141, no. 5, pp. 1–10, 2019.

[70] V. Kishan, A. Devaraju, and K. Prasanna Lakshmi, "Influence of volume percentage of NanoTiB2 particles on tribological & mechanical behaviour of 6061-T6 Al alloy nano-surface composite layer prepared via friction stir process," *Def. Technol.*, vol. 13, no. 1, pp. 16–21, 2017.

[71] I. Dinaharan, R. Nelson, S. J. Vijay, and E. T. Akinlabi, "Microstructure and wear characterization of aluminum matrix composites reinforced with industrial waste fly ash particulates synthesized by friction stir processing," *Mater. Charact.*, vol. 118, pp. 149–158, 2016.

[72] C. M. Rejil, I. Dinaharan, S. J. Vijay, and N. Murugan, "Microstructure and sliding wear behavior of AA6360/(TiC+B 4C) hybrid surface composite layer synthesized by friction stir processing on aluminum substrate," *Mater. Sci. Eng. A*, vol. 552, pp. 336–344, 2012.

[73] K. M. Mehta and V. J. Badheka, "Wear behavior of boron-carbide reinforced aluminum surface composites fabricated by Friction Stir Processing," *Wear*, vol. 426–427, no. September 2018, pp. 975–980, 2019.

[74] S. Rathee, S. Maheshwari, A. N. Siddiquee, and M. Srivastava, "Effect of tool plunge depth on reinforcement particles distribution in surface composite fabrication via friction stir processing," *Def. Technol.*, vol. 13, no. 2, pp. 86–91, 2017.

[75] A. R. Cisko *et al.*, "Characterization of fatigue behavior of Al-Li alloy 2099," *Mater. Charact.*, vol. 151, no. March, pp. 496–505, 2019.

[76] H. Liu, Y. Hu, C. Dou, and D. P. Sekulic, “An effect of the rotation speed on microstructure and mechanical properties of the friction stir welded 2060-T8 Al-Li alloy,” *Mater. Charact.*, 2017.

[77] H. Qin, H. Zhang, and H. Wu, “The evolution of precipitation and microstructure in friction stir welded 2195-T8 Al-Li alloy,” *Mater. Sci. Eng. A*, 2015.

[78] N. D. Alexopoulos, E. Migklis, A. Stylianos, and D. P. Myriounis, “Fatigue behavior of the aeronautical Al-Li (2198) aluminum alloy under constant amplitude loading,” *Int. J. Fatigue*, 2013.

[79] M. J. Adinoyi, N. Merah, and J. Albinmousa, “Shear fatigue behavior of AW2099-T83 aluminum-lithium alloy,” *Int. J. Fatigue*, vol. 117, no. August, pp. 101–110, 2018.

[80] C. Bitondo *et al.*, “Friction stir welding of AA2198-T3 butt joints for aeronautical applications,” *Int. J. Mater. Form.*, vol. 3, no. SUPPL. 1, pp. 1079–1082, 2010.

[81] Y. E. Ma, Z. C. Xia, R. R. Jiang, and W. Y. Li, “Effect of welding parameters on mechanical and fatigue properties of friction stir welded 2198 T8 aluminum–lithium alloy joints,” *Eng. Fract. Mech.*, vol. 114, pp. 1–11, 2013.

[82] A. Muthumanickam, P. Gandham, and S. Dhenuvakonda, “Effect of Friction Stir Welding Parameters on Mechanical Properties and Microstructure of AA2195 Al–Li Alloy Welds,” *Trans. Indian Inst. Met.*, vol. 72, no. 6, pp. 1557–1561, 2019.

[83] ASTM, “ASTM E112-13: Standard test methods for determining average grain size,” *ASTM Int.*, 2013.

[84] R. Kumar, K. Singh, and S. Pandey, “Process forces and heat input as function of process parameters in AA5083 friction stir welds,” *Trans. Nonferrous Met. Soc. China (English Ed.*, 2012.

[85] A. Forcellese, M. Martarelli, and M. Simoncini, “Effect of process parameters on vertical forces and temperatures developed during friction stir welding of magnesium alloys,” *Int. J. Adv. Manuf. Technol.*, 2016.

[86] M. J. Peel, A. Steuwer, P. J. Withers, T. Dickerson, Q. Shi, and H. Shercliff, “Dissimilar friction stir welds in AA5083-AA6082. Part I: Process parameter effects on thermal history and weld properties,” *Metall. Mater. Trans. A Phys. Metall. Mater. Sci.*, 2006.

[87] S. Cui, Z. W. Chen, and J. D. Robson, “A model relating tool torque and its associated power and specific energy to rotation and forward speeds during friction stir welding/processing,” *Int. J. Mach. Tools Manuf.*, 2010.

[88] M. Azizieh, A. H. Kokabi, and P. Abachi, “Effect of rotational speed and probe

profile on microstructure and hardness of AZ31/Al2O3 nanocomposites fabricated by friction stir processing," *Mater. Des.*, 2011.

[89] M. A. Moghaddas and S. F. Kashani-Bozorg, "Effects of thermal conditions on microstructure in nanocomposite of Al/Si 3N 4 produced by friction stir processing," *Mater. Sci. Eng. A*, 2013.

[90] T. R. McNelley, S. Swaminathan, and J. Q. Su, "Recrystallization mechanisms during friction stir welding/processing of aluminum alloys," *Scr. Mater.*, 2008.

[91] P. B. Prangnell and C. P. Heason, "Grain structure formation during friction stir welding observed by the 'stop action technique,'" *Acta Mater.*, 2005.

[92] K. V. Jata and S. L. Semiatin, "Continuous dynamic recrystallization during friction stir welding of high strength aluminum alloys," *Scr. Mater.*, 2000.

[93] G. Buffa, L. Fratini, and R. Shivpuri, "CDRX modelling in friction stir welding of AA7075-T6 aluminum alloy: Analytical approaches," *J. Mater. Process. Technol.*, 2007.

[94] A. Rollett, F. Humphreys, G. S. Rohrer, and M. Hatherly, *Recrystallization and Related Annealing Phenomena: Second Edition*. 2004.

[95] J. J. Shen, H. J. Liu, and F. Cui, "Effect of welding speed on microstructure and mechanical properties of friction stir welded copper," *Mater. Des.*, 2010.

[96] B. D. Cullity and S. R. Stock, "Elements of X-ray diffraction, 3rd edition," *Prentice Hall*, 2001.

[97] H. Patle, R. Dumpala, and B. R. Sunil, "Machining Characteristics and Corrosion Behavior of Grain Refined AZ91 Mg Alloy Produced by Friction Stir Processing: Role of Tool Pin Profile," *Trans. Indian Inst. Met.*, 2018.

[98] M. Pezeshkian, I. Ebrahimzadeh, and F. Gharavi, "Fabrication of Cu Surface Composite Reinforced by Ni Particles Via Friction Stir Processing: Microstructure and Tribology Behaviors," *J. Tribol.*, 2018.

[99] C. Sharma, D. K. Dwivedi, and P. Kumar, "Effect of welding parameters on microstructure and mechanical properties of friction stir welded joints of AA7039 aluminum alloy," *Mater. Des.*, vol. 36, pp. 379–390, Apr. 2012.

[100] D. D. Macdonald, "Review of mechanistic analysis by electrochemical impedance spectroscopy," *Electrochim. Acta*, 1990.

[101] E. McCafferty, *Introduction to corrosion science*. 2010.

[102] B. G. Prakashaiah, D. Vinaya Kumara, A. Anup Pandith, A. Nityananda Shetty, and B. E. Amitha Rani, "Corrosion inhibition of 2024-T3 aluminum alloy in 3.5%

NaCl by thiosemicarbazone derivatives," *Corros. Sci.*, 2018.

[103] J. R. Scully, D. C. Silverman, and M. W. Kendig, *Electrochemical Impedance: Analysis and Interpretation*. 1993.

[104] S. Abbasi, M. Nouri, and A. Sabour Rouhaghdam, "A novel combined method for fabrication of stable corrosion resistance superhydrophobic surface on Al alloy," *Corros. Sci.*, 2019.

[105] D. S. Chauhan, K. R. Ansari, A. A. Sorour, M. A. Quraishi, H. Lgaz, and R. Salghi, "Thiosemicarbazide and thiocarbohydrazide functionalized chitosan as ecofriendly corrosion inhibitors for carbon steel in hydrochloric acid solution," *Int. J. Biol. Macromol.*, 2018.

[106] J. Lv, H. Luo, and J. Xie, "Experimental study of corrosion behavior for burnished aluminum alloy by EWF, EBSD, EIS and Raman spectra," *Appl. Surf. Sci.*, 2013.

[107] Z. J. Zheng, Y. Gao, Y. Gui, and M. Zhu, "Corrosion behaviour of nanocrystalline 304 stainless steel prepared by equal channel angular pressing," *Corros. Sci.*, 2012.

[108] U. Trdan and J. Grum, "Evaluation of corrosion resistance of AA6082-T651 aluminium alloy after laser shock peening by means of cyclic polarisation and ElS methods," *Corros. Sci.*, 2012.

[109] F. El-Taib Heakal, N. S. Tantawy, and O. S. Shehta, "Influence of chloride ion concentration on the corrosion behavior of Al-bearing TRIP steels," *Mater. Chem. Phys.*, 2011.

[110] M. Yadav, S. Kumar, R. R. Sinha, I. Bahadur, and E. E. Ebenso, "New pyrimidine derivatives as efficient organic inhibitors on mild steel corrosion in acidic medium: Electrochemical, SEM, EDX, AFM and DFT studies," *J. Mol. Liq.*, 2015.

[111] V. Pandey, J. K. Singh, K. Chattopadhyay, N. C. S. Srinivas, and V. Singh, "Optimization of USSP duration for enhanced corrosion resistance of AA7075," *Ultrasonics*, 2019.

[112] K. R. Ansari, M. A. Quraishi, and A. Singh, "Schiff's base of pyridyl substituted triazoles as new and effective corrosion inhibitors for mild steel in hydrochloric acid solution," *Corros. Sci.*, 2014.

[113] R. Acuña, C. M. Abreu, M. J. Cristóbal, M. Cabeza, and X. R. Nóvoa, "Electrochemical study of the surface metal matrix composite developed on AA 2024-T351 by the friction stir process," *Corros. Eng. Sci. Technol.*, 2019.

[114] B. Guitián, X. R. Nóvoa, and B. Puga, "Electrochemical Impedance Spectroscopy as a tool for materials selection: Water for haemodialysis," in *Electrochimica Acta*, 2011.

[115] S. Deng and X. Li, "Inhibition by Jasminum nudiflorum Lindl. leaves extract of the corrosion of aluminium in HCl solution," *Corros. Sci.*, 2012.

[116] J. J. Gray and C. A. Orme, "Electrochemical impedance spectroscopy study of the passive films of alloy 22 in low pH nitrate and chloride environments," *Electrochim. Acta*, 2007.

[117] Y. Liu, G. Z. Meng, and Y. F. Cheng, "Electronic structure and pitting behavior of 3003 aluminum alloy passivated under various conditions," *Electrochim. Acta*, 2009.

[118] K. Haruna, I. B. Obot, N. K. Ankah, A. A. Sorour, and T. A. Saleh, "Gelatin: A green corrosion inhibitor for carbon steel in oil well acidizing environment," *J. Mol. Liq.*, 2018.

[119] M. an Chen, Y. chun Ou, Y. hong Fu, Z. hua Li, J. ming Li, and S. dan Liu, "Effect of friction stirred Al-Fe-Si particles in 6061 aluminum alloy on structure and corrosion performance of MAO coating," *Surf. Coatings Technol.*, 2016.

[120] I. Milošev, T. Kosec, and H. H. Strehblow, "XPS and EIS study of the passive film formed on orthopaedic Ti-6Al-7Nb alloy in Hank's physiological solution," *Electrochim. Acta*, 2008.

[121] T. Hong, Y. H. Sun, and W. P. Jepson, "Study on corrosion inhibitor in large pipelines under multiphase flow using EIS," *Corros. Sci.*, 2002.

[122] A. Viceré, G. Roventi, C. Paoletti, M. Cabibbo, and T. Bellezze, "Corrosion behavior of aa6012 aluminum alloy processed by ecap and cryogenic treatment," *Metals (Basel).*, 2019.

[123] A. Y. Adesina, Z. M. Gasem, and A. Madhan Kumar, "Corrosion Resistance Behavior of Single-Layer Cathodic Arc PVD Nitride-Base Coatings in 1M HCl and 3.5 pct NaCl Solutions," *Metall. Mater. Trans. B Process Metall. Mater. Process. Sci.*, 2017.

[124] E. Avcu, "The influences of ECAP on the dry sliding wear behaviour of AA7075 aluminium alloy," *Tribol. Int.*, vol. 110, no. October 2016, pp. 173–184, 2017.

[125] T. Kucukomeroglu, "Effect of equal-channel angular extrusion on mechanical and wear properties of eutectic Al-12Si alloy," *Mater. Des.*, 2010.

[126] C. T. Wang, N. Gao, R. J. K. Wood, and T. G. Langdon, "Wear behavior of an aluminum alloy processed by equal-channel angular pressing," *J. Mater. Sci.*, 2011.

[127] E. Ortiz-Cuellar, M. A. L. Hernandez-Rodriguez, and E. García-Sanchez, "Evaluation of the tribological properties of an Al-Mg-Si alloy processed by

severe plastic deformation," *Wear*, 2011.

[128] K. D. Ralston, N. Birbilis, and C. H. J. Davies, "Revealing the relationship between grain size and corrosion rate of metals," *Scr. Mater.*, 2010.

[129] K. D. Ralston and N. Birbilis, "Effect of grain size on corrosion: A review," *Corrosion*, 2010.

[130] M. K. Chung, Y. S. Choi, J. G. Kim, Y. M. Kim, and J. C. Lee, "Effect of the number of ECAP pass time on the electrochemical properties of 1050 Al alloys," *Mater. Sci. Eng. A*, 2004.

[131] O. Jilani, N. Njah, and P. Ponthiaux, "Corrosion properties of anodized aluminum: Effects of equal channel angular pressing prior to anodization," *Corros. Sci.*, 2014.

[132] L. Jinlong, L. Tongxiang, W. Chen, and G. Ting, "The passive film characteristics of several plastic deformation 2099 Al-Li alloy," *J. Alloys Compd.*, 2016.

[133] I. Charit and R. S. Mishra, "High strain rate superplasticity in a commercial 2024 Al alloy via friction stir processing," *Mater. Sci. Eng. A*, 2003.

[134] I. Vysotskiy, D. Zhemchuzhnikova, S. Malopheyev, S. Mironov, and R. Kaibyshev, "Microstructure evolution and strengthening mechanisms in friction-stir welded Al–Mg–Sc alloy," *Mater. Sci. Eng. A*, vol. 770, no. October 2019, p. 138540, 2020.

[135] G. R. Argade, N. Kumar, and R. S. Mishra, "Stress corrosion cracking susceptibility of ultrafine grained Al-Mg-Sc alloy," *Mater. Sci. Eng. A*, 2013.

[136] A. G. Rao, V. A. Katkar, G. Gunasekaran, V. P. Deshmukh, N. Prabhu, and B. P. Kashyap, "Effect of multipass friction stir processing on corrosion resistance of hypereutectic Al-30Si alloy," *Corros. Sci.*, 2014.

[137] D. SONG, A. bin MA, J. hua JIANG, P. hua LIN, and D. hui YANG, "Corrosion behavior of ultra-fine grained industrial pure Al fabricated by ECAP," *Trans. Nonferrous Met. Soc. China (English Ed.*, 2009.

[138] M. Zohoor, M. K. Besharati Givi, and P. Salami, "Effect of processing parameters on fabrication of Al-Mg/Cu composites via friction stir processing," *Mater. Des.*, 2012.

[139] Y. J. Kwon, I. Shigematsu, and N. Saito, "Mechanical properties of fine-grained aluminum alloy produced by friction stir process," *Scr. Mater.*, 2003.

[140] A. Korchef, Y. Champion, and N. Njah, "X-ray diffraction analysis of aluminium containing Al8Fe2Si processed by equal channel angular pressing," *J. Alloys Compd.*, 2007.

[141] A. Dolatkhah, P. Golbabaei, M. K. Besharati Givi, and F. Molaiekiya, "Investigating effects of process parameters on microstructural and mechanical properties of Al5052/SiC metal matrix composite fabricated via friction stir processing," *Mater. Des.*, 2012.

[142] Z. Tao, S. Zhang, W. Li, and B. Hou, "4-Chloro-benzoic acid [1,2,4]triazol-1-ylmethyl ester as an effective inhibitor of mild steel corrosion in HCl solution," *Mater. Corros.*, 2010.

[143] W. Li, L. Hu, Z. Tao, H. Tian, and B. Hou, "Experimental and quantum chemical studies on two triazole derivatives as corrosion inhibitors for mild steel in acid media," *Mater. Corros.*, 2011.

[144] S. John and A. Joseph, "Quantum chemical and electrochemical studies on the corrosion inhibition of aluminium in 1 N HNO3 using 1,2,4-triazine," *Mater. Corros.*, 2013.

[145] K. Surekha, B. S. Murty, and K. Prasad Rao, "Effect of processing parameters on the corrosion behaviour of friction stir processed AA 2219 aluminum alloy," *Solid State Sci.*, 2009.

[146] M. Navaser and M. Atapour, "Effect of Friction Stir Processing on Pitting Corrosion and Intergranular Attack of 7075 Aluminum Alloy," *J. Mater. Sci. Technol.*, 2017.

[147] H. J. Liu, J. C. Hou, and H. Guo, "Effect of welding speed on microstructure and mechanical properties of self-reacting friction stir welded 6061-T6 aluminum alloy," *Mater. Des.*, 2013.

[148] F. L. Zeng *et al.*, "Corrosion mechanism associated with Mg 2Si and Si particles in Al-Mg-Si alloys," *Trans. Nonferrous Met. Soc. China (English Ed.*, vol. 21, no. 12, pp. 2559–2567, 2011.

[149] Y. Wu and H. Liao, "Corrosion Behavior of Extruded near Eutectic Al-Si-Mg and 6063 Alloys," *J. Mater. Sci. Technol.*, 2013.

[150] H. Ahlatci, "Wear and corrosion behaviours of extruded Al-12Si-XMg alloys," *Mater. Lett.*, 2008.

[151] E. Balducci, L. Ceschini, S. Messieri, S. Wenner, and R. Holmestad, "Thermal stability of the lightweight 2099 Al-Cu-Li alloy: Tensile tests and microstructural investigations after overaging," *Mater. Des.*, 2017.

[152] B. Cai, Z. Q. Zheng, D. Q. He, S. C. Li, and H. P. Li, "Friction stir weld of 2060 Al-Cu-Li alloy: Microstructure and mechanical properties," *J. Alloys Compd.*, 2015.

[153] A. K. Shukla and W. A. Baeslack, “Study of microstructural evolution in friction-stir welded thin-sheet Al-Cu-Li alloy using transmission-electron microscopy,” *Scr. Mater.*, 2007.

[154] Y. Tao *et al.*, “Friction stir welding of 2060–T8 Al[sbnd]Li alloy. Part I: Microstructure evolution mechanism and mechanical properties,” *Mater. Charact.*, vol. 168, no. June, 2020.

[155] Y. Lin and Z. Zheng, “Microstructural evolution of 2099 Al[sbnd]Li alloy during friction stir welding process,” *Mater. Charact.*, vol. 123, pp. 307–314, 2017.

[156] C. Gao, Z. Zhu, J. Han, and H. Li, “Correlation of microstructure and mechanical properties in friction stir welded 2198-T8 Al-Li alloy,” *Mater. Sci. Eng. A*, vol. 639, pp. 489–499, 2015.

[157] Y. Mao, L. Ke, F. Liu, C. Huang, Y. Chen, and Q. Liu, “Effect of welding parameters on microstructure and mechanical properties of friction stir welded joints of 2060 aluminum lithium alloy,” *Int. J. Adv. Manuf. Technol.*, vol. 81, no. 5–8, pp. 1419–1431, 2015.

[158] K. Yan, T. Wang, H. Liang, and Y. Zhao, “Effects of Rotation Speed on Microstructure and Mechanical Properties of 2060 Al-Cu-Li Alloy in Friction Stir Welding,” *J. Mater. Eng. Perform.*, vol. 27, no. 11, pp. 5803–5814, 2018.

[159] J. F. Li, Z. Q. Zheng, W. Da Ren, W. J. Chen, X. S. Zhao, and S. C. Li, “Simulation on function mechanism of Tl(Al2CuLi) precipitate in localized corrosion of Al-Cu-Li alloys,” *Trans. Nonferrous Met. Soc. China (English Ed.*, 2006.

[160] V. Proton *et al.*, “The influence of artificial ageing on the corrosion behaviour of a 2050 aluminium-copper-lithium alloy,” *Corros. Sci.*, vol. 80, pp. 494–502, 2014.

[161] Y. Ma *et al.*, “ Corrosion and Anodizing Behavior of T 1 (Al 2 CuLi) Precipitates in Al-Cu-Li Alloy ,” *J. Electrochem. Soc.*, vol. 166, no. 12, pp. C296–C303, 2019.

[162] J. lei Huang *et al.*, “Correlation of intergranular corrosion behaviour with microstructure in Al-Cu-Li alloy,” *Corros. Sci.*, 2018.

[163] J. F. Li, Z. Q. Zheng, S. C. Li, W. J. Chen, W. D. Ren, and X. S. Zhao, “Simulation study on function mechanism of some precipitates in localized corrosion of Al alloys,” *Corros. Sci.*, vol. 49, no. 6, pp. 2436–2449, 2007.

[164] Y. Ma *et al.*, “Crystallographic defects induced localised corrosion in AA2099-T8 aluminium alloy,” *Corros. Eng. Sci. Technol.*, 2015.

[165] J. F. Li, Z. Ziqiao, J. Na, and T. Chengyu, “Localized corrosion mechanism of 2×××-series Al alloy containing S(Al2CuMg) and θ′(Al2Cu) precipitates in 4.0%

NaCl solution at pH 6.1," *Materials Chemistry and Physics*, vol. 91, no. 2–3. pp. 325–329, 2005.

[166] J. F. Li, C. X. Li, Z. W. Peng, W. J. Chen, and Z. Q. Zheng, "Corrosion mechanism associated with T1 and T2 precipitates of Al-Cu-Li alloys in NaCl solution," *J. Alloys Compd.*, 2008.

VITAE

Name :Ibrahim Hassan ZainElabdeen Mohammed

Nationality :Sudanese

Date of Birth :1/1/1993

Email :ibrahem.hsn@outlook.com

Address :Hasahiesa, Gezira, Sudan

Postal code : 79371

Academic Background : MSc. (Mechanical Engineering), April 2020, King Fahd University of Petroleum and Menerals, Dhahran, Kingdom of Saudi Arabia.

: BSc. (Mechanical Engineering), October, 2015 University of Khartoum, Khartoum, Sudan.

Research Interests : FS Welding/Processing, Nanocomposite coatings,. Tribology of metals and Polymers.

Publications:

1- Adesina AY**, Zainelabdeen IH**, Dalhat MA, Mohammed AS, Sorour AA, Al Badour FA, Influence of micronized waste tire rubber on the mechanical and tribological properties of epoxy composite coatings, Tribology International (2020), doi: https://doi.org/10.1016/ j.triboint.2020.106244.

2- Al-Badour, Fadi, **Zainelabdeen IH,** Suleiman, Rami K., and Adesina, Akeem. "Crack Repair Using Hybrid Additive Manufacturing and Friction Stir Processing." *Proceedings of the . Volume 6A: Materials and Fabrication*. San Antonio, Texas, USA. July 14–19, 2019. V06AT06A004. ASME. https://doi.org/10.1115/PVP2019-93688.